Generation, Handling and Transport of Laser-Driven Heavy Ion Beams

Erzeugung, Handhabung und Transport von lasergetriebenen Schwerionenstrahlen
Zur Erlangung des Grades eines Doktors der Naturwissenschaften (Dr. rer. nat.)
genehmigte Dissertation von Johannes Ding aus Augsburg
Tag der Einreichung: 10. Juli 2018, Tag der Prüfung: 29. Oktober 2018
Darmstadt — D 17

1. Gutachten: Prof. Dr. Markus Roth
2. Gutachten: Prof. Dr. Oliver Boine-Frankenheim

TECHNISCHE
UNIVERSITÄT
DARMSTADT

Fachbereich Physik
Institut für Kernphysik
Arbeitsgruppe Prof. Dr. Markus Roth

Generation, Handling and Transport of Laser-Driven Heavy Ion Beams
Erzeugung, Handhabung und Transport von lasergetriebenen Schwerionenstrahlen

Genehmigte Dissertation von Johannes Ding aus Augsburg

1. Gutachten: Prof. Dr. Markus Roth
2. Gutachten: Prof. Dr. Oliver Boine-Frankenheim

Tag der Einreichung: 10. Juli 2018
Tag der Prüfung: 29. Oktober 2018

Darmstadt — D 17

Bitte zitieren Sie dieses Dokument als:
URN: urn:nbn:de:tuda-tuprints-82148
https://tuprints.ulb.tu-darmstadt.de/id/eprint/8214

Zusammenfassung

Die vorliegende Dissertation behandelt die Erzeugung, Handhabung und den Transport von laser-beschleunigten Schwerionenstrahlen. Die dargestellte Forschungsarbeit wurde innerhalb der Laser- und Plasmaphysikgruppe am Institut für Kernphysik der Technischen Universität Darmstadt erbracht. Die Experimentkampagnen, die zu den Erkenntnissen dieser Arbeit beitragen, wurden am GSI Helmholtzzentrum für Schwerionenforschung mit der Unterstützung der dortigen Abteilung für Plasmaphysik durchgeführt.

Die lasergetriebene Ionenbeschleunigung mittels der sogenannten Target Normal Sheath Acceleration (TNSA) ermöglicht die kompakte Erzeugung von intensiven Ionenstrahlen, deren kinetische Energie im Bereich von einigen 10 MeV liegt. Die laserbeschleunigten Ionen weisen einzigartige Eigenschaften auf, wie eine sehr kleine transversale und longitudinale Emittanz, sehr hohe Ionenzahlen pro Paket, aber auch ein sehr breites und exponentiell zu höheren Energien abfallendes Energiespektrum und eine große Divergenz. Die Zusammensetzung der Ionensorten im Strahl hängt von der Atomzusammensetzung der Quellregion ab und ist aufgrund der Natur des Beschleungigungsmechanismus im Allgemeinen von Protonen dominiert, die aus Kohlenwasserstoffverunreinigungen der Oberfläche stammen. Viele vorraussichtliche Anwendungen der lasergetriebenen Ionenstrahlen sind auf die effiziente Beschleunigung von Schwerionen angewiesen und auch darauf, dass die Divergenz und die Energieverteilung der ursprünglichen TNSA-Strahlen beeinflusst werden können.

In der vorliegenden Arbeit konnte die effiziente Beschleunigung von Fluor- und Kohlenstoffionenstrahlen durch den TNSA-Mechanismus gezeigt werden. Die Kohlenwasserstoffverunreinigungen auf der Oberfläche der beschichteten Targets wurden durch Joule'sche Heizung entfernt. Dadurch konnten mithilfe der 100 TW Strahlführung des PHELIX Lasersystems an der GSI vierfach positiv geladene Kohlenstoffionen (C^{4+}) mit kinetischen Energien bis zu $68,5^{+4,8}_{-4,3}$ MeV und siebenfach geladene Fluorionen (F^{7+}) mit bis zu 180^{+32}_{-26} MeV erzeugt werden.

Der Einsatz eines gepulsten Hochfeld-Solenoidmagneten vom Helmholtzzentrum Dresden-Rossendorf innerhalb der Prototyp-Strahlführung der LIGHT (Laser Ion Generation, Handling and Transport) Kollaboration bot die Möglichkeit, die lasergetriebenen Fluor- und Kohlenstoffionenstrahlen effizient zu kollimieren und zu transportieren. Aufgrund der chromatischen Fokussierung konnte ein Teil des Ionenspektrums ausgewählt werden. In einem Abstand von mehr als $6,0\,\mathrm{m}$ von der Ionenquelle konnten $9,9^{+2,7}_{-3,1} \cdot 10^8$ C^{4+} Ionen mit einer durchschnittlichen Energie von $(14,9 \pm 0,1)$ MeV nachgewiesen werden, indem radiochromatische Filme mit Thomson Parabeln kombiniert wurden.

Neben der Identifizierung herausfordernder Problemstellungen im Bezug auf die zeitliche Komprimierung von Schwerionenpaketen wurden auch gangbare Lösungen für diese Probleme aufgezeigt und bereits in die LIGHT-Strahlfürung implementiert. Eine erste erfolgreiche

Demonstration der effizienten zeitlichen Komprimierung von laserbeschleunigten F^{7+} Ionenstrahlen resultierte in $(1,3 \pm 0,1)$ ns (FWHM) kurzen Ionenpaketen.

Die erfolgreiche effiziente Erzeugung, Handhabung und der Transport von lasergetriebenen Schwerionenstrahlen rückt eine lasergetriebene Ionenstrahlführung für beispielsweise die Untersuchung des Bremsvermögens von dichten Plasmen im Bezug auf Ionen in greifbare Nähe.

Abstract

The thesis at hand addresses the generation, handling and transport of laser-driven heavy ion beams. The presented research has been conducted within the laser and plasma physics group at the institute of nuclear physics of the Technical University of Darmstadt. The experimental campaigns contributing to the results in this thesis have been carried out at the GSI Helmholtz Center for Heavy Ion Research and were supported by their plasma physics department.

The laser-driven ion acceleration scheme target normal sheath acceleration (TNSA) enables the compact generation of intense ion bunches with kinetic energies in the range of 10s of MeV. The laser-accelerated ion beams have unique properties, such as extremely small transverse and longitudinal emittance, high numbers of ions per bunch, but also broad exponentially decaying energy spectra and high divergence. Due to the nature of the acceleration process the composition of ion species in the beam is defined by the atom population in the source area and is generally dominated by protons stemming from ever present hydro-carbon contaminations. Many anticipated applications of laser-driven ion beams rely on the efficient acceleration of heavy ions and on controlling the energy spread and the divergence of the initial TNSA beam.

In this work the efficient acceleration of carbon and fluorine ion beams by means of TNSA was demonstrated. The hydrocarbon contaminations on the surface of the coated targets were removed by means of Joule heating. Utilizing this method and the 100 TW beamline of the PHELIX laser system at GSI, kinetic energies of fourfold positively charged carbon ions (C^{4+}) of up to $68.5^{+4.8}_{-4.3}$ MeV and of sevenfold positively charged fluorine ions (F^{7+}) of up to 180^{+32}_{-26} MeV were observed.

With the help of a pulsed high-field solenoid magnet from Helmholtz Center Dresden-Rossendorf incorporated into the prototype beamline of the LIGHT (Laser Ion Generation, Handling and Transport) collaboration, the efficient collimation and transport as well as the energy selection by means of chromatic focussing of the laser-driven carbon and fluorine ion beams could be achieved. At an average energy of (14.9 ± 0.1) MeV a number of $9.9^{+2.7}_{-3.1} \cdot 10^8$ C^{4+} ions were detected at a distance from the ion source of more than 6.0 m by a combination of radiochromic films and Thomson parabolas.

Challenging problems for the temporal bunch compression of laser-driven heavy ion beams with a three gap spiral resonator as well as viable solutions to these hurdles have been identified and already incorporated into the LIGHT beamline within the scope of this thesis. A first successful proof-of-principle of temporal bunch compression of laser-driven fluorine ion beams resulted in bunches as short as (1.3 ± 0.1) ns (FWHM).

By successfully demonstrating the efficient generation, handling and transport of laser-driven heavy ion beams an anticipated laser-driven ion beamline for the investigation of for example the stopping power of ions in dense plasmas is within reach.

Contents

1 Introduction

The history of the laser, its rapid and ever continuing improvement, is a great success story. More than 50 years after the discovery of the first ruby laser by T. Maiman in 1960 [1] the 21st century is generally being viewed at as the "century of the photon", because the laser is seen as a key technology to the majority of modern research and development.

Shortly after the groundbreaking discovery by T. Maiman the techniques of Q-switching [2] and mode-locking [3] allowed for the generation of short laser pulses with pulse durations as low as femtoseconds. The *chirped pulse amplification* (**CPA**), developed by G. Mourou and D. Strickland in 1985 [4], enabled the amplification of these pulses up to several hundreds of Joules. Further development in numerous high power laser facilities around the world resulted so far in several petawatt class laser systems [5, 6, 7]. Focussing of the resulting high power laser pulses leads to intensities as high as $10^{20}\,\mathrm{W\,cm^{-2}}$ to $10^{21}\,\mathrm{W\,cm^{-2}}$. With the imminent *extreme light infrastructure* (**ELI**) [8], laser facilities with pulse power exceeding 10 petawatt will be available.

These very intense laser pulses of typically less than one picosecond duration have opened a completely new scientific field, the relativistic laser-plasma-interaction. The laser pulse interacts with an initially solid or gaseous medium, which gets ionized at least partially. Free electrons in the resulting plasma are accelerated to velocities close to the speed of light in the time span of a single laser cycle [9]. Among others, phenomena such as the generation of high harmonics of the laser pulse [10], x-rays caused by synchrotron radiation [11], electron acceleration [12, 13] and ion acceleration [14, 15, 16] all originate from relativistic laser-plasma-interactions.

Almost two decades after the discovery of compact acceleration of ions by means of ultra-intense laser irradiation of solid targets [14, 17], the mechanism is still subject to research. The new source for intense MeV-range ion bunches is considerted to be a driver for many applications. These range from: igniting inertial confinement fusion [18, 19], driving isochoric heating to achieve warm dense matter [20, 21, 22] to the generation of isotopes with table-top devices [23], and particle therapy [24, 25]. Due to the high particle numbers and initially short pulse durations of the ion bunches the monitoring of transient phenomena is an interesting field of work [26]. Lately the generation of laser-driven neutron beams has been investigated by several groups [27, 28]

Despite theoretical evidence in *particle in cell* (**PIC**) simulations for potentially game-changing new acceleration mechanisms such as the *breakout-afterburner* (**BoA**) [29, 30], enabled by *radiation induced transparency* (**RIT**) [31, 32] or the *radiation pressure acceleration* (**RPA**) [33], up to now the only reliable mechanism is *target normal sheath acceleration* (**TNSA**) [14, 17, 15]. By irradiating micrometer thick targets with ultra-intense shortpulse lasers, which are focussed down to more than $10^{18}\,\mathrm{W\,cm^{-2}}$, electrons from the front surface are pushed through the bulk material and form an electron sheath on the rear face of the target. The resulting electrical field, which is in the order of $10^{12}\,\mathrm{V\,m^{-1}}$, ionizes the atoms on the rear surface and subsequently accelerates the ions up to several tens of MeV. Due to the initially cold ion temperature, the absence of collisions during the acceleration process and the process taking place on a picosecond time scale, the ion beams exhibit some exceptional characteristics. Total particle numbers exceed 10^{12} and stem from a sub-mm source area with transverse emittances as low as 0.01 mm mrad. While the energy spectrum of the ions has an exponentially decaying distribution, there is a very high degree of order in the longitudinal structure of the beam, manifesting itself in the longitudinal emittance being below 10^{-4} eV s for specific energies [34]. Many of the above mentioned applications, such as isochoric heating, could be improved by separating the TNSA source spatially from the application, because highly relativistic electrons, x-rays, *electro-magnetic pulses* (**EMP**) and plasmas in general lead to strong interference for any measurement. Ion beam therapy imposes high demands on the maximum energy spread and brilliance of the applied ion beam. Thus, utilizing a TNSA ion beam for these kinds of applications, either the TNSA source has to be specifically tailored to allow for precise beam tuning, or the TNSA source has to be incorporated into a collimating and energy selective ion optical system.

The former was attempted by tailoring the target, but this method could only influence the ion beam on a microscopic scale [20, 35]. The latter has shown promising results by utilizing conventional magnetic focussing devices like quadrupoles [36] or solenoids [37, 38, 39]. The combination of a laser-driven ion source with conventional accelerator technology seems to be the way to go and several projects are investigating in this field. Among others the ELI has dedicated a substantial work package, ELI-MED [40], to the transport and handling of laser-driven ion pulses with ion optical systems. Within the joint research project onCOOPtics[1] investigations are under way to take advantage of laser-driven ion acceleration in order to make ion beam therapy more compact and affordable [41]. One of the most successful collaborative efforts has been undertaken by German universities and Helmholtz centres to examine *laser ion generation, handling and transport* (**LIGHT**) [42].

This thesis is part of an ongoing investigation within the LIGHT project to selectively collimate a highly divergent laser-driven ion beam in such a way as to reduce the energy spread and compress the bunch temporally. In contrast to previous works by K. Harres [38, 43], T. Burris-Mog [37, 44], S. Busold [39, 42, 45, 46] and F. Kroll [47] and ongoing research [48], this thesis investigates laser-driven mid-Z ion beams instead of proton beams.

1.1 The LIGHT project

The LIGHT collaborators from the Technical University of Darmstadt, GSI Helmholtz-center for heavy ion research (GSI), Helmholtz-center Dresden-Rossendorf (HZDR), Johann Wolfgang Goethe University Frankfurt, Helmholtz Institute Jena and Ludwig-Maximilians-University Munich have chosen the Z6 experimental area at GSI as a testbed for a laser-driven ion beamline. The choice was made based on the unique capabilities offered by the *petawatt high-energy laser for heavy ion experiments* (**PHELIX**) laser system [7] and the existing accelerator expertise and infrastructure. In particular the *radiofrequency* (**rf**) power supply, required for temporal bunch compression with resonators, could be provided by the *universal linear accelerator* (**UNILAC**), thus making the Z6 experimental area at GSI a unique experimental site. The high energy laser nhelix [49] enhances the future capabilities for applications of the LIGHT beamline.

After demonstrating the effectiveness of pulsed solenoids for the collimation of laser-driven proton beams [37, 38] with experiments at the PHELIX Petawatt experimental area, further work was conducted at the Z6 experimental area. S. Busold et al. built and characterized

---

[1] Consists of Helmholtz-Zentrum Dresden-Rossendorf (HZDR), OncoRay, Dresden and ultra optics, Jena

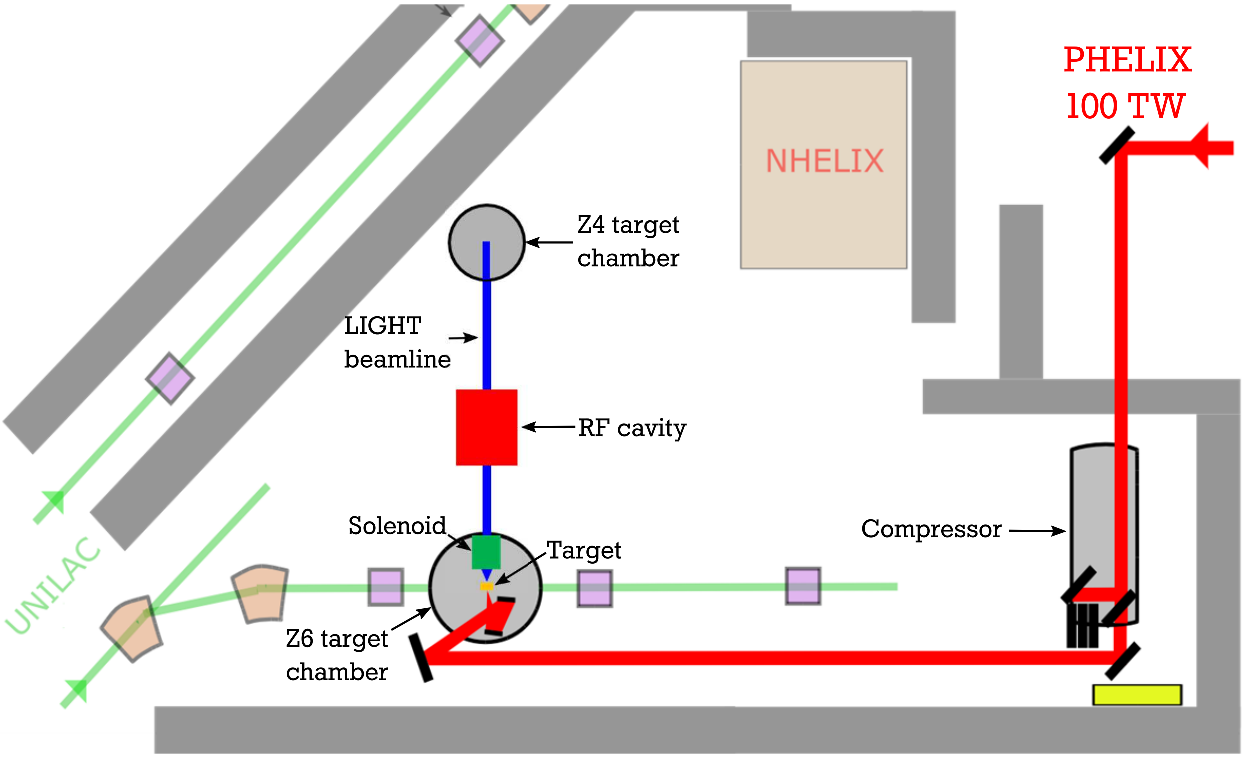

Figure 1.1: Overview of the Z6 experimental area at GSI (courtesy of B. Zielbauer) with LIGHT beamline; The PHELIX laser drives the ion acceleration in the Z6 target chamber. A pulsed solenoid collimates a part of the divergent ion beam and a rf cavity can be utilized for temporal bunch compression of the ion beam. The Z4 target chamber at the end of the beamline offers space for diagnostics.

a laser driven proton beamline, starting with the laser-driven proton source in the Z6 target chamber [46]. In figure 1.1 the subsequent solenoid and rf cavity are depicted, together with the target chamber Z4, which offers space for diagnostics at the end of the beamline.

Within the scope of the construction and characterization of the laser-driven proton beamline S . Busold et al. demonstrated the efficient transport of laser-driven protons with a pulsed solenoid combined with a rf cavity for energy compression culminating in proton bunches at kinetic energies of 9.7 MeV with a *full width half maximum* (**FWHM**) energy spread of $(2.7 \pm 1.7)\,\%$, containing $(1.7 \pm 0.3) \times 10^9$ protons at a distance of 3.0 m from the target [45]. Optimizing the temporal bunch compression capabilities offered by the rf cavity resulted in proton bunches with average kinetic energies of 7.8 MeV and FWHM durations of (462 ± 40) ps, containing at least 1.5×10^8 protons at 6 m distance from the target [39].

In addition to the original goals of the LIGHT project, such as a conceptual study to provide an additional compact ion beamline for plasma physics experiments at the *facility for antiproton and ion research* (**FAIR**) and the investigation of laser-driven ion sources as an alternative to conventional accelerators for special applications [46], one specific application has aroused interest - the investigation of ion stopping in dense plasmas. Theories about energy deposition of ions in dense plasmas are of great interest to inertial confinement fusion, because of its dependency on the α-particle heating [50]. Long standing expertise and experimental capabilities at the plasma physics group at GSI [51] and recent success [52] make an encouraging environment for a continuation of these investigations.

The LIGHT beamline offers sub-nanosecond proton bunches with very high intensities and could therefore eliminate two major problems of previous stopping power experiments. The first is the low signal-to-noise ratio, caused by x-rays and EMPs stemming from the dense plasma, which is generated with nanosecond laser pulses, and the overall low ion numbers per bunch that can be provided by the UNILAC. Increasing the ion number per bunch by a factor of 1×10^4 with the LIGHT beamline will remedy this problem. The second problem is the relatively long bunch duration of the UNILAC beams (5.5 ns FWHM), leading to an averaging effect of the stopping power, because of hydrodynamic expansion of the plasma during probing by the ion bunch.
However, only proton beams have been generated, transported and temporally compressed within the LIGHT project. As the energy loss of ions in plasmas scales with the effective charge state Z_{eff} of the ion,

$$E_{loss} \propto Z_{eff}^2, \tag{1.1}$$

energy loss measurements based on *time of flight* (**ToF**) methods are not sensitive enough to resolve the energy loss of protons in plasmas accessible with non-multi-kJ laser systems. Therefore it is absolutely necessary to investigate the possibilities of the generation, handling and transport of laser-driven mid-Z ion beams within LIGHT.
A successful demonstration of transport and temporal compression of heavy ion beams with kinetic energies in the range of one MeV per nucleon will make LIGHT the ideal probe beam for stopping power measurements and will open up new opportunities for a range of plasma physics experiments, e.g. pump-probe experiments with either the nhelix laser as driver and the LIGHT beamline as probe beam or the other way around.

1.2 Thesis structure

This thesis is dedicated to the three major parts of the LIGHT project, namely: generation, transport and bunch compression. After a short introduction to the relevant laser-ion acceleration mechanism in chapter 2, a detailed description of the experimental realization of a laser-driven heavy ion source and its characterization is presented in chapter 3.

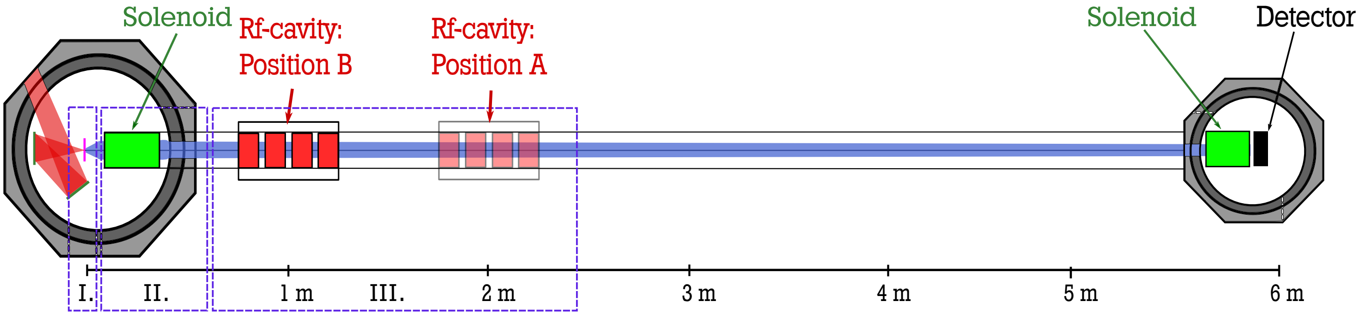

Figure 1.2: Overview of the LIGHT beamline, consisting of a laser-driven ion source (section I), a pulsed solenoid for collimation and energy selection (section II), a movable rf cavity for bunch compression (section III) and an additional target chamber for diagnostics at the end of the beamline. The laser-driven ion source will be introduced and discussed in chapters 2 and 3, collimation and transport in chapter 4 and temporal bunch compression in chapter 5.

Collimation and energy selection capability of a pulsed solenoid are investigated in chapter 4. Modifications of the LIGHT beamline for optimum bunch compression of ion bunches, together with first results are presented in chapter 5. Chapter 6 concludes this thesis and gives an outlook for further development of the LIGHT project.

2 Principles of laser-driven ion acceleration

Contrary to the implication of the title, the ions are not directly driven by the high intensity short pulse laser because of their high mass. Instead for intensities up to $10^{24}\,\mathrm{W\,cm^{-2}}$ electrons gain energy from the laser-matter interaction and in turn transfer a part of this energy to the ions. To be able to understand this two stage process, the following chapter is divided into two parts: the interaction of the laser pulse with electrons and the subsequent acceleration of the ions. More precisely the first section gives a simple picture of the interaction of the intense laser pulses with single electrons and atoms, followed by the collective interaction of the laser pulse and the resulting plasma. The ensuing acceleration of ions will be explained with the well understood target normal sheath acceleration, which happens to be the only relevant acceleration mechanism within the scope of this work. This chapter is concluded with a more detailed treatment of ionization mechanisms and rates in quasi-static electric fields. The descriptions of all phenomena are based on references [9, 53, 54, 55], if not stated otherwise.

2.1 Laser field interacting with single particles

In the presented work, all the laser pulses were linearly polarized. Therefore in the case of a laser propagating in a vacuum in the z-direction, the electric and magnetic fields **E** and **B** can be described as

$$\begin{aligned}\mathbf{E} &= E_0\mathbf{e}_y e^{i(\mathbf{kz}-\omega_L t)},\\ \mathbf{B} &= \tfrac{E_0}{c}\cdot(-\mathbf{e}_x)e^{i(\mathbf{kz}-\omega_L t)},\end{aligned} \tag{2.1}$$

where E_0 is the electric field amplitude of the laser, c is the speed of light in a vacuum, ω_L the laser angular frequency, $\mathbf{k}$ the laser wave vector, $\mathbf{e}_{\mathrm{x,y}}$ the unit vectors perpendicular to the laser direction of propagation and t the time. Generally the electric field amplitude E_0 itself depends on the time t, but varies only slowly compared to the laser oscillation period and thus is taken to be constant until further notice. An electron with mass m_e and velocity $\mathbf{v}$ in electromagnetic fields is subject to the Lorentz-force

$$\frac{\mathrm{d}}{\mathrm{d}t}(\gamma m_e \mathbf{v}) = -e(\mathbf{E}+\mathbf{v}\times\mathbf{B}). \tag{2.2}$$

The *Lorentz*-factor γ is necessary for the treatment of charged particles in relativistic regimes and denotes $\gamma = 1/\sqrt{1-v^2/c^2}$, whereas e is the charge of the electron. In case of non-relativistic velocities $v << c$ the **B**-field can be neglected and the force acting on the electron depends only on the **E**-field. The resulting equation of motion describes a harmonic oscillator with the quiver velocity in the x-direction

$$v_{osc} = \frac{eE_0}{m_e\omega_L}. \tag{2.3}$$

From equation 2.3 it may be seen, why ions are assumed to be stationary. The quiver velocity depends inversely on the mass of the particle and is very small for ions since $m_{ion}/m_e \geq 1836$. Assuming a laser wave length of $1\,\mu$m the quiver velocity of the electrons approaches the speed of light for intensities larger than $1.37 \times 10^{18}\,\mathrm{W\,cm^{-2}}$, which is still much below experimental capabilities. Therefore one can distinguish between relativistic and non-relativistic laser-electron interactions with the dimensionless parameter

$$a_0 := \frac{v_{osc}}{c} = \frac{eE_0}{m_e \omega_L c} = \sqrt{\frac{I_0[\mathrm{W\,cm^{-2}}]\lambda_L^2[\mu\mathrm{m}]}{1.37 \times 10^{18}}}. \tag{2.4}$$

For the calculation of a_0 the relativistic mass increase is neglected. Therefore relativistic laser-electron interaction is characterized by $a_0 > 1$. In the relativistic regime the magnetic field can no longer be ignored. The electrons, oscillating in the y-direction, then experience an additional force, the $\mathbf{v} \times \mathbf{B}$ drift, which leads to the drift velocity v_D in the z-direction.

$$v_D = \frac{a_0^2}{4 + a_0^2} \tag{2.5}$$

As long as the relativistic laser field acts on the electron, it will get pushed in the laser direction of propagation. The distance travelled by the electrons in the y-z-plane, depicted in figure 2.1, depends on the laser intensity, expressed in terms of a_0. However, there is no continuous energy transfer onto the electron and after the laser pulse has passed by, the electron is at rest again. This is also known as the Lawson-Woodward theorem [56].

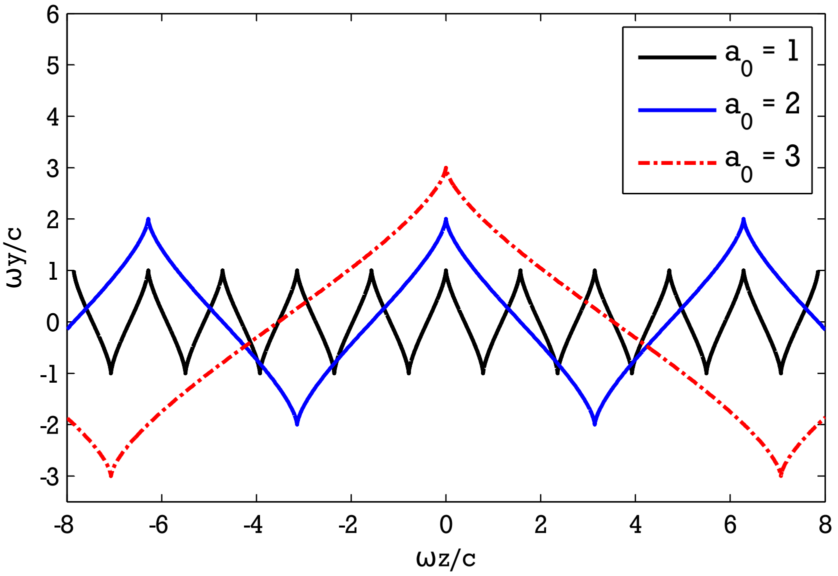

Figure 2.1: Trajectories of electrons in relativistic laser fields of plain waves propagating in z-direction plotted in terms of the dimensionless parameters $\omega \cdot y/c$ and $\omega \cdot z/c$. The electrons were at rest before the arrival of the laser pulse. For increasing intensities (a_0) the electron can travel further in the z-direction during the laser pulse.

2.1.1 Ponderomotive force

As long as the laser is treated as a plane wave, it is impossible to transfer any amounts of energy from the laser field on to the electron that still remains after the laser pulse has passed. However, focussed laser pulses cannot be treated as plain waves, which is especially true for high intensity short pulse lasers. To achieve the highest intensities, the laser pulse with a duration below 1 ps is focussed down to a μm-sized spot. For high laser powers the intensity gradients in such a diffraction-limited focal spot are sufficiently large to influence the laser-electron interaction. In addition to the quiver motion due to the rapid oscillation of the laser field, the electrons are forced away from high intensity regions of the laser field. This force is called *ponderomotive force* and was reported as early as the 19th century by Paul Drude [57]. In a more modern approach in 1957 Boot and Harvey derived the ponderomotive force as the low-frequency force, that an inhomogeneous oscillating electromagnetic field imposes on a charged particle. A non-relativistic laser field as given in equation 2.1, but with a field amplitude changing in the y-direction ($E_0 = E_0(y)$), acts on electrons via the Lorentz force as described in the beginning of section 2.1:

$$\frac{\mathrm{d}v_y}{\mathrm{d}t} = \frac{-e}{m_e} E_y(y(t), t) \tag{2.6}$$

To deduce an equation for the ponderomotive force one divides the motion of the electron in an oscillatory part y_o and a motion of the oscillation center y_c, see equation 2.7 [9]. If one then performs a Taylor series expansion of the electric field $E_y(y(t), t)$ with respect to y_c, one ends up with equation 2.8.

$$y(t) = y_o(t) + y_c(t); \quad \langle y_o(t)\rangle = 0; \quad \langle y(t)\rangle = \langle y(t)_c\rangle = y_c; \quad y_o(t) \ll y_c(t); \tag{2.7}$$

$$E_y(y(t), t) = E(y_c(t), t) + y_o \cdot \frac{\mathrm{d}}{\mathrm{d}y} E(y_c(t), t) \tag{2.8}$$

In the lowest order, the electron oscillates in the same way as in section 2.1, the only difference being the dependence of the oscillation amplitude on the position y. Inserting y_o and time averaging the second order of the electric field over one oscillation period, results in

$$\frac{\mathrm{d}v}{\mathrm{d}t} = -\frac{e}{2m_e\omega_L^2} E(y_c(t)) \frac{\mathrm{d}}{\mathrm{d}y} E(y_c(t)) = -\frac{e}{4m_e\omega_L^2} \frac{\mathrm{d}}{\mathrm{d}y} E(y_c(t))^2, \tag{2.9}$$

which is called the ponderomotive force. Equation 2.9 can be rewritten to fit the general case and then the *ponderomotive potential* Φ_p becomes apparent.

$$\mathbf{f}_p = -\frac{e}{4m_e\omega_L^2} \nabla \mathbf{E}^2(\mathbf{r}) = -\nabla \Phi_p \tag{2.10}$$

A relativistically correct equation of the ponderomotive force is obtained in [58].

$$\mathbf{f}_p = -m_e c^2 \nabla \bar{\gamma}; \qquad \bar{\gamma} = \sqrt{1 + a_0^2/\alpha} \tag{2.11}$$

Here $\bar{\gamma}$ is the time averaged Lorentz factor over the duration of one laser cycle. α is a factor depending on the polarization of the laser and equals 2 for linear polarization. A solution of the resulting equations of motion is only feasible numerically, but the gained kinetic energy W_p and the angle θ relative to the direction of laser propagation of the electrons when exiting the laser-electron interaction can be determined analytically:

$$W_p = (\bar{\gamma} - 1) m_e c^2, \tag{2.12}$$

$$\tan^2(\theta) = \frac{2}{\bar{\gamma} - 1} \tag{2.13}$$

In experimental studies [59] a widely approved estimate for the ponderomotive potential in terms of laser intensity I_L and wavelength λ_L has been found, which is also supported by numerical simulations.

$$\Phi_p = m_e c^2 \left(\sqrt{1 + \frac{I_L[\mathrm{W\,cm^{-2}}]\lambda_L[\mu\mathrm{m}]}{1.37 \cdot 10^{18}[\mathrm{W\,cm^{-2}}]}} - 1 \right) \tag{2.14}$$

2.1.2 Single atom in the laser field - Ionization

For the understanding of the collective behaviour of electrons in laser fields, the question of how the electrons are freed from the confinement of the atom has to be tackled first. In most laser-driven ion acceleration schemes the laser interacts with atoms and creates a plasma in the process. One possible mechanism for creating a plasma of ions and electrons out of a formerly solid material is the so called *photo ionization*. An atom is excited by absorbing a photon and relaxes this excitation by releasing an electron [60]. For this process to happen the photon has to carry sufficient energy to at least overcome the Coulomb potential of the bound electron. Since typical high power lasers generate wavelengths in the visible or infra-red spectrum and the ionization potential is in the order of several eV, photo ionization is not a relevant mechanism for laser-matter interactions within the scope of this work.

However with rising intensities the probability for the "simultaneous" absorption of multiple photons rises as well and enables the so called *multiphoton ionization* (**MPI**) [61]. The probability of ionization exhibits a resonant behaviour, when photon energies are comparable to the difference between virtual states. In the case of most high power lasers the necessary number of photons for ionization is sufficiently high to suppress this resonant behaviour so that the ionization rate Γ can be written as

$$\Gamma = \sigma_n \cdot I_L^n, \tag{2.15}$$

where σ_n is the cross-section of the n-photon transition. If $n \cdot \hbar\omega$ exceeds the ionization threshold by at least $\hbar\omega$, then the process is called *above threshold ionization*. Multiphoton ionization starts to become a relevant process at laser intensities of $10^{12}\,\mathrm{W\,cm^{-2}}$ [53]. A completely different ionization mechanism requires the atomic potential to be disturbed by the laser field. This is the case, when the field strengths of laser field and atomic fields are in the same order of magnitude. A simple estimate with Bohr's atomic model yields an intensity of $3.5 \times 10^{16}\,\mathrm{W\,cm^{-2}}$ at which

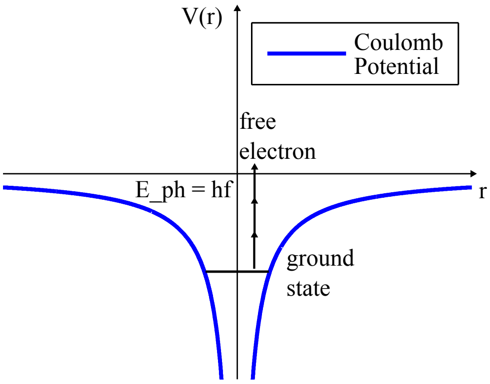

Figure 2.2: Multiphoton ionization: for high intensity laser fields, the Coulomb potential can be overcome by the "simultaneous" absorption of multiple photons.

the laser field is as strong as the electric field of hydrogen. The deformation of the atomic potential in the presence of strong electric fields is depicted in figure 2.3. For intensities much below the afore mentioned estimate the Coulomb barrier is already significantly deformed. As soon as a significant part of the evanescent wave functions of the electrons reaches the far side of the Coulomb barrier, electrons can tunnel through the barrier (see figure 2.3 a)) [62]. Therefore this mechanism is called *tunnel ionization*. Laser intensities above $1.4 \times 10^{14}\,\mathrm{W\,cm^{-2}}$ for hydrogen deform the Coulomb barrier severely, so that electrons can leave the atomic confinement freely (see figure 2.3 b)). Consequently this ionization mechanism is named *barrier suppression ionization* (**BSI**). Tunnel ionization and BSI can be summarized as field ionization mechanisms. To determine the different regimes of ionization mechanisms in terms of laser intensity one can use the Keldysh parameter [63].

$$\gamma_K = \omega_L \sqrt{\frac{2E_{ion}}{I_L}} \tag{2.16}$$

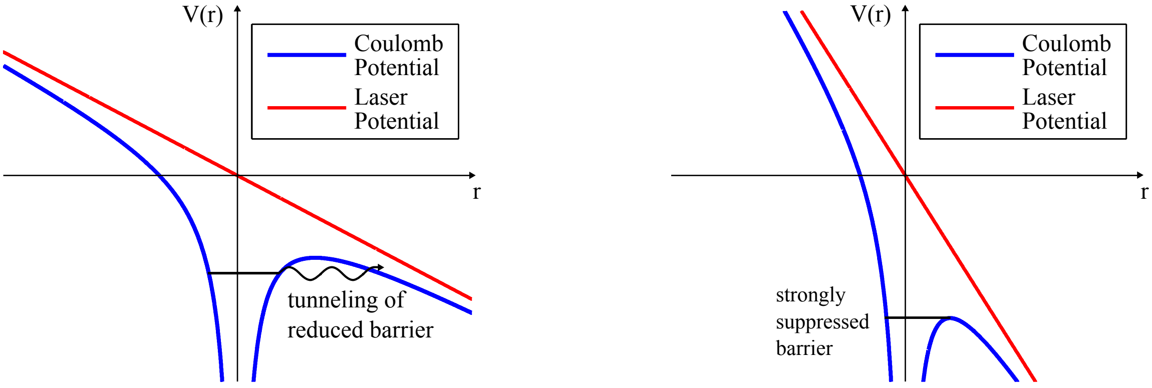

(a) (b)

Figure 2.3: Schematic display of field ionization, a), and barrier suppression ionization, b). The Coulomb potential is deformed by the presence of a laser field (potential).

E_{ion} denotes the ionization energy the of electron in its unperturbed ground state. A Keldysh parameter of $\gamma_K \gg 1$ indicates MPI and $\gamma_K \ll 1$ field ionization as the dominant ionization mechanism. The transition for hydrogen at $\gamma_K = 1$ takes place at $7 \times 10^{13}\,\mathrm{W\,cm^{-2}}$ for wave lengths of $1\,\mu$m.
According to the already described ionization mechanisms significant ionization should appear only at laser intensities above $10^{12}\,\mathrm{W\,cm^{-2}}$. However in reality ionization and breakdowns do occure at intensities as low as $10^{9}\,\mathrm{W\,cm^{-2}}$. This means that another ionization mechanism is present in many-particle-systems under the influence of high intensity laser radiation. Free electrons, stemming from contamination with weakly bound electrons or from photo ionization with UV-light, are accelerated in the laser field [53]. When they collide with bound electrons, they transfer energy and possibly ionize atoms. Therefore the process is called *collisional ionization* (**CI**). A more detailed investigation of collisional ionization and barrier-suppression ionization in the case of quasi-static electric fields can be found in section 2.4.

2.2 Laser-plasma interaction

After considering the interaction of high power lasers with single particles, the following section is dedicated to the collective interplay between plasma and laser. The laser propagation in plasmas is followed by an overview of relevant energy transfer mechanisms.

2.2.1 Laser propagation

When displaced by external fields, the electron gas of the plasma will be compressed locally, while the ions stay immobile. The resulting coulomb force strives to restore the homogenous electron density, which leads to an oscillation of the electrons. The frequency of this rapid oscillation depends only on the electron density n_e and is called *plasma frequency* [55]

$$\omega_p = \sqrt{\frac{e^2 n_e}{\epsilon_0 m_e}}, \tag{2.17}$$

where ϵ_0 denotes the vacuum permittivity. A laser field propagating through a plasma interacts with these plasma oscillations and in turn is influenced by them. By approximating the plasma linearly as a dielectric and solving the resulting wave function of a transverse electromagnetic wave in this dielectric, one ends up with a dispersion relation for the laser propagation.

$$\omega_L^2 = \omega_p^2 + k^2 c^2 \tag{2.18}$$

As long as $\omega_L > \omega_p$ the wave vector k is real and the laser can propagate. But in the case of a positive gradient of the electron density n_e in the direction of propagation, at a critical electron density n_c the wave vector becomes imaginary meaning that the laser is reflected. The critical electron density follows from equations 2.17 and 2.18 and can be approximated as

$$n_c = \frac{\epsilon_0 m_e \omega_L^2}{e^2} \approx 1.1 \cdot 10^{21} \left(\frac{1}{\lambda_L[\mu\mathrm{m}]} \right)^2 \mathrm{cm}^{-3} \tag{2.19}$$

Opaque plasmas are also called *overdense plasmas*. The skin depth of the evanescent laser depends on the difference of plasma and laser frequency. A smaller electron density gradient leads to a greater skin depth.

$$L_{skin} = \frac{c}{\sqrt{\omega_p^2 - \omega_L^2}} \tag{2.20}$$

2.2.2 Electron acceleration

In this section the energy transfer from the laser to the electrons in overdense plasmas is discussed. The absorption mechanisms can be grouped into two major categories - collisional and collisionless absorption. The collisional absorption mechanism hinges on the symmetry breaking of collisions of electrons with ions in the presence of a rapidly oscillating strong electric field. In this mechanism, also known as *inverse bremsstrahlung* [53], an electron absorbs a photon while interacting with the strong electric field of an atom or ion. This is the reversal of bremsstrahlung, hence the appropriate name. The collision frequency $\nu_{electron-ion}$ is of paramount importance for this process.

$$\nu_{electron-ion} \propto \frac{n_e}{T_e^{\frac{3}{2}}} \tag{2.21}$$

The more energy the laser deposits into the plasma, the higher the electron temperature T_e becomes and the lower the importance of the collisional absorption because of the decreasing collision frequency. At an intensity of around $10^{15}\,\mathrm{W\,cm^{-2}}$ collisionless absorption mechanisms start to dominate, the first one being the *resonant absorption* [64, 65]. P-polarized electromagnetic plain waves with non-zero angle of incidence with respect to the boundary surface of the critical density drive an electron-plasma wave resonantly beyond the critical density. Because of the damping of this plasma wave, the laser can transfer up to 50 % of its energy in this process. As a result only electrons from the narrow region of interaction gain large amounts of energy, leading to very hot electrons.

For equal polarization and incident angle of the laser, but very steep electron density gradients the *not-so-resonant absorption*, first proposed by Brunel in 1987 [66], is the main heating mechanism. The steep density gradient leads to a small penetration depth of the laser. The electric field component perpendicular to the critical density surface accelerates electrons from this surface into the thinner plasma and then back towards the critical density during the first half-cycle. The electrons then enter the overdense plasma at maximum velocity, where the laser field cannot act on them any more, because of the small skin depth. Hence energy was transferred very efficiently from laser to electron, thus generating a small quantity of very fast electrons.

Intensities exceeding $10^{18}\,\mathrm{W\,cm^{-2}}$ trigger the $\boldsymbol{j} \times \boldsymbol{B}$*-heating*, proposed in 1985 [67]. The laser-electron interaction being relativistic enables the $\mathbf{v}\times\mathbf{B}$-term of the Lorentz force. Necessary condition is again a steep density gradient and small skin depth, but the process works best for normal incidence and is almost independent of s- or p-polarization. Electrons are accelerated in the same scheme as in the *not-so-resonant absorption*, only here the $\mathbf{v} \times \mathbf{B}$-term drives the acceleration with double the frequency ω_L.

Over a wide range of intensities, different absorption mechanisms are contributing to the heating of a plasma and the generation of a fast electron population. Typical high power high energy sub-picosecond laser systems exhibit a relatively low intensity laser foot (see figure 2.4 for the shape of this pre-pulse) with contrast levels from 10^{-7} to 10^{-12} as long as nanoseconds before the main pulse. These intensities are sufficient for ionization of the target and preheating of the resulting plasma. The main pulse reaches peak intensities of up to $10^{21}\,\mathrm{W\,cm^{-2}}$ and creates hot electrons with the above mentioned mechanisms. Since the injection of electrons into the laser field is random, the energies of the hot electrons should be distributed around a central value. However, from theoretical studies with PIC simulations [68, 69] an exponentially decaying electron distribution $n_{e,hot}$ is often assumed.

$$n_{e,hot}(T) = n_{e,0} \cdot \exp\left(-\frac{E}{k_B T_{e,hot}}\right) \tag{2.22}$$

The temperature equals the ponderomotive potential Φ_p (see work by S.P. Hatchett et al. [15]) given in section 2.1.1 and $n_{e,0}$ can in turn be calculated from total laser energy E_L, average electron energy $k_B T_{e,hot}$ and laser spot size r_0. The following estimates are taken from [70] and work by M. Roth and M. Schollmeier published in [71].

$$k_B T_{e,hot} = \Phi_p = m_e c^2 \left(\sqrt{1 + \frac{a_0^2}{\alpha}} - 1\right) \tag{2.23}$$

For a linear polarized laser α should be 2, but an extensive study in [70] of published data for the electron temperature found $\alpha \approx 1.14$.

$$n_{e,0} = \frac{\eta E_L}{c \tau_L \pi r_0^2 k_B T_{e,hot}}, \tag{2.24}$$

with η being the conversion efficiency of laser energy to kinetic energy of the electrons, c the speed of light in vacuum and τ_L the duration of the laser pulse.

$$\eta = 1.2 \times 10^{-15} I^{0.74} [\mathrm{W\,cm^{-2}}] \tag{2.25}$$

2.3 TNSA - a laser-driven particle acceleration

Having explained the basic principles of high power short pulse laser interaction with matter, the next section is dedicated to the phenomenological discussion of a laser-driven particle acceleration scheme called target normal sheath acceleration, which is widely seen as the most robust of all proposed laser-driven ion acceleration schemes. This section is based on references [14, 15, 17, 34, 54, 72, 73]. Special attention is directed to the characteristics of the resulting ion beam. The process can be divided into four stages, which are displayed in figure 2.4. A high energy short pulse laser is focussed down to a spot size between $5\,\mu$m and $50\,\mu$m radius. The low-foot of the laser pulse preceding the main pulse generates an expanding plasma (see figure 2.4 a)). At the same time a shock wave, driven by the ablation pressure of the laser, starts propagating through the target. After a significant part of the laser energy is transferred to

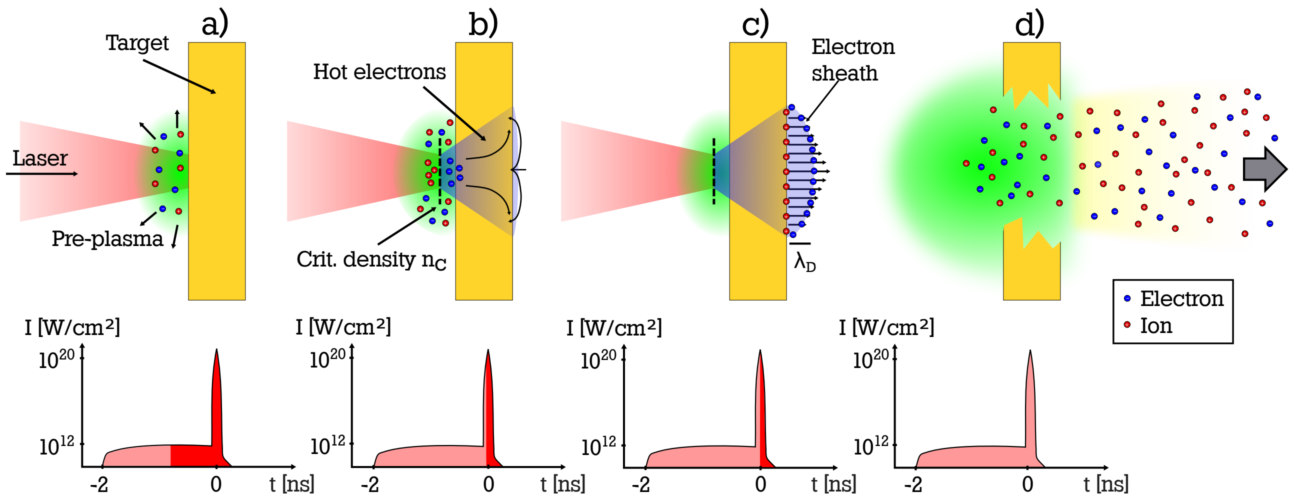

Figure 2.4: Time resolved schematic of the target normal sheath acceleration. a) The low intensity foot of the laser pulse ignites a plasma on the front side of the target and launches an ablation shock wave into the target. b) Electrons gain energy from the interaction with the laser pulse and get pushed to the rear side of the target. The laser can only interact with the plasma up to the critical plasma density. While propagating through the target, the electrons experience Coulomb small angle scattering, which broadens the divergence distribution of the electrons. c) Fast electrons leave the target and thus contribute to the increasing positive charge of the target. Slower electrons are held back by the resulting electric field and form an electron sheath at the rear side. The atoms on the rear surface are ionized by BSI and are accelerated in the electric field. d) Ions and electrons propagate in a directed plasma expansion perpendicular to the target rear surface. For as long as the laser pulse persists, hot electrons from the target front surface contribute to the acceleration of the ions. As soon as the ablation shock wave reaches the rear surface, the target is destroyed.

hot electrons, by the mechanisms outlined in section 2.2.2, these electrons propagate through the still solid target. They leave the laser-plasma interaction zone in the direction of laser propagation with an angular distribution $\tan(\theta) = \sqrt{2/(\bar{\gamma}-1)}$, only depending on the electron energy (see equation 2.13). The transversal source size is the laser spot size, usually between $5\,\mu$m and $50\,\mu$m radius. For short pulse lasers with pulse lengths in the sub-picosecond time scale the resulting electron current exceeds the Alfvén limit by orders of magnitude [74, 75]. To counteract the self-generated magnetic fields, which prevent the electrons from propagating, return currents of cold electrons are generated. The hot electron beam is filamented, with each filament carrying up to one Alfvén current, and return currents encasing them. The thicker the target, the more the filamentation breaks down, which is also visible in resulting ion beam profiles. While propagating through the target material, the electrons undergo multiple Coulomb small-angle scattering processes. This broadens the electron beam significantly and has been calculated by M. Schollmeier [70] with H.A. Bethe's theory of multiple scattering [76]. The process is depicted in figure 2.4 b).

The fastest electrons are able to leave the target completely and therefore start to charge up the target. This electric potential is increased by means of charge separation until the electrons start to recirculate back into the target and a dynamic equilibrium is developed with electrons oscillating around the positively charged target rear surface. A one dimensional analysis by M. Passoni et al. [77, 78] of the resulting electrical field taking the hot electron distribution $n_{e,hot}$ from equation 2.22 into account yields an equation for the electric sheath field $E(z)$ on the rear side of the target.

$$E(z) = \frac{2k_B T_{e,hot}}{e} \frac{1}{z + \sqrt{2}\lambda_D} \tag{2.26}$$

The extent in the z-direction of the field is determined by the Debye length λ_D, which is a measure of the scale of significant charge separation in plasmas.

$$\lambda_D = \sqrt{\frac{\epsilon_0 k_B T_{e,hot}}{e^2 n_{e,0,rear}}} \tag{2.27}$$

From these equations it becomes apparent, that the electron density on the rear side of the target $n_{e,0,rear}$ is of utmost importance for the TNSA mechanism. The approximated value for $n_{e,0,rear}$ is derived from the hot electron density on the front side of the target, equation 2.24, and the broadening stemming from the propagation through the solid target with thickness d [54, 70].

$$n_{e,0,rear} = n_{e,0,front} \frac{r_0^2}{\left(r_0 + d\tan\frac{\theta}{2}\right)^2} \tag{2.28}$$

$$\approx 1.5 \cdot 10^{19} \frac{r_0^2}{\left(r_0 + d\tan\frac{\theta}{2}\right)^2} \frac{I[10^{18}\,\mathrm{W\,cm^{-2}}]^{7/4}}{\sqrt{1 + 0.73 I[10^{18}\,\mathrm{W\,cm^{-2}}]\lambda^2[\mu\mathrm{m}^2]}} \tag{2.29}$$

Calculating the Debye length with this electron density on the rear side with equation 2.27, and inserting the result then into equation 2.26 for $z = 0$, gives an estimate for the maximum electric field strength at the rear surface.

$$E_{max} = 5.2 \cdot 10^{11} \cdot \frac{r_0^2}{\left(r_0 + d\tan\frac{\theta}{2}\right)^2} \cdot I[10^{18}\,\mathrm{W\,cm^{-2}}]^{7/8} \tag{2.30}$$

The resulting fields in figure 2.4 c) are in the order of $10^{12}\,\mathrm{V\,m^{-1}}$ and are sufficient to ionize atoms on the rear surface by barrier-suppression ionization (see section 2.4). For standard targets without any special cleaning or treatment, the surface atoms consist to a considerable extent of hydrocarbons and water vapor [79]. Therefore after ionization the surface layer is comprised mainly of protons and carbon, oxygen and target material ions with varying charge states. The surface ions are then accelerated along the field lines of the electric field, which are perpendicular to the target surface because the target surface is conducting, hence the appropriate name target normal sheath acceleration. However, since the sheath of electrons is supplied by a constant stream of electrons from the front side, which follow a broad angular distribution, the sheath and therefore the equipotential surfaces are bell-shaped [34]. Thus, when accelerated along the field lines, the ions experience a large angular spread. The outermost layer of ions (in the laser propagation direction) experiences the highest field and therefore gains energy (equal to the electric potential of the sheath field) up to several 10 MeV. From the second layer inwards the ions are exposed to a diminished field, because the positive charge of the outer ions screens the field effectively. This is also the explanation for the formation of a spectrally very broad, towards higher energies exponentially decaying energy spectrum with a sharp cut-off at the maximum energy.

The screening of the electric field also plays an important role in the efficiency of the acceleration of each ion species. The higher the charge to mass ratio of the ions, the faster the ions are accelerated, meaning that these ions travel in the front of the ion bunch and screen the field for ions in their wake. This self-enforcing mechanism ultimately leads to protons being accelerated up to 10s of MeV per nucleon, whereas heavier ions from surface contaminations or the target itself reach only a fraction of that velocity.

For the efficient formation of these electric fields it is important to choose the target thickness according to the speed of the shock wave caused by the laser ablation pressure on the front side. In the case where the shock wave reaches the rear side of the target before the charge separation and build up of the electron sheath by hot electrons from the laser-plasma interaction are complete, the sheath will be distorted by the shock wave breakout. Since the sound velocity of the ions depends on the temperature of the pre plasma, which in turn depends on the intensity of the low-foot of the laser pulse, control of the contrast is especially important for thin targets [80, 81].

The subsequent propagation of the mixed ion and electron beam (see figure 2.4 d)) has been modelled with a plasma expansion model by P. Mora [82] or J. Fuchs [83] or with quasi-static models by M. Passoni [77]. However only characteristics of the ion beams such as maximum energy of the ions and to some extent the energy spectrum of the ions may be determined analytically. For studies of angular divergence or expansion of the beam one has to fall back on numerical simulations, realized for example with PIC simulation methods [84, 85, 86].

2.4 Ionization mechanisms - theory and rates

The target normal sheath acceleration mechanism relies on a very fast ionization of the atoms on the rear surface for the ions to take advantage of the sheath field. In the case of heavy ions, such as carbon or fluorine, the process becomes more complicated, because the ionization potentials of the different charge states span more than one order of magnitude. There are two possible ionization mechanisms, the barrier suppression ionization and the collisional ionazation, both of which were touched on briefly in section 2.1.2. This section will introduce mechanisms and analytical estimates for the ionization rates in order to understand the measured ion spectra presented later in chapter 3. It is based on work by B.M. Hegelich [16, 87, 88]. The analytically estimated ionization rates are utilized in section 3.2.1 to calculate values for the rates expected for the presented laser-ion acceleration parameters.

2.4.1 Field ionization

The hot electrons, stemming from the laser-plasma interaction on the target front side, form a sheath field on the rear side, which is in the order of $10^{12}\,\mathrm{V\,m^{-1}}$. This has been shown by M. Roth et al. [89] and A. J. Mackinnon et al. [90] among others. In the presence of static electric fields of this magnitude the atomic Coulomb potential gets distorted (see figure 2.5). On one

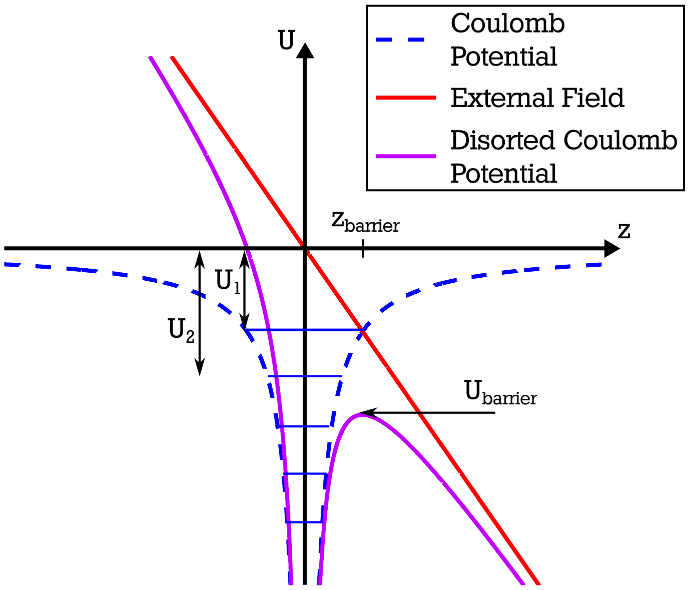

Figure 2.5: Schematic representation of the barrier suppression ionization. The presence of a strong external electric field causes a distortion of the atomic Coulomb potential. This leads to the formation of a barrier potential, which in case of the BSI is below the upper atomic levels of the electron shell. Electrons, whose energy level in the potential exceed the level of the barrier, are no longer confined and leave the atom in an ionized state.

side the potential well is increased, whereas on the opposite side a barrier significantly below zero potential is formed. The effective atomic potential then reads as

$$U(z,t) = -\frac{eZ}{4\pi\epsilon_0 z} - zE(t), \tag{2.31}$$

where Z is the atomic number and $E(t)$ the time dependent external field. By evaluating this potential in terms of its maximum and reinserting the position of the maximum into 2.31, one can derive an expression for the height of the potential barrier.

$$\frac{\mathrm{d}U(z,t)}{\mathrm{d}z} = \frac{eZ}{4\pi\epsilon_0 z^2} + E(t) \overset{!}{=} 0; \tag{2.32}$$

$$\Rightarrow |z_{barrier}| = \sqrt{\frac{eZ}{4\pi\epsilon_0 E(t)}} \tag{2.33}$$

$$\Rightarrow U_{barrier} = \sqrt{\frac{eZE(t)}{\pi\epsilon_0}} \tag{2.34}$$

Conversely one can find the minimum value for the external field, at which the barrier U_k is of the same height as the k$^{\text{th}}$ atomic level.

$$E_{k,min} = \frac{U_k^2 \pi\epsilon_0}{eZ} \tag{2.35}$$

This classical approach to BSI conveys a first impression as to what charge states are accessible with field ionization. To calculate rates a quantum-mechanical approach by M.V. **A**mmosov, N.B. **D**elone and V.P. **K**rainov [91] is chosen. Their **ADK**-model builds on work by L.D. Landau [62] and extends his model to more complex ions and higher charge states. The ionization rate in the ADK-model is then expressed as

$$W_{ADK} = C^2_{n^*,l} \cdot f(l,m) \left(\frac{3}{\pi} \frac{E}{E_a} \left(\frac{U_H}{U_k} \right)^{3/2} \right)^{1/2} U_H \left(\frac{2E_a}{E} \left(\frac{U_k}{U_H} \right)^{3/2} \right)^{2n^*-|m|-1} \exp\left(-\frac{2}{3} \left(\frac{U_k}{U_H} \right)^{3/2} \frac{E_a}{E} \right). \tag{2.36}$$

with

$$C_{n^*,l} = \left(\frac{2e}{n^*} \right)^{n^*} \frac{1}{(2\pi n^*})^{1/2}; \quad f(l,m) = \frac{(2l+1)(l+|m|)!}{2^{|m|}|m|!(l-|m|)!}, \tag{2.37}$$

and

$$E_a = \frac{e}{4\pi\epsilon_0 a_b^2} = 0.51\,\mathrm{TV\,m^{-1}} \tag{2.38}$$

The atomic field E_a follows from the Bohr radius a_b, whereas U_H and U_k denote the potentials of hydrogen and the k$^{\mathrm{th}}$ charge state of a given ion respectively. In $C_{n^*,l}$ e stands for the Euler number e. The effective quantum number n^* together with the angular quantum number l and the magnetic quantum number m complete the description. V.P. Krainov expanded the model for the BSI [92], which then gives an estimate for the BSI rate [93]:

$$W_{ADK-BSI} \approx 6.6 \times 10^{16} \frac{Z^2}{n^{4.5}_{eff}} \left(10.87 \frac{Z^3}{n^4_{eff}} \left(\frac{E_a}{E} \right)^{1/2} \right)^{2n_{eff}-1.5} \times \exp\left[-\frac{2Z^3}{3n^3_{eff}} \left(\frac{E_a}{E} \right)^{1/2} \right]. \tag{2.39}$$

Z stands for the charge of the created ion and $n_{eff} = Z/\sqrt{U_k/U_H}$.

2.4.2 Collisional ionization

The second contribution to the ionization of the rear surface is caused by the interaction of streams of electrons with the surface atoms. Hot electrons from the front surface as well as cold electrons in the return currents can transfer energy through collisions onto the atoms and thus ionize them. A model for electron-atom collisions from Y. Kim [94], containing all possible impact parameters, was expanded by V.T. Tikhonchuk to include electron energies up to several MeVs [95]. In his work an estimation for the ionization rate was also determined.

$$W_{col} = n_e v_e \sigma_i(k_B T_e) = n_e v_e \cdot 4\pi a_B^2 \frac{U_H^2}{U_k k_B T_e} \ln\left(\frac{k_B T_e}{U_k} \right) \tag{2.40}$$

Equation 2.40 shows a decreasing ionization rate with increasing electron temperature. Thus one might expect an overwhelming contribution to the ionization rates from the cold electron return currents in the target. The rate is boosted by the much lower temperature of the electrons as well as by the equally increased abundance of this electron population. Simulations by B.M. Hegelich [88] show however that the temporal overlap of the electron return current and the surface ion population is in the order of a few femtoseconds and therefore the main ionization contribution is caused by hot electrons.

3 Laser-driven heavy ion source

Without special measures for target preparation shortly before the laser-driven acceleration takes place, no efficient acceleration of heavy ions is possible, at least not in the TNSA scheme. More advanced acceleration mechanisms, such as RPA [33, 96] or BoA [29, 31], enable the acceleration of a significant part of the bulk material, whereas TNSA is limited to the material on the target surface. The composition of the surface layer has been studied in detail for example by means of x-ray photoemission spectroscopy [79] or elastic recoil detection analysis [97]. It was found, that the surface consists mainly of hydrocarbons, water vapor and only to a lower degree of the target material. As already mentioned in section 2.3, the ions resulting from the ionization of the surface layer gain velocity in the electron sheath field according to their charge to mass ratio. Therefore, shortly after the onset of the TNSA mechanism, protons travel in the front of the ion bunch and screen the trailing ions with $q/m_u < 1$, m_u being the ion mass in terms of atomic mass units. Thus for the efficient acceleration of heavy ions it is mandatory to remove all contaminations containing hydrogen. For efficient acceleration of target atoms with $Z > 8$ it is necessary to create a completely clean surface, because oxygen ions from oxides can hinder the acceleration in similar ways to hydrogen for light ions.

This chapter is dedicated to the design, experimental realization and characterization of a laser-driven heavy ion source. A short review of different pre-shot target preparation methods is followed by an introduction of the PHELIX laser system, which is both the driver for the generation and the acceleration of the ions. Essential parameters for the TNSA mechanism, that were derived in the preceding chapter, such as electron temperature, sheath field and ionization rates in the case of complete absence of hydrogen contaminations, are calculated for the available laser parameters. The following section introduces the heavy ion diagnostics, Thomson parabola and Radiochromic Imaging Spectroscopy. The experimental setup for the source characterization is described in section 3.4. Resulting data from the heavy ion diagnostics are analysed in section 3.5 and findings are discussed in section 3.6.

3.1 Review of pre-shot target preparation methods

Pre-shot target preparation methods can be grouped into two categories. Heating of the target to evaporate adsorbed surface contamination on the one hand or a more selective energy transfer directly to the surface layer to desorb or ablate it on the other hand. The latter is generally speaking a lot more technologically advanced and requires good control of the mechanism and knowledge of the contamination layer. Heating of the target is perhaps the most brute-force method and can be achieved in a number of ways. The simplest design is to feed an electric current through a thin conducting target. Because the target is the bottleneck of the whole electric circuit, a significant power loss in the target raises its temperature and in turn increases the resistance in the case of a *positive temperature coefficient of resistance* (**PTC**) material. Therefore by controlling the current one can resistively heat the target to temperatures close to the melting point of the target material (Joule heating [98]).

Other heating methods are for example radiative heating, where broadband radiation sources are focussed onto the target rear surface, or laser heating with cw lasers. All three heating methods were tested by B. M. Hegelich et al. in several campaigns [16, 87, 88, 99] and Joule heating was found to be the most robust and successful pre-shot target preparation method. Depending on the target and coating material, they could demonstrate efficient acceleration of fluorine ions, carbon ions and palladium (see references [16, 87]). Even quasi-monoenergetic carbon ion beams have been demonstrated with this technique [99].

Methods such as sputtering the rear surface with argon ions [79], ablating it with sub-nanosecond laser pulses exceeding $10^{11}\,\mathrm{W\,cm^{-2}}$ [100] or even enabling non-equilibrium desorption processes with femtosecond laser pulses [97, 101] are much more demanding, but promise a higher level of control over the whole process. For example the origin of the protons in the TNSA mechanism could be proven by selectively removing the surface contaminations from either the front side or the rear side of the target with the help of an argon ion sputtering gun [79]. Even though increases in heavy ion cut-off energies by a factor of three in the case of femtosecond desorption [97] and a factor of two in the case of laser ablation [100] this category of target preparation methods could not emulate the success of the afore mentioned brute-force method. However, in the case of a combination of heating and laser ablation persistent surface layers of oxides could be removed in addition to hydrocarbons and water vapor.

For the design of the heavy ion source for the LIGHT project effectiveness, robustness and ease of implementation were the decisive factors and therefore the Joule heating as demonstrated by B.M. Hegelich was the method of choice for enabling efficient heavy ion acceleration.

3.2 The PHELIX laser system

The laser-ion acceleration in the LIGHT project is driven by the *petawatt high-energy laser for heavy ion experiments* (PHELIX) [7]. Using the chirped pulse amplification technique [4] in a staged configuration, PHELIX is capable of supplying laser pulses with energies up to 250 J at pulse lengths as short as 400 fs. There is also the option for laser pulses with nanosecond pulse lengths and up to 1 kJ energy, but for the scope of this work only the short-pulse laser system was relevant.

In figure 3.1 the principle layout of the laser system is depicted. The laser pulses are generated with a commercially available Ti:Sa-short-pulse-oscillator, which produces pulses with 4 nJ and 100 fs (FWHM) at a repetition rate of 72 MHz and a central wavelength of 1053 nm. An optional module for the suppression of *amplified spontaneous emission*, based on the *ultrafast optical parametric amplfication* [102], is bypassed in the experimental campaigns within the scope of this work. After passing through a stretcher the pulse exhibits a flat-top amplitude profile with 2.3 ns pulse length, a pockels-cell reduces the repetition rate to 10 Hz. Two regenerative amplifiers [103, 104] increase the output energy of the first module, the femtosecond frontend, to 30 mJ.

The pre-amplifier module expands the beam with Keppler-telescopes in several steps to keep the fluence below the damage threshold of the optics. The Keppler-telescopes have the added benefit of counteracting the beam degradation because of propagation. Two flash-pumped Nd:glass amplifiers, operated in double-pass geometry, can boost the output energy to 5 J. The heat load deposited into the glass rods of the amplifiers introduces a temperature gradient, that changes the optical properties in a spatially dependent fashion. The main result is a defocussing of the laser beam that can be counteracted with a movable lens at the end of the amplifier. Additional wavefront aberrations can in parts be corrected with a deformable mirror in the

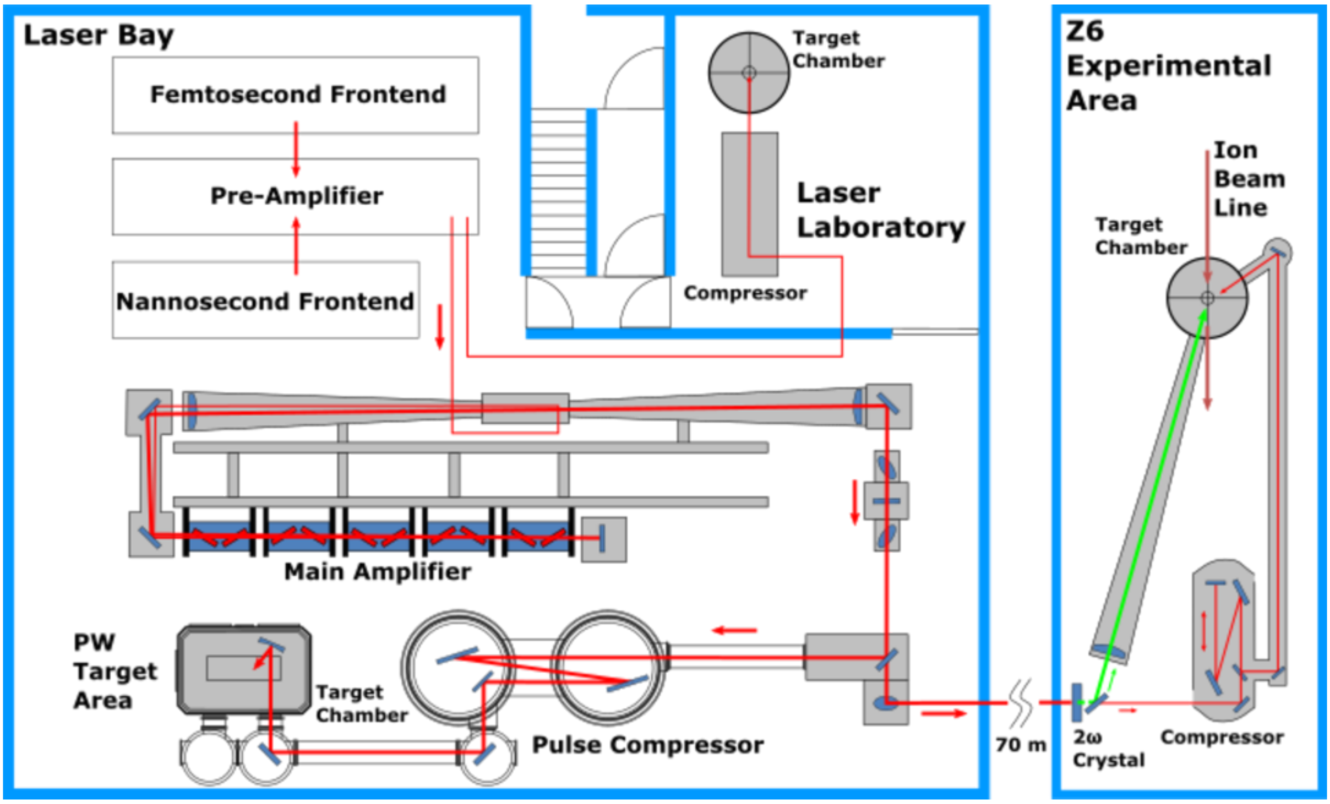

Figure 3.1: Overview of the PHELIX system and its adhering experimental areas[1]. The laser-driven ion acceleration experiments in this work were almost exclusively carried out at the Z6 experimental area.

module [105]. Therefore the cooling time of the amplifier rods limits the repetition rate of the system, in the present case to one shot every 30 s.
Last in the chain of amplifying modules is the main amplifier. The beam is expanded to 28 cm and double-passes through five slab amplifier modules with two Nd:glass discs each, enabling a maximum output energy of 1000 J. Back reflections are suppressed by a Faraday rotator.
Following the main amplifier system a switch yard is used to selectively supply one of the two experimental areas: either the petawatt target area with a full aperture beam or the Z6 experimental area with a subaperture beam with 12 cm diameter. In both cases a subsequent compressor shortens the temporal pulse lengths down to 650 fs. The diffraction gratings of the compressors have a significantly lower damage threshold and thus limit the maximum pulse energy to 250 J and 50 J for the petawatt target area and the Z6 experimental area respectively.
In a final step the laser pulses are focussed with off-axis parabolic mirrors to spot sizes below 5 μm diameter. The resulting intensities and relativistic laser parameters a_0 can be found in table 3.1.
From the laser parameters at the Z6 experimental area important parameters defining the TNSA-process can be estimated using approximations from chapter 2. They are listed in table 3.2; most importantly the maximum electric sheath field at the rear side, a defining factor for the determination of field ionization rates.

---

[1] Figure taken from *https://www.gsi.de/en/work/research/appamml/plasma_physicsphelix/phelix.htm* (May 2018)

	E_{Laser}	τ_{Laser}	Minimum spot size	Maximum Intensity	a_0
Petawatt Target Area	200 J	650 fs	3.5 μm	10^{21} W cm^{-2}	27
Z6 Experimental Area	40 J	650 fs	3.5 μm	3.7×10^{19} W cm^{-2}	5.46

Table 3.1: Capabilities of the PHELIX short-pulse laser at the two main experimental areas.

	Electron temperature $k_B T_e$	Conversion efficiency η	Electron density front side $n_{e,front}$	Electron density rear side $n_{e,rear}$	Maximum electric sheath field E_{max}
Experimental Area Z6	2.3 MeV	0.36	1.8×10^{21} cm^{-3}	5.9×10^{20} cm^{-3}	6.9×10^{12} V m^{-1}

Table 3.2: Approximated values for TNSA relevant quantities, taken from section 2.

3.2.1 Ionization rates for the Z6 experiments

In tables 3.3 and 3.4 actual ionization rates for both barrier-suppression ionization and collisional ionization for carbon and fluorine are displayed. They were calculated with equations 2.39 and 2.40 on the basis of the capabilities of the PHELIX laser at the Z6 experimental area (see tables 3.1 and 3.2).

Charge state	1+	2+	3+	4+	5+	6+
Ionization potential of carbon [eV]	11.26	24.38	47.89	64.49	392.09	489.99
Carbon ionization rate by BSI [ps^{-1}]	6×10^4	2.8×10^5	1.52×10^6	4.73×10^6	0	0
Carbon ionization raty by CI [ps^{-1}]	0.52	0.23	0.11	0.08	0.01	0.01

Table 3.3: Estimated ionization rates for carbon on the rear side of a TNSA target, driven by the PHELIX laser system at Z6 (parameters see table 3.2)

The ionization via BSI dominates the rates. However, for both carbon and fluorine the helium-like ion charge states cannot be generated by the BSI and therefore the amount of these ions should be almost negligible compared to other charge states.

3.3 Ion diagnostics

The specific features of laser-driven ion beams, such as a broad energy spectrum with a strong correlation of abundance and energy, an almost instantaneous generation and a huge divergence angle, pose a particular challenge for possible detectors. The extremely hostile environment of the laser-plasma interaction, with x-rays, hot electrons and strong EMPs, adds to the requirements for the detectors. In this paragraph two very common detection mechanisms are introduced, namely the *radiochromic imaging spectroscopy* (**RIS**) [106] and the *Thomson parabola* (**TP**) [107].

Charge state	1+	2+	3+	4+	5+	6+	7+	8+	9+
Ionization potential of fluorine [eV]	17.42	34.97	62.71	87.14	114.24	157.17	185.19	953.91	1103.12
Fluorine ionization rate by BSI [ps^{-1}]	1.4×10^5	4.5×10^5	1.12×10^6	2.06×10^6	2.50×10^6	7.4×10^5	4.3×10^5	0	0
Fluorine ionization rate by CI [ps^{-1}]	0.33	0.15	0.08	0.06	0.04	0.03	0.02	0.004	0.003

Table 3.4: Estimated ionization rates for fluorine on the rear side of a TNSA target, driven by the PHELIX laser system at Z6 (parameters see table 3.2)

3.3.1 Radiochromic Imaging Spectroscopy

When detecting laser-driven ion beams, it is especially important to monitor as many beam characteristics in one shot as possible, because shot-to-shot variations are still significant with the present level of control. With the RIS one can measure spectral properties, total particle numbers, energy resolved divergence [108] and with the right kind of target even the emittance of the beam [34]. The very first experiments discovering the TNSA mechanism already relied on the RIS [14, 15]. The cornerstone of this detection mechanism are *Gafchromic radiochromic films*, provided by *International Specialty Products, Ashland*, hence called **RCF**s. The films are sensitive to ionizing radiation [106] and change their color proportional to the absorbed dose of radiation [109]. Additionally the films are insensitive to light and exhibit a spatial resolution down to 5 μm. After irradiation they are digitized usually with a transmission scanning device.

As the penetration depths of the ions depend on their kinetic energy, a stack of RCFs with absorption layers in between can break down the spectrum of the ions spatially. An example of a stack is shown in figure 3.2 a). Consequently from doses and positions of the RCFs the spectral shape of the ion beam can be deduced. This is the key to the RIS technique [108]. Since protons display a relatively sharp peak in energy loss (Bragg peak) shortly before they are stopped, the major contribution to the dose of a given RCF stems from protons, that are stopped in this film (see figure 3.2 b)). Calculating the dose from the change in color requires a calibration of the RCFs [110], [111]. The calibration has to be repeated for each new version and batch of RCFs and has been carried out at the TANDEM accelerator at HZDR [110].

In figure 3.2 c) the dose for each RCF in the stack in a) is depicted and shows the expected behaviour for a TNSA proton spectrum. From the dose, deposited in each layer, the computation of the energy spectrum is quite demanding on computational power. A first MATLAB routine for the analysis of RCFs was developed by M. Schollmeier [70] and F. Nürnberg [112] and rebuilt by C. Brabetz [113]. The fact, that protons contribute to the dose not only in the layer they

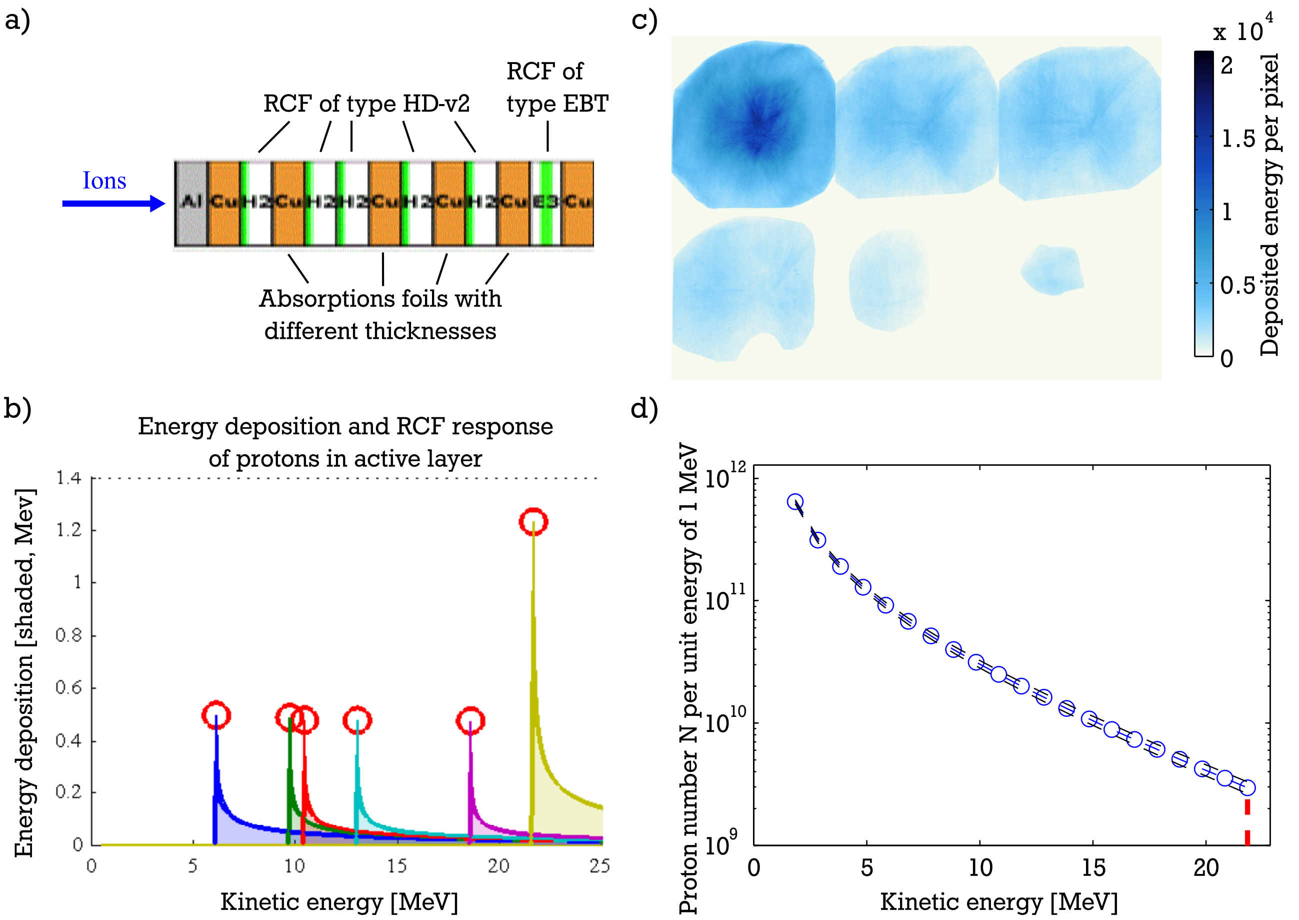

Figure 3.2: Breakdown of the Radiochromic Imaging Spectroscopy (RIS):
a) A stack of RCFs is used to measure a proton beam spectrally and spatially. Metal foils between RCFs serve as absorber to reduce the stack size and cost.
b) Protons deposit energy according to their Bragg curve, thus determining the response function. Therefore the response of any RCF is strongest for protons that get stopped within the sensitive layer.
c) The coloring of the RCFs is proportional to the deposited energy.
d) From calibrations and with the help of a software the energy spectrum of the protons can be derived. The additional black lines denote the 95 % confidence interval.

get stopped in, but also to all the layers they passed through (see equation 3.1), necessitates a deconvolution of each layer with its response function.

$$E_{dep,layer\ n} = \int \frac{\mathrm{d}N(E')}{\mathrm{d}E} \times E_{loss}(E')dE' \tag{3.1}$$

$\frac{\mathrm{d}N(E')}{\mathrm{d}E}$ represents the proton spectrum and $E_{loss}(E')$ the deposited energy in layer n. An approximation to this problem, implemented in the analysis software, is to assume a certain energy spectrum for the ions, usually an exponentially decaying one, and to calculate a convolution of this spectrum with the response function of the RCFs (figure 3.2 b)). After comparing the calculated deposited energy with the measured dose, fits are undertaken before iteratively approximating the "real" energy spectrum. In figure 3.2 d) the outcome of such an approximation with a TNSA spectrum given by J. Fuchs et al. [59] is depicted.

Regardless of all the advantages of the RIS there are limitations. The most severe limitation for this work is, that it can only be used for protons. Heavier ions suffer from a huge increase in stopping power, when compared to protons. Given the same velocity, carbon ions can only penetrate a fraction of the RCFs. Together with the much broader Bragg peak, an analysis, according to the principle described above, is impossible. On top of that, it is also almost insensitive to the charge state of the ions. In this work RCFs are only adopted to get an estimate for the spatial profile of the ion beam.

3.3.2 Thomson parabola

One viable detection method to obtain energy spectra for different ion species and charge states in one shot is the Thomson parabola. The device is named after J.J. Thomson, who used it to investigate cathode rays in the beginning of the 20th century [107]. He expanded the Wien filter, a discovery by W. Wien in 1898 [114]. After restricting a collimated charged particle beam spatially with a pinhole the beam travels through a static magnetic and electric field. The fields are parallel to each other, but perpendicular to the propagation direction of the particle beam. The motions of charged particles in electromagnetic fields are governed by the Lorentz force, see equation 2.2. If we assume the direction of propagation of the positively charged ion beam to be in the z-direction, and the fields to point in the y-direction, then the magnetic field deflects the ion beam in the negative x-direction, whereas the electric field pulls the beam in y-direction. Then the magnetic deflection (non-relativistic) reads as

$$-x_{def,mag} = \frac{qBL_B}{mv}\left(\frac{L_B}{2} + d_B\right), \tag{3.2}$$

where v is the velocity of the ions, $L_B(L_E)$ the extent of the magnetic(electric) field in the ion propagation direction and $d_B(d_E)$ the distance from the end of magnetic(electric) field to the point of measurement. Then the electric deflection is given by

$$y_{def,elec} = \frac{qEL_E}{m^2v^2}\left(\frac{L_E}{2} + d_E\right). \tag{3.3}$$

When solving equation 3.2 for $E_{kin} = mv^2/2$ and inserting this term into equation 3.3 the quadratic dependence of y on x becomes apparent:

$$y_{def,elec} = \frac{m}{q}\frac{E}{B^2}\frac{L_E \cdot \left(\frac{L_E}{2} + d_E\right)}{L_B^2 \cdot \left(\frac{L_B}{2} + d_B\right)^2} \cdot x^2_{def,mag} = a \cdot x^2, \tag{3.4}$$

hence the name Thomson parabola. The dependence of a in equation 3.4 is the reason for spatial spread of ion traces of different charge-to-mass ratios. Thus, for each distinguishable charge-to-mass ratio an energy spectrum can be derived, here from the magnetic deflection and the intensity of the ion trace on a screen.

$$E_{kin}(q,m) = \frac{q^2B^2}{2m} \cdot L_B^2 \cdot \left(\frac{L_B}{2} + d_B\right)^2 \frac{1}{x^2_{def,mag}} \tag{3.5}$$

For this set of equations to be valid, the fields need to be homogeneous and the deflection angles in both directions small. With particle tracking simulations, such as *CST Particle Studio* [115], one can avoid these limitations and use Thomson parabolas with real field geometries.

In laser-ion acceleration experiments usually the magnetic deflection is used to deduce an energy spectrum for a given ion species and charge state, because strong EMPs can couple into the condenser plates for the electric field and cause a temporal disturbance. The EMPs are emitted by the solid target acting as an antenna and driven by the sudden ejection of electrons from the target and its subsequent recharging through the target holder [116].

Thomson parabolas have been used in numerous experimental campaigns: the studies on efficient acceleration of heavy ions by B.M. Hegelich et al. ([16, 87, 88, 99]), by D. Carroll et al. [117] and many others [118, 119, 120, 121].

Almost equally numerous are the detection methods for the energy-resolved split-up ion beams. All methods have in common, that they put a screen of some sort at the end of the drift lengths after the fields. The earliest approaches utilized *California raisin 39* (**CR39**), a plastic nuclear track detector [122]. Scintillators with electron multiplying CCD cameras [118] as well as multi-channel plates [119] could be used as on-line readout for the Thomson parabola. In this work *image plates* (**IP**), provided and developed by Fuji Photo Film Co. Ltd. were adopted as screens. IPs are based on photo-luminescence, meaning excited atoms emit photons when returning to their ground states. Because of the phosophors inside the IP, the excited state can survive for hours. By exposing it to photons with the correct wavelengths, the excited states get stimulated to return to their ground states. Suitable scanners collect the *photo stimulated luminescence* (**PSL**) spatially resolved.

IPs were first developed for the application in medicine [123], but soon also incorporated in laser-plasma experiments [124]. Important features of image plates are their linear response to deposited energy by ionizing radiation [120], their good spatial resolution (down to 10 μm) and the reusability after erasing the previous signal. However the response varies strongly with type and energy of radiation. Cross calibrations with CR39 for protons [125] and for carbon ions [126] in the relevant energy range make IPs the ideal detector for Thomson parabolas.

The Thomson parabola adopted for this work was designed by D. Carroll et al. [127] and differs slightly from the design shown in figure 3.3 a). Instead of having both condenser plates parallel to the direction of zero deflection, this TP features one plate (the negative plate) with a small angle. This enables a decrease in cut-off energies due to the slow ions hitting the plate.

3.3 b) shows ion traces on the IP after scanning. For high ion energies the traces of ions with different charge-to-mass ratios melt together. The distinguishability depends on the widths of the traces on the IP, which in turn is determined by the free aperture of the pinhole. This parameter also defines the energy resolution of the Thomson parabola, which becomes worse with increasing ion energy (see figure 3.3 c)). However the main disadvantage of acquiring beam properties with a Thomson parabola is the very small solid angle covered by the pinhole. To achieve reasonable energy resolution and to be able to differentiate between ion species and charge states, it is necessary to utilize pinholes with diameters below 500 μm. Thus only a small fraction of the laser-driven ion beam enters the Thomson parabola.

There are numerous uncertainties contributing to the overall accuracy of a measurement of an energy spectrum with a Thomson parabola. On the one hand there are limitations to the energy resolution, caused by the finite width of the ion trace on the image plate. In all of the ensuing energy spectra the width was taken to include 95 % of the PSL in a perpendicular lineout of the trace. As the kinetic energy assignment to ions scales with the quadratic inverse of the distance from the no-deflection point to the point of impact on the image plate, the energy resolution becomes worse for increasing energies. On the other hand there are uncertainties connected to the determination of the number of ions from the signal intensity on the image plate. The uncertainties of the response of the image plate and the read-out and digitization with a suitable scanner are small enough to be neglected in the scope of this work. Distance of the TP to the source and the pinhole diameter necessary for the calculation of the covered solid angle can be determined with sufficient accuracy to not play a role here. The overwhelming majority of the

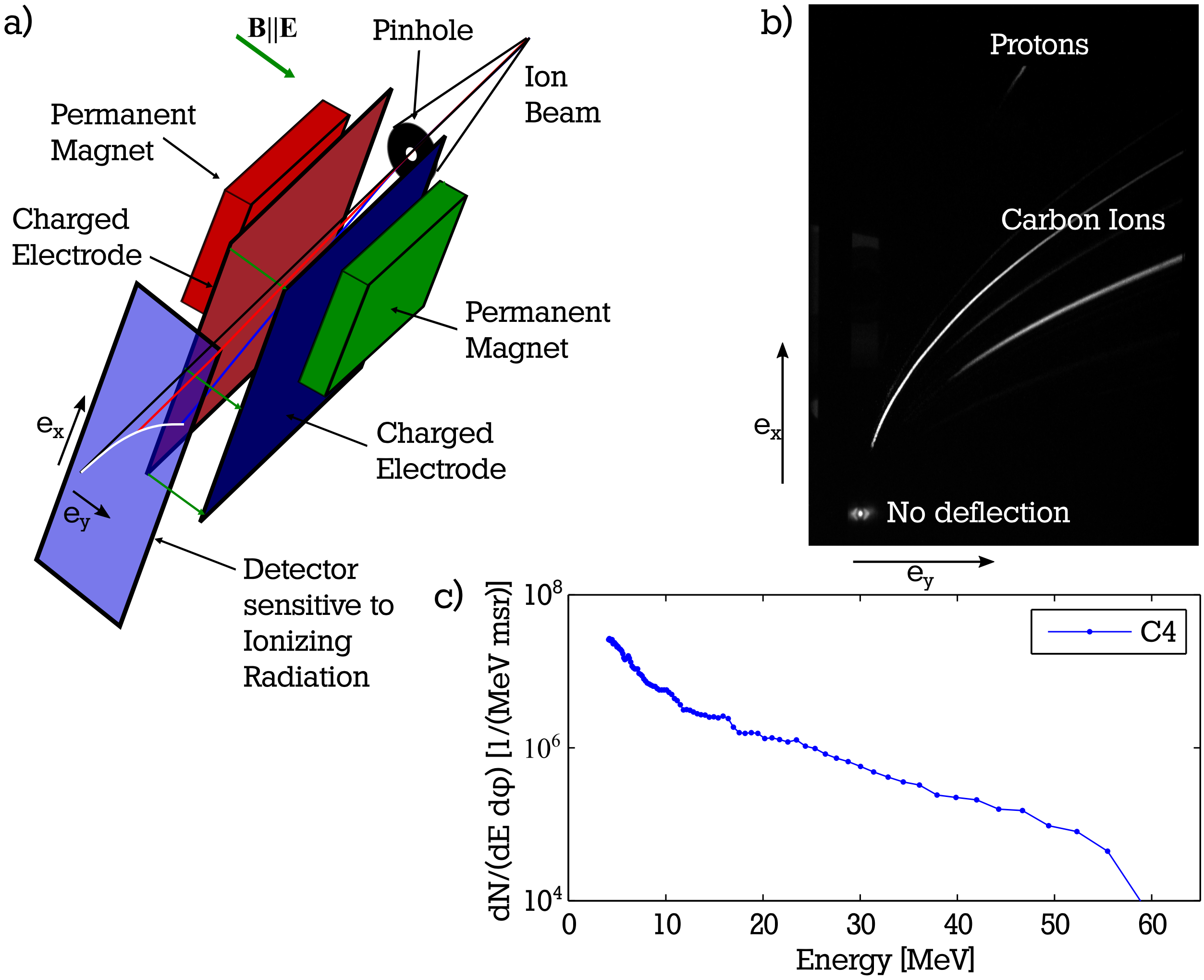

Figure 3.3: Thomson parabola for the detection of laser-driven heavy ion beams:
a) Two permanent magnets provide the magnetic field, while the electric field is added with a pair of charged copper electrodes. Positively charged ions are pulled towards to negatively charged electrode.
b) Traces of carbon ions and remnants of protons. The higher the ion energy, the closer is their point of impact to the no deflection point. Therefore at high energies the traces of ions with different charge-to-mass ratios become difficult to distinguish. The bright signal at the point of no deflection stems mainly from x-rays.
c) The signal on the image plate is resolved spectrally via the magnetic deflection and equation 3.5. Multiplying the PSL value with the IP response leads to an ion spectrum per energy unit and solid angle. The growing gaps between data points for higher energies are caused by an increase in energy bin size.

uncertainty of the number of ions per energy bin is caused by the uncertainty of the conversion of the signal in PSL into a number of ions. The only calibration available for the deduction of carbon ion quantity from an IP signal states an uncertainty of 15 % for the conversion [126]. On top of that, the uncertainty of the ion energy also adds to the conversion uncertainty; for Thomson parabola configurations in this work typically up to 5 %. By means of Gaussian error propagation an overall uncertainty of 16 % is found for the uncertainty of the ion quantity.

A defining property of a laser-accelerated ion beam is the observed cut-off energy. Because of high energetic x-rays there is a non-vanishing background signal to be found on the image plate. In this work the cut-off energy is defined as the highest kinetic energy for which the energy spectrum in terms of PSL of a given ion species and charge state barely exceeds a background energy spectrum, received for a trace of equal width close to the actual ion trace. The uncertainty of the cut-off energy is then composed of the uncertainty of the energy resolution and the statistical fluctuations of the background.

3.4 Experimental realization of laser-driven heavy ion source

Two experimental campaigns have been conducted at the experimental area at Z6 (see 1.1) in order to achieve efficient heavy ion acceleration and characterize the resulting ion beam. The first campaign took place in July 2015 and lasted one week. It was dedicated to accelerate fluorine ions, as fluorine ion beams are difficult to access by conventional accelerators, because fluorine ions are highly corrosive and therefore difficult to generate sustainably in an ion source. In a second campaign, again lasting one week, in February 2017 the efficient acceleration of carbon ions was successfully demonstrated and the divergence of carbon ion beams was examined in more detail.

The target preparation method of choice in these experimental campaigns is Joule heating, since this method was found to be the most reliable, as discussed in section 3.1. The first paragraph will detail the kind of targets, the target holder design and the temperature control for the setup of an efficient heavy ion source. The second paragraph will then outline the arrangement of the diagnostics in order to measure as many ion beam characteristics as possible.

3.4.1 Target heating

Effective Joule heating poses some requirements to the target: it has to be made from conductive material, the material must have a PTC and in order to have the highest temperatures at the target itself the resistance needs to peak at the target position. Fortunately common target designs combine all these requirements already. The only adjustments were to change the target material from gold to tungsten because of its extremely high melting point and to coat the rear side of the target with a thin layer of either carbon or calcium fluoride, shown in figure 3.4 a). The coating was applied by sputtering the material onto the tungsten foil (target laboratory at GSI), which was then cut into rectangles of 10 mm x 1 mm with the help of a femtosecond laser system at the target laboratory at TU Darmstadt.

The design of the target holding system needed to be changed from the standard design for laser-driven proton sources as well, as depicted in figure 3.4 b). Instead of holding the target in place with adhesive bonding, it needs to be clamped, mainly to ensure good conductive contacts, but also to enable the target holder to withstand the temperature increase caused by the heating

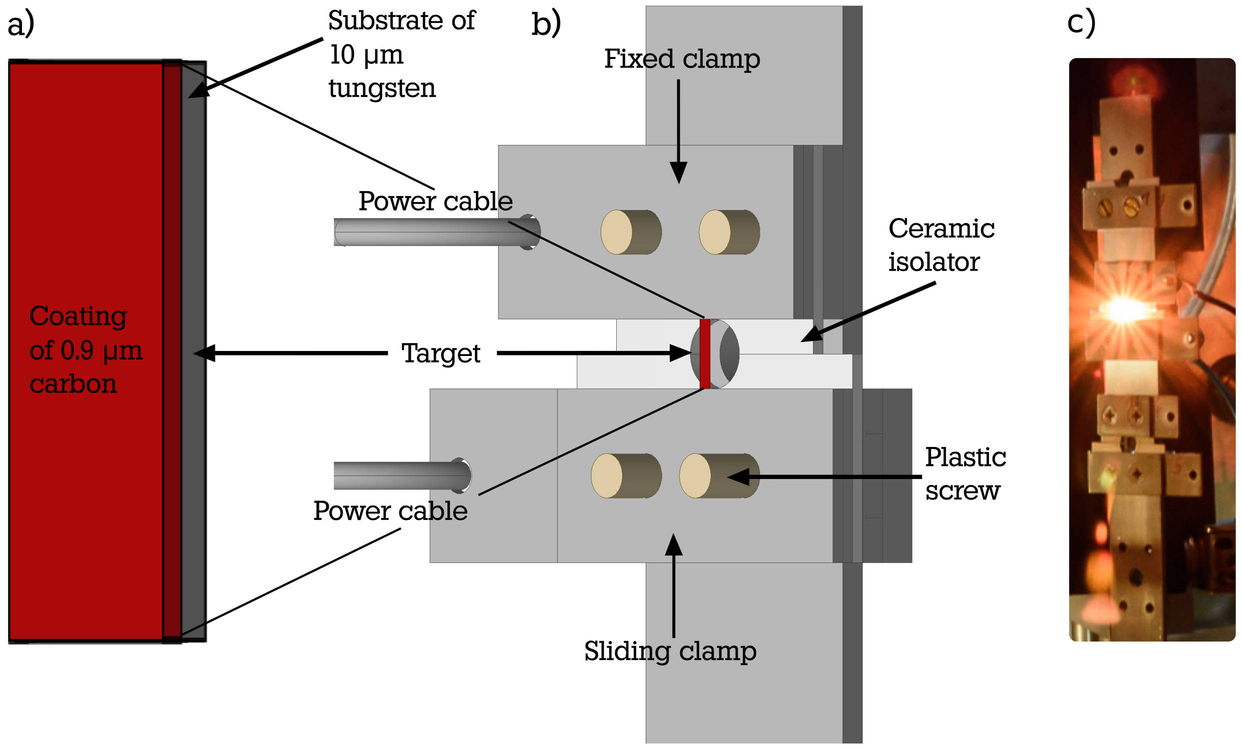

Figure 3.4: Target and target holding system:
a) The target consists of a $10\,\mu\mathrm{m}$ tungsten substrate and a sub-micrometer coating of carbon or calcium fluoride.
b) The target is clamped, with the upper clamp being fixed and a sliding lower clamp to account for heat induced elongation of the target.
c) Target heated to about 1000 °C.

of the target and to have a reusable target holding system. The current flows through one power cable, the clamps and the target and leaves through the other power cable. To prevent a short circuit with the target chamber, ceramic insulators are placed below the clamps. The connection to the target ladder is achieved with plastic screws consisting of a high performance plastic, *polyether ether ketone*. In this design the bottom clamp is free to slide, with its weight supported by the target, hence keeping the target under tension at all times irrespective of the target length. The target orientation and shape are hence correctly maintained. This is important since the heating of the target to 1000 °C is accompanied by an elongation of the target. If not compensated for, this elongation can lead to an uncontrollable bending of the target, which can deviate from the predefined TNSA-direction. When operated at temperatures around 1000 °C, the target glows similarly to a light bulb (figure 3.4 c)).
Reproducibility of TNSA-accelerated heavy ion beams demands a high level of control of the target properties. High precision manufacturing guarantees consistent thickness and coating of the target, but also the heating temperature for cleaning the target at the origin of the ion source has to be measured and controlled for all shots. By controlling the current and voltage throughput across the target the temperature of the target is determined. However, small differences in the clamped lengths of the target result in substantial differences in temperature. Assessing the temperature with sensors, such as a platinum resistance temperature detector with 1000 Ω at 0 °C (Pt1000), requires a thermal contact to the measured component, thus distorting

the temperature due to the additional thermal sink. Measuring the temperature at the fixing points of the target and inferring the temperature in the middle by simulations with COMSOL [128] is a practicable way and has been adopted for the first campaign.

A better method is to measure the temperature at precisely the point of the TNSA-source origin by utilizing a brightness pyrometer. Without any contact the temperature is deduced from the thermal radiation emanating from the target. The pyrometer, utilized in this experimental setup, is a PYROSPOT DGF 11N pyrometer from DIAS Infrared Systems. It is based on probing the intensity of the thermal radiation [129] in a measurement spot of 0.8 mm diameter at wavelengths ranging from 1.5 μm to 1.8 μm and is capable of measuring temperatures from 250 °C to 2000 °C.

Since tungsten does not behave as a black body, one has to take the emissivity into account, which is dependent on the material, surface roughness, emission angle and temperature and is certainly not constant for all wavelengths. The emissivity of tungsten at the given wavelength and surface properties was taken from studies of thermophysical properties of matter from the 1960s [130]. A major advantage of the pyrometer from DIAS Infrared Systems is, that only the lensing system for the collection of the thermal radiation has to be inside the target chamber (3.5 a)). The radiation is transported through an optical fiber to the actual pyrometer outside of

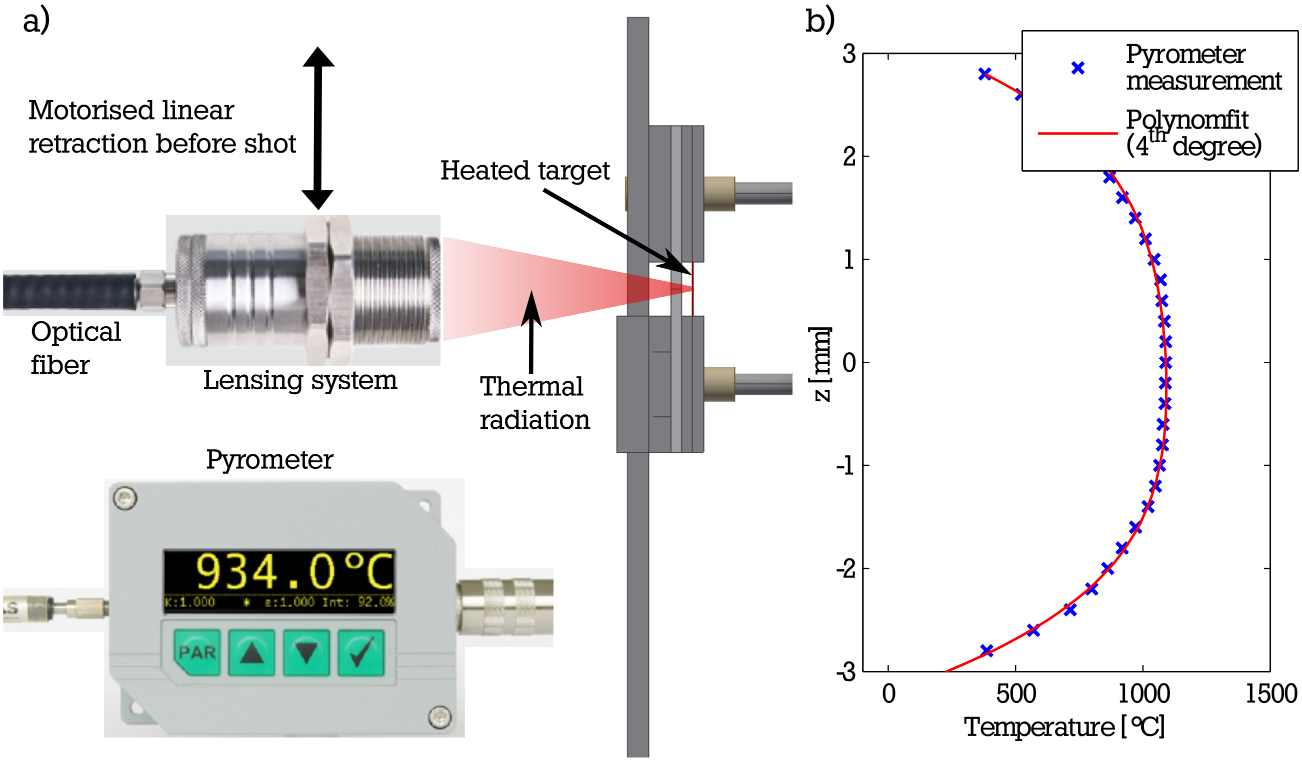

Figure 3.5: Temperature measurement of heated target:
a) Pyrometer with separate lensing system for the collection of thermal radiation and analysis device. Shortly before a shot, the lensing system is moved out to free the line of sight for PHELIX.
b) Temperature profile along the length of the target at a current of 3.4 A. The plateau-like temperature curve around the middle of the target makes for identical conditions across the small source region of a TNSA ion beam.

the chamber, which makes moving the pyrometer out of the way for the laser shot much easier. Temperature readout for a PC is available.

The power supply unit for the Joule heating is a Genesys 1U 1500 W Programmable DC Power Supply from Heinzinger, able to provide up to 15 A. It can be operated from a PC, thus enabling an online temperature regulation at a safe distance from the target chamber.

In figure 3.5 b) a temperature profile across the lengths of the target at a current of 3.4 A is depicted. As expected from simulations a fourth-degree polynomial fits the temperature profile nicely. Shooting at the middle of the target justifies the assumption of a homogeneous temperature and consequently a constant level of hydrogen elimination across the source region of the TNSA ion beam. The temperature is measured at the front side of the target, but because of the good thermal conductivity of both substrate and coating of the target, one can assume the same temperature for the coating at the rear side.

3.4.2 Diagnostics setup

The experiments took place in the main target chamber in the Z6 experimental area, introduced in section 1.1, and were driven by the PHELIX laser system with parameters detailed in section 3.2. The main diagnostics for the experimental campaigns in July 2015 and February 2017 were Thomson parabolas, for the reasons already stated in 3.3.2. RCFs with holes or slits to allow the Thomson parabolas a free line of sight were used as complimentary diagnostics in order to get some measure of the divergence of the ion beam. By using several Thomson parabolas at the same time at different angles with respect to the target rear side surface normal the divergence distribution of the ion beam could be probed in the campaign in February 2017, depicted in figure 3.6.

Experimental constraints limited the number of Thomson parabolas to three at $0°$, $-12°$ and $20°$ in the mathematical positive sense. Additionally the target can also be rotated and therefore give access to a different set of angles, always assuming rotational symmetry of the ion beam around the target rear side surface normal, which is a common assumption. A change in the angle of laser to target also influences the laser-plasma interaction, but $\pm 5°$ ought not to alter the interaction significantly. Then either the divergence distribution between $0°$ and $12°$, $0° + \beta$ and $12° - \beta$, is probed more closely, or the divergence distribution between $12°$ and $20°$, $12° + \alpha$ and $20° - \alpha$.

The orientation of the target rear side surface normal was checked and adjusted shortly before each shot, also with regard to a possible bending of the target because of uncompensated thermal elongation. Opening the target chamber after each shot and scanning the IPs after a set amount of time, guaranteed comparable results and also correct absolute particle numbers in the energy spectra of the ions.

The targets were typically heated for 10 min at constant current, while monitoring their temperature, before the pyrometer had to be moved out of the sightline of the PHELIX laser 2 min before the shot. From the temperature curve of the monitoring the actual temperature at the shot time was then inferred.

The Thomson parabolas were operated at voltages of $\pm(3.0 \pm 0.1)\,\mathrm{kV}$, resulting in a maximum electric field of $(3.0 \pm 0.1)\,\mathrm{MV\,m^{-1}}$. The maximum magnetic field at the zero deflection axis was $(0.620 \pm 0.004)\,\mathrm{T}$.

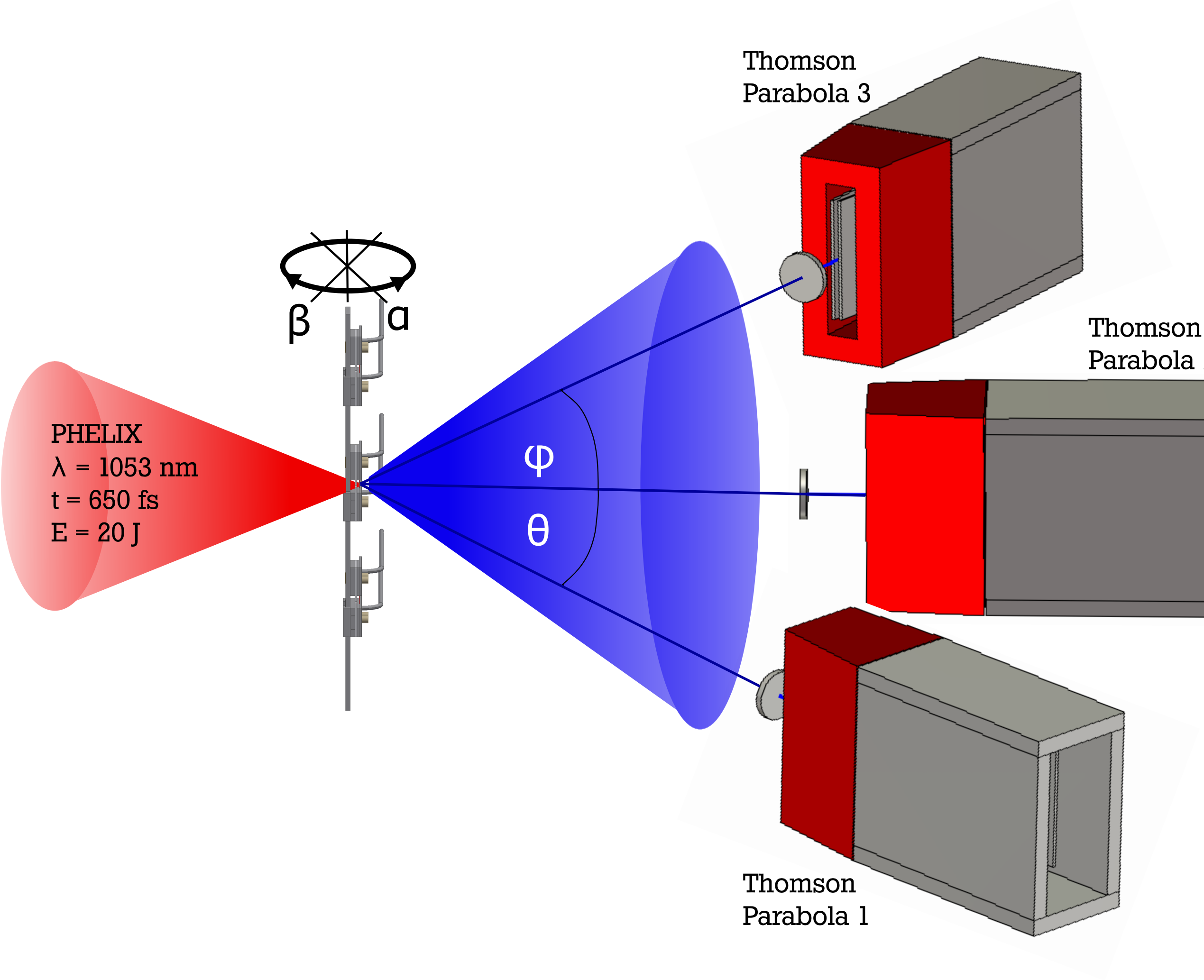

Figure 3.6: Diagnostic setup for the source characterization: The PHELIX laser is focussed onto a heated target. The charge-to-mass ratio resolved energy spectrum of the resulting heavy ion beam is then measured with Thomson parabolas. TPs at different angles with respect to the target rear side surface normal give access to the divergence distribution of the ion beam. Rotating the target increases the number of probe positions.

3.5 Characterization of laser-driven heavy ion source

The combination of pre-shot target preparation (see section 3.4.1) and ion beam diagnostics (sections 3.3, 3.4.2), together with the PHELIX laser system as driver for the laser-ion acceleration, yielded multiple sets of data for the characteristics of the ion source. The following section is dedicated to the presentation of raw data and derived energy spectra of the ions. In the first paragraph the results of the experimental campaign in July 2015 are shown. The analysis of the fluorine ion data ran into some problems, which were fixed for the experimental campaign in February 2017. In this experimental campaign the characterization of a laser-driven carbon ion source was the main focus.

3.5.1 Efficient acceleration of fluorine ions

In the campaign in July 2015 only one Thomson parabola was incorporated into the experimental setup. Therefore no statement could be made about the divergence distribution of the laser-driven fluorine ion source. RCFs of the type EBT3 with a hole in the middle to enable a free line of sight for the Thomson parabola were used to give an estimate of the transversal beam profile and are depicted in figure 3.7 a). As there was no opaque absorption foil in front of the RCFs, the speckle pattern in the RCFs is most likely caused by the post-pulse of the PHELIX laser, because the speckle imprints coincide with the laser direction and the diameter is consistent with the distance of the RCFs from the focus point of the laser.

The high stopping power of the fluorine ions prevents any colorization of RCFs beyond the second one. The line of sight of the Thomson parabola, which sits in the middle of the hole in the RCFs, had a small offset to the centre of the ion beam. The ion spectra in figure 3.7 b) are therefore the raw data of fluorine ions emanating at 2° with respect to the target surface normal direction. The pinhole of the TP covers a solid angle of 4.6×10^{-3} msr. For Thomson parabolas, this is quite a large covered solid angle, which leads to broad traces on the image plate. Fluorine ions with up to sevenfold positively charged ions can be seen on the IP together with possibly calcium ions of varying charge states. RCFs as well as the IP show data for a shot utilizing a tungsten target covered by calcium fluoride and heated to a temperature of 1400 °C. The TNSA process was driven by PHELIX with an intensity of approximately $4 \times 10^{19}\,\mathrm{W\,cm^{-2}}$.

The analysis of the ion traces with respect to their magnetic deflection leads to energy spectra for each charge state of the fluorine ions, see figure 3.8. Instead of ion numbers the ion spectra are given as luminescence in units of PSL per unit energy in megaelectronvolts and unit solid angle in millisteradian. The markings on the curves indicate the average energy of an energy bin, which is defined by the width of the trace. To calculate an ion number from the luminescence a calibration for the utilized image plate is necessary. However, in this campaign the image plates were of the type Agfa MD 40 without protective layer, for whom no response function for fluorine ions existed in literature. The IPs were evaluated and digitized using a FLA 7000 scanning device. To characterize the basic properties of the fluorine ion beam the luminescence is sufficient, but the shape of the spectra changes significantly, when including the response function of the IPs.

The previously mentioned relatively big covered solid angle of the TP leads to an uncertainty in the energy resolution of worse than 15 % at the cut-off energy of 180^{+32}_{-26} MeV for sevenfold positively charged fluorine ions (F^{7+}). The ion spectra are dominated by F^{7+} ions from as low 12 MeV onwards. The F^{7+} ion spectrum even appears to show a slight peak shortly before its cut-off energy, not unlike the mono-energetic feature discovered by B.M. Hegelich et al. [99]. Every charge state but the lowest two exhibits a plateau structure with sharp cut-off energies at both ends. This can be understood with regards to the ionization rate dependence on the electric sheath field on the rear side of the target, derived in section 2.4.1. At the beginning of the TNSA process, when the electric field is the strongest, fluorine gets ionized up to sevenfold positively, which is then accelerated most efficiently. The screening of the F^{7+} ions lowers the field until it is not strong enough to generate F^{7+} ions by means of field ionization. Then mostly F^{6+} ions are created and therefore these ions already experience a lower electric field resulting in smaller kinetic energies.

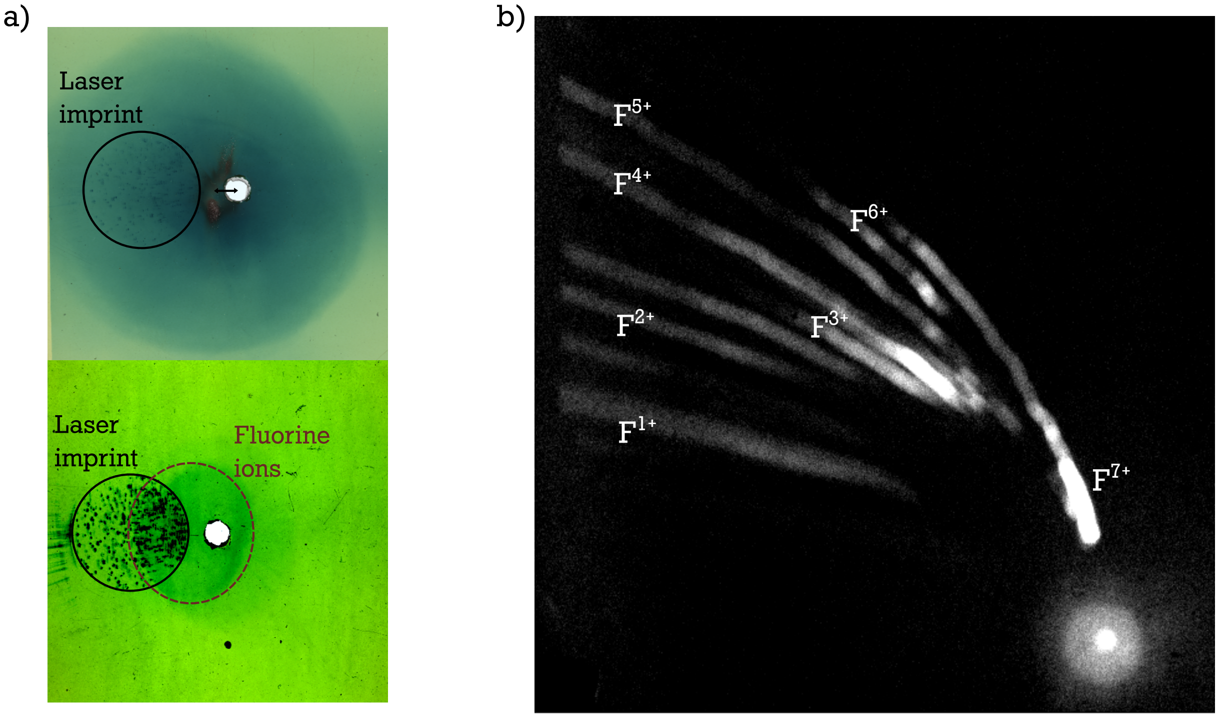

Figure 3.7: Raw data of a tungsten target with calcium fluoride coating, heated to a temperature of 1400 °C:
a) Two RCFs give an impression of the transversal profile of the ion beam. From the smaller imprint on the second RCF with adjusted contrast for better visibility an energy-dependent divergence of the fluorine ions, similar to protons, can be deduced. The speckle pattern in the RCFs stems from a post-pulse of the PHELIX laser.
b) A Thomson parabola recorded traces for fluorine ions up to sevenfold positively charged ions (enhanced contrast). Traces possibly caused by calcium ions are visible as well. The wobbly structure of the ion traces comes from the strong EMP of the laser-plasma interaction, which then couples into the capacitor plates of the TP and influences the field and therefore the electric deflection.

Another field of study was the efficiency of the acceleration of fluorine ions with respect to the temperature of the target. Diagram 3.9 displays the energy spectra of resulting protons and F^{7+} ions for three different shots. Shot 7 was taken on a target at room temperature, shot 13 at 600 °C and shot 18 at 1400 °C. Even without heating F^{7+} ions exceeding 100 MeV were generated, even though a dominating proton spectrum is observed. At 600 °C the amount and maximum energy of the protons were strongly reduced and the acceleration of F^{7+} ions was enhanced significantly. Comparing the spectra at 600 °C and 1400 °C suggests, that temperatures close to the melting point of calcium fluoride at 1418 °C leads to a reduction of the abundance of fluorine atoms on the target by sublimation, thus reducing the total number of accelerated ions. This can also be seen from an increase in pressure in the vacuum chamber.

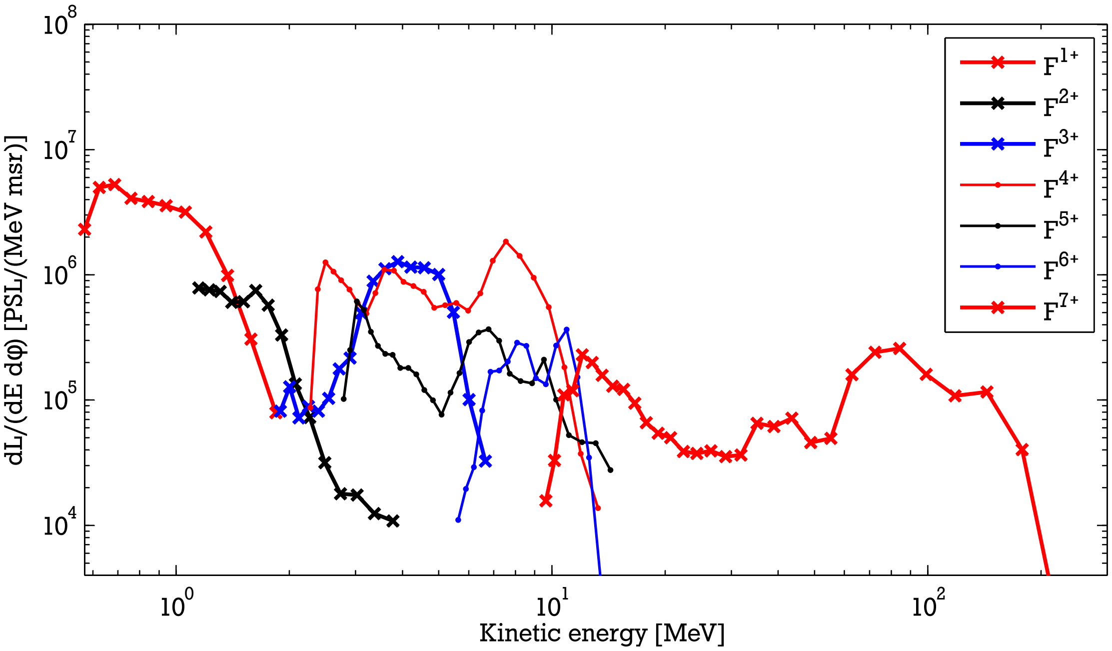

Figure 3.8: Energy spectra derived from the raw data in figure 3.7 b): F^{7+} ions dominate the spectrum from $12\,\mathrm{MeV}$ onwards and display a peak shortly before the maximum energy cut-off. The plateau behaviour of the charge states above F^{2+} is caused by the ionization mechanism.

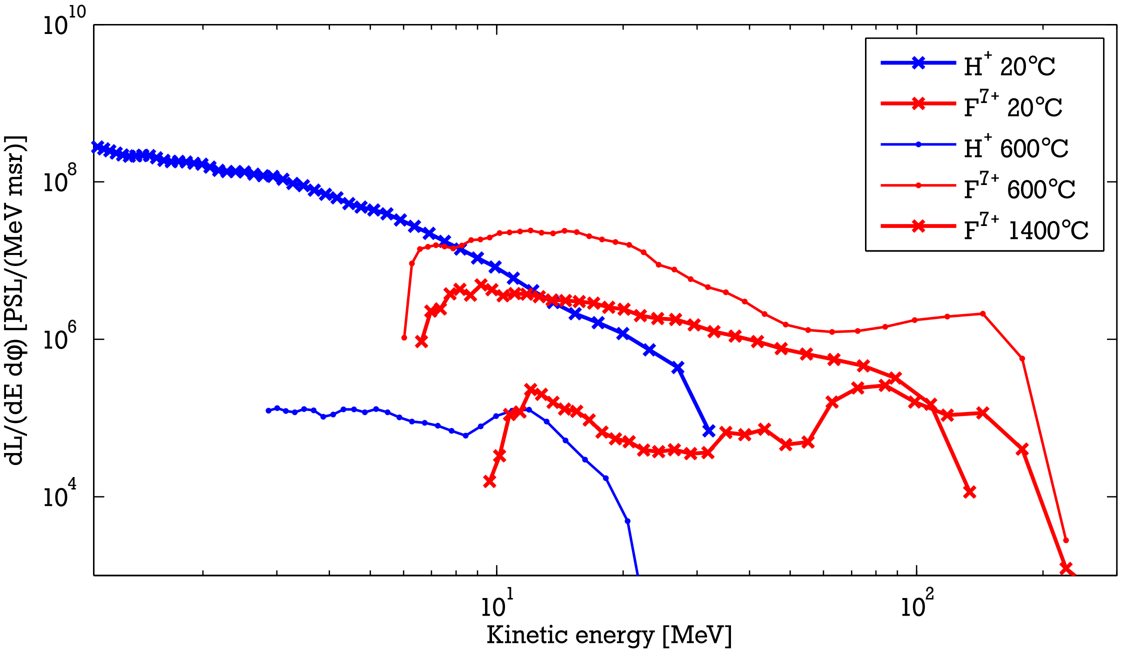

Figure 3.9: Effect of target temperature on the acceleration: Without heating F^{7+} ions exceeding $100\,\mathrm{MeV}$ were observed. Moderate heating up to $600\,^{\circ}\mathrm{C}$ leads to an enhanced acceleration of F^{7+} ions, whereas at temperatures close to the melting point of calcium fluoride the total number of accelerated fluorine ions is significantly reduced.

3.5.2 Efficient acceleration of carbon ions

The main improvement for the experimental campaign in February 2017 was to incorporate three Thomson parabolas whose lines of sight were arranged at different angles with respect to the target rear side surface normal. On top of that the distances of the TPs to the target were increased as much as possible and the pinhole diameters were chosen accordingly to improve energy resolution and guarantee distinguishable traces at high energies. By adding resistors to the plate capacitor, responsible for the electric field in the Thomson parabola, the effect of the EMP coupling could be reduced. This is also apparent from the very clear traces in figure 3.10 b) without any sign of the wobbling due to rapid changes of the electric field. An RCF was mounted 50 mm behind the target, in this campaign with a slit, to get additional information about the divergence and the pointing direction of the ion beam (figure 3.10 a)). On the image plate, displayed in 3.10 b) with enhanced contrast, carbon ion traces for singly positively charged ions (C^{1+}) up to fivefold positively charged carbon ions (C^{5+}) are visible and some remnants of protons. The corresponding Thomson parabola was recording ions emanating at 0° from

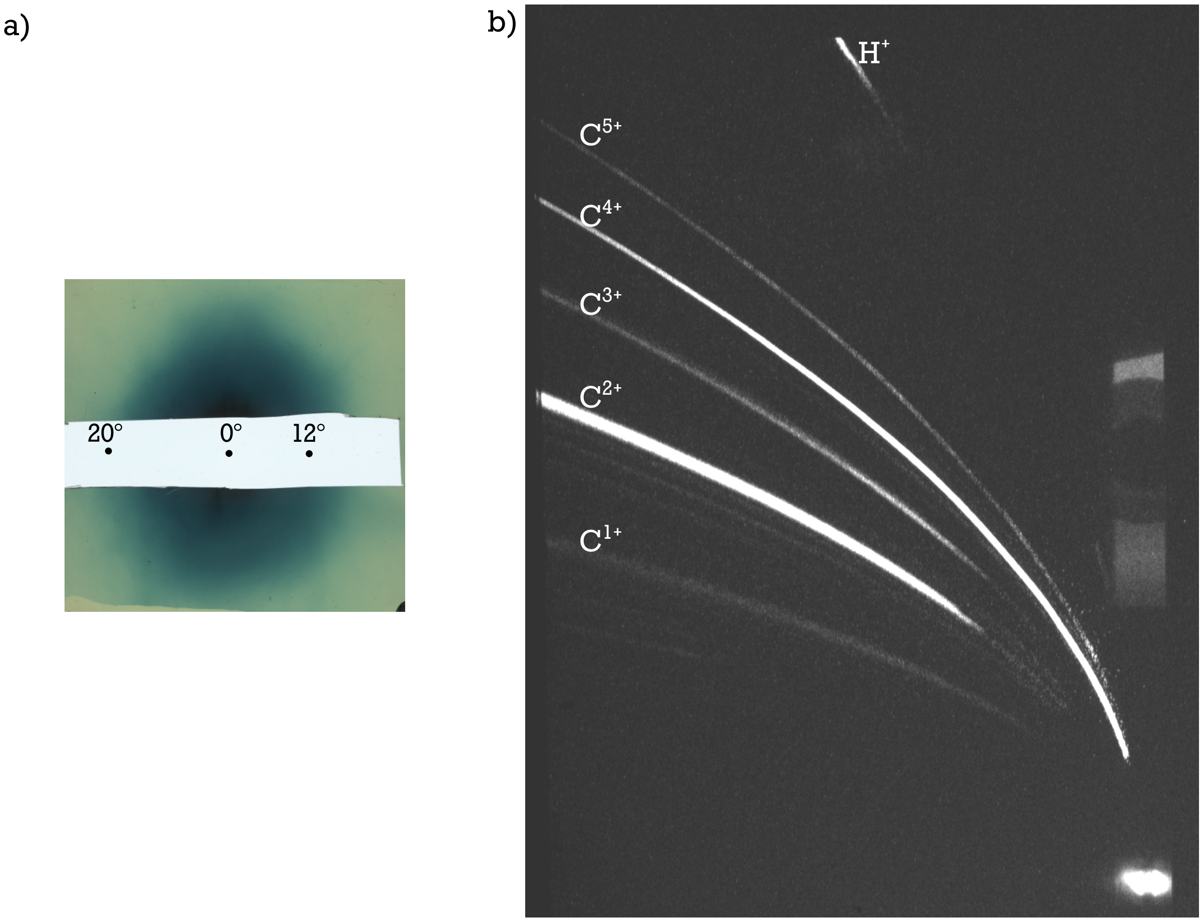

Figure 3.10: Raw data for carbon coated tungsten target, heated to 1160 °C:
a) RCF mounted in a distance of 50 mm to the target. The lines of sight of the TPs are indicated with black dots.
b) Image plate of the Thomson parabola in target normal direction displayed with enhanced contrast. All carbon ion charge states, from C^{1+} to C^{5+}, are visible as clear unperturbed traces as well as remnants of protons.

the target in a solid angle of 9.8×10^{-5} msr. In this campaign the image plates were of the type BAS-TR from Fuji Photo Film, which were already calibrated for protons and carbon ions [125, 126]. The data set was recorded for a tungsten target, coated with carbon, and heated to a temperature of 1160 °C.

The energy spectra of the observed ions, separated spatially because of their difference in charge-to-mass ratio, are shown in figure 3.11. The number of ions per unit of energy and solid angle was derived from the luminescence in PSL with the help of the response functions taken from [126] and [125]. As the luminescence fades over time even without exposure to light, a scaling is applied to refer the luminescence to a fixed delay after exposure of 30 min.

$$\mathrm{PSL}_{30} = \left(\frac{30}{t}\right)^{-0.161} \cdot \mathrm{PSL}(t) \tag{3.6}$$

Contrary to the energy spectra for fluorine ions, not the highest observed charge state dominates the spectrum, but C^{4+}. These ions reach kinetic energies of up to $68.5^{+4.8}_{-4.3}$ MeV, whereas C^{5+} ions only gain up to $33.6^{+1.3}_{-1.2}$ MeV. This can be understood, when looking at the ionization rates for carbon, calculated in section 3.2.1. The highest charge state available through the barrier-suppression ionization is C^{4+}. C^{5+} is only generated via collisional ionization by hot electrons and is almost insignificant compared to the amount of C^{4+}. It is possible, that a very small amount of C^{5+} reaches kinetic energies exceeding the cut-off energy of the C^{4+} ions, but vanishes in the non-zero background. For the C^{4+} energy spectrum the background is depicted as well in figure 3.11 as ${\mathrm{C}^{4+}}_{\mathrm{b}}$. The cut-off for each charge state at high energies as well as low energies hints at the electric field at the rear surface falling below a threshold necessary

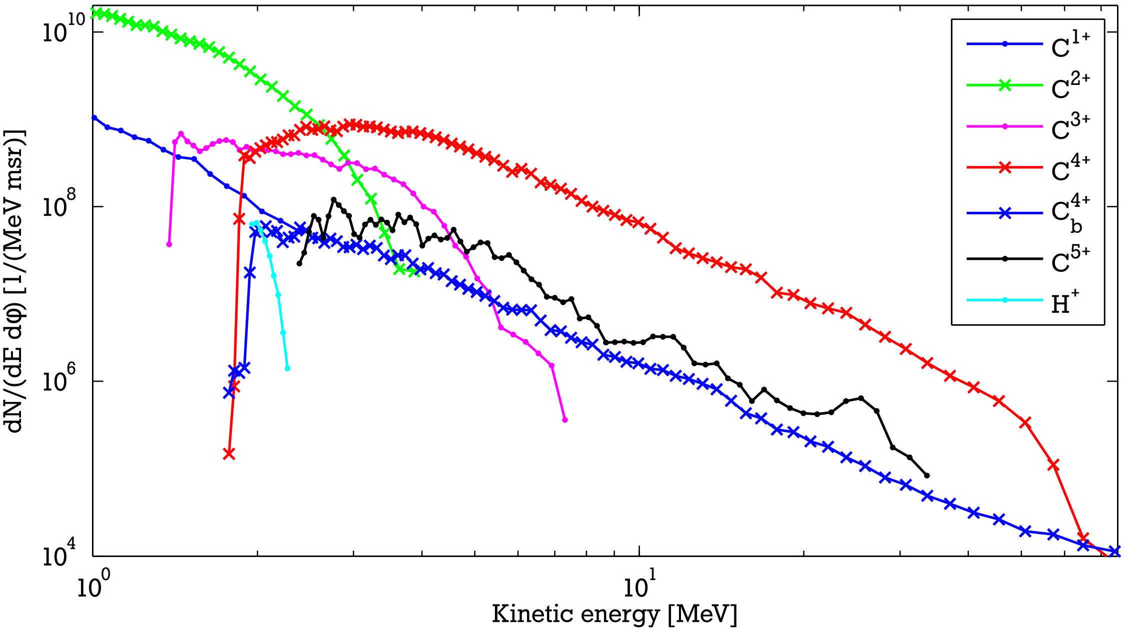

Figure 3.11: Energy spectra of ions emitted in target surface normal direction: C^{4+} was the most abundant charge state for energies above 2.5 MeV and was also accelerated to the highest kinetic energies of around $68.5^{+4.8}_{-4.3}$ MeV. The markings on the curves indicate the average energy of an energy bin, which is defined by the width of the trace.

for barrier-suppression ionization of the given charge state, before the acceleration process is completed.

The two additional Thomson parabolas, situated at −12° regarding the target surface normal and 20°, cover solid angles of 5.4×10^{-4} msr and 12.4×10^{-4} msr respectively. The most prominent ion species and charge state at these positions are again the fourfold positively charged carbon ions. In figure 3.12 the energy spectra of C^{4+} of all three Thomson parabolas are displayed, all with uncertainties calculated as outlined in 3.3.2. Additionally two spectra at −12° and 20°, which were calculated from the measured spectrum at 0° and the energy-divergence relation of protons are shown. What immediately stands out are the very similar numbers of C^{4+} ions at kinetic energies ranging from 20 MeV to 45 MeV for all of the measured spectra. At low energies the spectra exhibit a strong decrease in particle numbers for higher angles, just as expected from numerous studies of the transversal profile of laser-driven proton beams ([14, 15, 17, 54, 89, 108] and many more). However, at higher energies the course of the energy spectrum for the Thomson parabola at −12° still mimics the course of the energy spectrum for the Thomson parabola at 0° and even exceeds it. The energy spectrum deduced from the Thomson parabola at 20° peaks at 20.6 MeV despite all expectations of a much steeper decrease of particle numbers with increasing energy for such large divergence. To explain such a behaviour, the divergence has to increase with the kinetic energy of the ions, contrary to common knowledge about TNSA ion beams. This general theme is similar for all charge states.

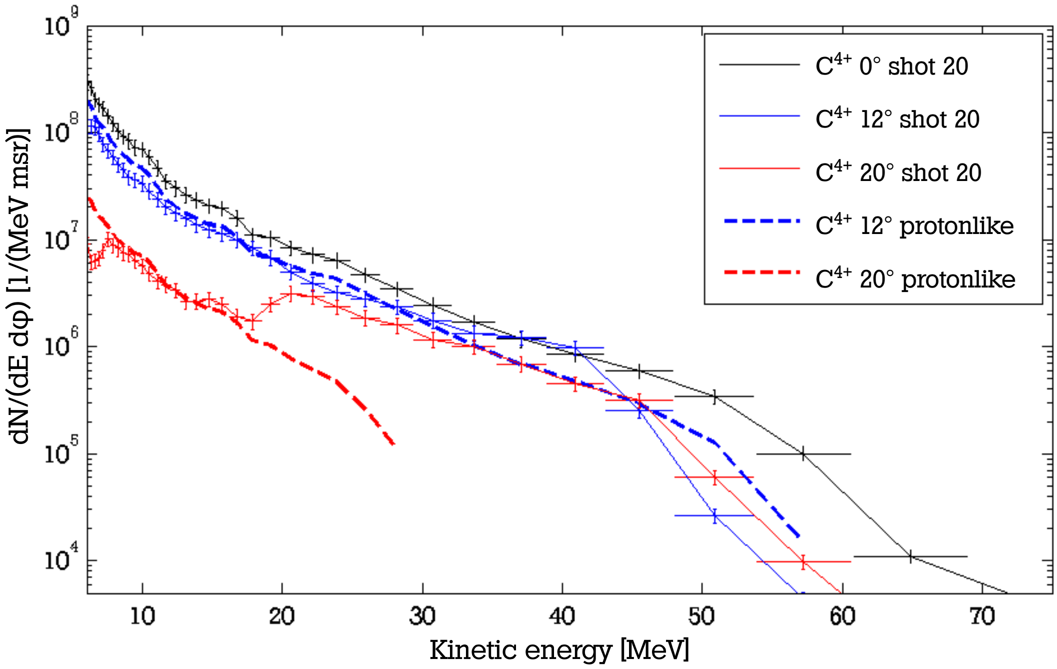

Figure 3.12: Comparison of C^{4+} energy spectra of Thomson parabolas at different angles with respect to the target surface normal: The course of the spectra at low energies is in line with the expected behaviour, inferred from the the energy-divergence relation of protons (investigated for example by [108]). At higher energies however, the three spectra approach each other. This indicates a reversed behaviour as for protons, with increasing divergence for increasing energy.

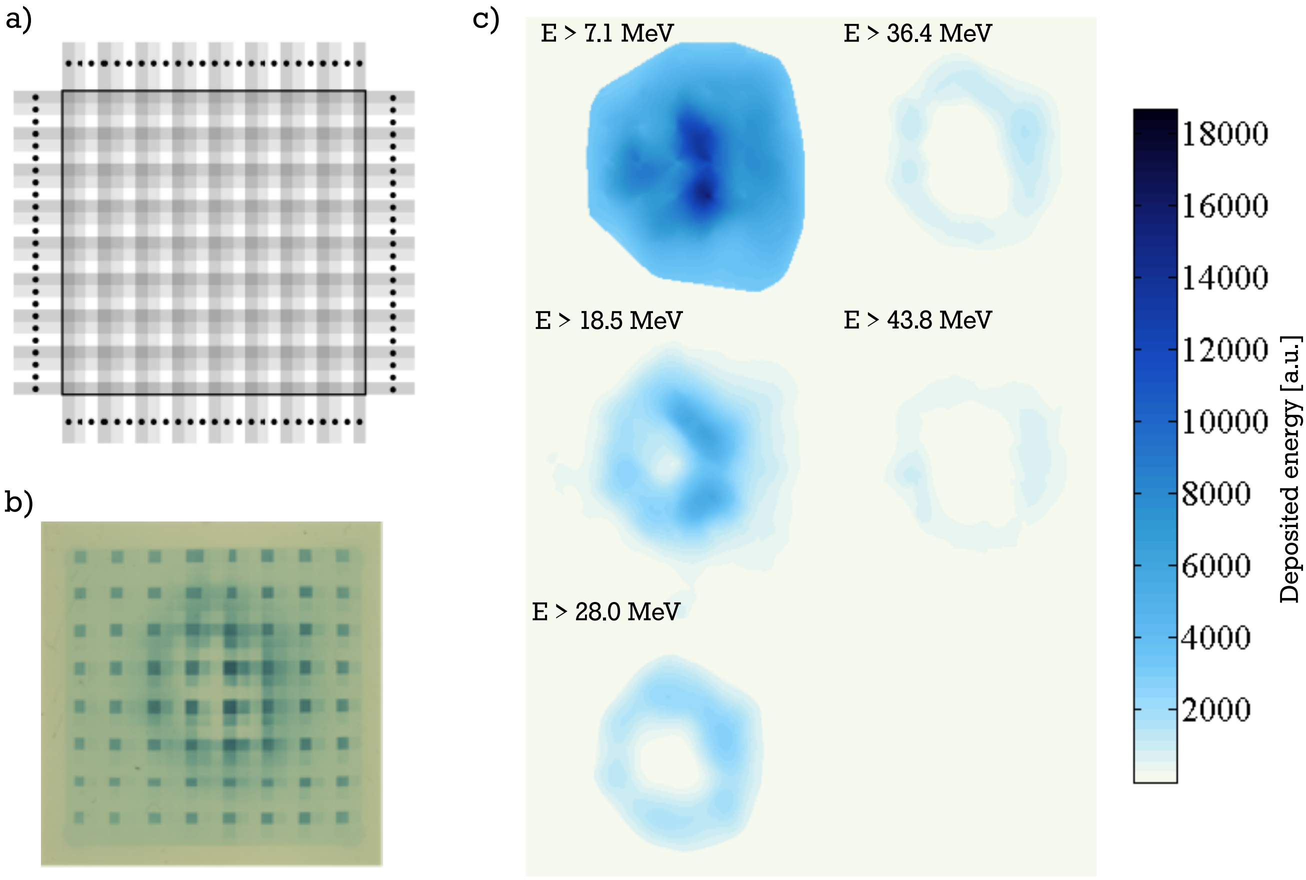

Figure 3.13: Transversal profile of a laser-driven carbon ion beam:
a) Introducing a gridded combination of absorption foils allows for the investigation of the transversal profile of heavy ion beams in several energy ranges in one shot.
b) Display of the transversal profile of a laser-driven carbon ion beam, generated with a target heated to a temperature of 1180 °C.
c) Merging all areas with a given thickness of the absorption layer and interpolating between these areas results in an emulation of an RCF stack.

The main problem of Thomson parabolas is the very small covered solid angle, thus requiring a severe approximation when extrapolating from the energy spectrum of the Thomson parabola to the whole beam. The standard RIS approach does not work for heavy ions, because of their high stopping power (see section 3.3.1). In this case a concept, used in [46], called "enhanced RIS" can remedy this problem in parts. Instead of a stack of many RCFs with absorption foils in between to get an energy-resolved transversal profile of the ion beam, a matrix of absorption foils is placed in front of one or more RCFs. This leads to a "pixelated" RCF-based detector with the advantage, that the absorption foils can be adapted to account for the increased stopping power of the carbon ions. The adjusted absorption foil matrix[2] in figure 3.13 a) consists of a 5 μm thick Aluminium base foil and stripes of 10 μm thick Aluminium foils, which create a pattern of overlapping absorption foils. Squared areas with zero to four overlapping Aluminium stripes in addition to the base foil equal areas with 5 μm up to 45 μm absorption foil in front of the radiation sensitive RCF. This enables one RCF to detect five different energy ranges in one shot. In figure 3.13 b) the outcome of this detection method is depicted. By creating images

---

[2] D. Jahn, private communication

consisting only of areas with the same thickness of absorption foil in front of them, one gets five "pixelated" RCFs at different energy ranges. An approximation of the full image can be deduced by means of bilinear interpolation between the pixels. Evaluating these approximated RCFs in terms of deposited energy produces the images in 3.13 c). For energies above 18.5 MeV a ring-like structure begins to emerge, which becomes more pronounced at higher energies. The relative uncertainty also grows at these energies because of the low signal intensity, but the trend is undeniable. From the energy spectra of the Thomson parabolas it is reasonable to assume, that the colouring of the RCF is only due to C^{4+} ions. Possible explanations for the formation of such ring structures are looked at in section 3.6.

3.6 Results and discussion

In the previous section the efficient acceleration of heavy ions by the means of laser irradiation of solid targets could be demonstrated. The ever present hydrocarbon contaminations on the surface of the foil targets were removed by Joule heating and subsequent evaporation. The impact of temperature and duration of the heating can be seen in figure 3.9. For several minutes of heating, increasing the target temperature increases the heavy ion yield and maximum energy cut-off. For temperatures close to the melting point, in the presented case of calcium fluoride at 1418 °C, the coating starts to sublimate and at the shot time only a fraction of it is left.

The ion spectra for carbon ions as well as fluorine ions exhibit distinct low energy cut-offs for all charge states but the lowest two (see figures 3.8 and 3.11). This phenomenon is directly linked to the ionization rates of the individual charge states. From the approximations of the ionization rates on the rear side of the target from section 2.4 together with the available laser parameters at the Z6 experimental area the ionization rates at the rear surface could be determined in section 3.2.1. For an intensity of $3.7 \times 10^{19}\,\mathrm{W\,cm^{-2}}$, the barrier suppression ionization is the dominant mechanism up to the helium-like charge state (only K-shell occupied by electrons). The last two electrons can only be removed by collisions with hot electrons from the target front surface. As the ionization rate for collisional ionization is smaller by at least a factor of 10^7, F^{8+}, F^{9+} as well as C^{5+} and C^{6+} are not generated or only in very small numbers.

The outermost layer of atoms at the rear surface of the target experiences the electric field used for the calculation of rates in tables 3.3 and 3.4, but for atoms further inwards this field is reduced by screening. As soon as the field falls below the minimum electric field necessary to reach the k^{th} charge state, described in equation 2.35, there will be no more generation of the k^{th} charge state but dominantly the $(k\text{-}1)^{\mathrm{th}}$ charge state. The ions experiencing the strongest electric field will be accelerated to highest velocities. While being accelerated the electric field is also further ionizing the ions up to the highest accessible charge state. By measuring the amount of neutral atoms after a drift from target to Thomson parabola, M. Hegelich et al. [88] provided proof, that the recombination rates in the expanding plasma are almost negligible. The energy spectra for heavy ions per solid angle in the target normal direction, derived in the scope of this work, are comparable to what M. Hegelich et al. found in their pioneering work [16]. The acceleration of C^{4+} ions up to kinetic energies of $68.5^{+4.8}_{-4.3}$ MeV was observed with the Thomson parabola being setup in TNSA direction. The highest observed charge state for fluorine ions, F^{7+}, reached kinetic energies of up to 180^{+32}_{-26} MeV.

Shot-to-shot variations were not investigated in detail because of the overall low number of shots at comparable parameters. However, fluctuations of the total laser energy of up to 20 %, varying focal spot sizes and changes of the overall pulse form due to aberrations in the laser system resulted in an overall variation of ion quantities by up to a factor of two. This factor is an estimate based on Thomson parabola spectra, which could be subject to very localized changes of ion beam density, and the RCFs with slit, depicted in 3.7.

The investigations concerning the transversal profile of the laser-driven heavy ion beams yielded unexpected results. Earlier investigations by for example M. Hegelich [88] or E. Brambrink et al. [131] found the divergence distribution of carbon ions to be very similar to the divergence distribution of protons with slight changes in the maximum divergence of the carbon ion beam. The comparison of energy spectra recorded by Thomson parabola situated at 0° with respect to the target surface normal, $-12°$ and 20° with the expected spectra at $-12°$ and 20° reveal a significant discrepancy at the high energy end of the spectra (see figure 3.12), that increases for higher observation angles. The expected spectra were calculated by assuming an energy-divergence relation based on proton emission data, which was experimentally observed for example in [46, 113], and scaling the C^{4+} energy spectrum in the target normal direction accordingly. Utilizing the enhanced RIS method confirms this behaviour of C^{4+} ion and suggests a ring-like structure of the transversal profile with rings emerging at kinetic energies above 18.5 MeV.

This ring structure was also observable in a standard stack of radiochromic films at the end of the experimental campaign in September 2017. The original objective of shot 70, presented in figure 3.14, was to measure the source size of C^{4+} ions by adding micro-machined grooves to the backside of the target, a method previously used by T.E. Cowan et al. [34] and F. Nürnberg et al. [108]. The focussing effect of the grooves was not visible in the RCFs, most likely because of the non-optimal shape and depths of the grooves, but in the second RCF there is a well pronounced ring-like structure. Contrary to the rings from the enhanced RIS method, there is also a smaller spot of colour in the center of the ring. This matches well with the findings of the

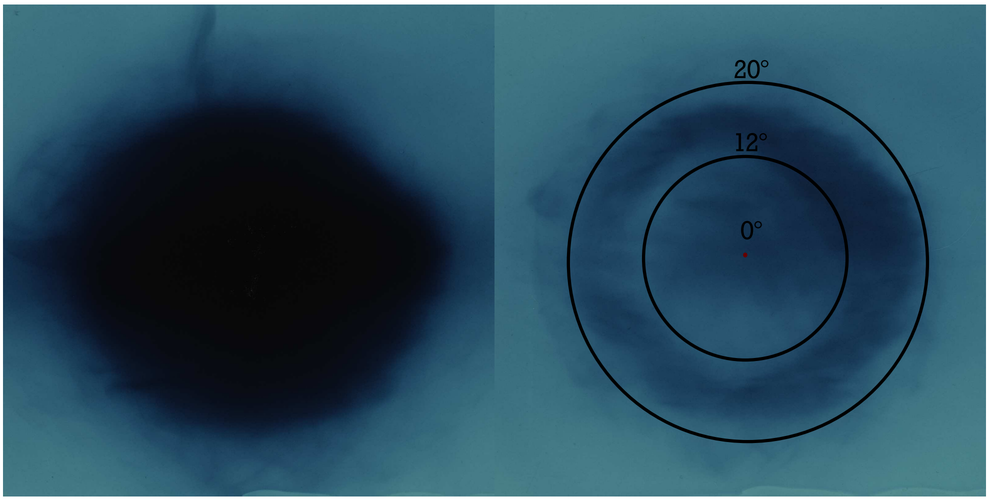

Figure 3.14: Two RCFs at 40 mm distance to target record the transversal profile of the laser-driven heavy ion beam. The left RCF of type EBT3 with only one layer of substrate detects carbon ions with kinetic energies above 6.5 MeV, whereas the right one is only sensitive to carbon ions with kinetic energies exceeding 77 MeV. For these high energies the ring structure is well pronounced, but not perfectly symmetric in its intensity distribution.

three TPs at different angles, which also showed ions at high energies in the center of the beam. The fact that there is a significant signal on the second RCF signifies the acceleration of C^{4+} ions to kinetic energies exceeding 77 MeV. Compared to a typical shot from the experimental campaign in February 2017, here shot 20, the minimum cut-off energy of the C^{4+} ion spectrum from shot 70 in the campaign in February is at least 10 MeV higher. All other parameters like target preparation, focal spot size etc. were similar for the two shots, but a refurbishing of the dielectric parabolic mirror, which focusses the short pulse laser onto the target, increased the intensity in the focal spot significantly, which led to the increase in kinetic energy.

These rings were not commonly observed in the experiments with a heated target by M. Hegelich et al. [16, 87, 99]. The only mention of a ring-structure in their work is in conjunction with a damaged target that had a small hole burned through during the alignment process [88]. In all of the presented experimental data, special care was taken to prevent such incidents and the targets were checked directly before each shot. Literature research discovered several articles, that touch on observed ring structures and possible explanations of this phenomenon, but all of them for laser-driven proton beams.

The first mention of rings in the transversal beam profile of laser-driven proton beams was as early as 2000 in the pioneering work by E.L. Clark et al. [132]. They used a stack detector consisting of one RCF followed by multiple CR39 plates. The resulting beam profile exhibited a bell-shaped intensity profile in the RCF and rings for the subsequent CR39 plates with decreasing diameter for increasing kinetic energies of the protons. The authors suggested that protons getting accelerated at the front surface and propagating through the target are deflected by magnetic fields inside the target. This explanation was first confirmed by PIC simulations from A. Pukhov [84], before experiments by M. Allen et al. proved that ions accelerated in the TNSA scheme stem only from the observed surface [72] and there is no contribution from ions propagating from the front side through the target.

After reproducing the findings of E.L. Clark with a similar combined detector of CR39 plates, Y. Murakami et al. concluded in 2001 that magnetic fields in the order of 10^4 T acting on the beam over several μm have to exist on the rear surface of the target to explain this phenomenon [133]. In a direct response to the earlier article by E.L. Clark et al. [132], S. Gaillard et al. published a comment [134] and an article [135] on how the observed rings in the CR39 plates arise from the over-saturated nuclear track detectors. As the proton spectrum decreases exponentially towards higher energies and due to the quadratic decrease of proton numbers for increasing divergence, the center parts of the CR39 plates are highly over-saturated. The etched tracks overlay each other in this area and when utilizing a density measurement of the tracks by means of optical reflectivity the over-saturated areas seem to show a lower proton density.

Recent research by H. Padda et al. in 2016 investigated the interaction of high intensity high energy laser pulses exceeding intensities of $2 \times 10^{20}\,\mathrm{W\,cm^{-2}}$ with $0.01\,\mu$m to $0.4\,\mu$m thin aluminium foil targets at the VULCAN laser facility [136]. They also measured annular proton beam profiles for low kinetic energies, which smear out for higher kinetic energies, but they inferred that this behaviour might be caused by transitions between acceleration mechanisms. Early in the Gaussian laser pulse the protons are accelerated via TNSA, but with increasing laser intensities radiation induced transparency [29, 31, 32] sets in. The aluminium ions, accelerated out of the bulk of the target via RIT, start to catch up with the slow protons and push them outwards because of Coulomb repulsion.

Another group of scientists observed ring-like structures in transversal proton beam profiles without any RIT. In an article from 2018 G. Becker et al. describe ring-like structures with opening angles of 11° to 13°, that smear out close to the cutoff energy [137]. They used a frequency doubled POLARIS laser system at 515 nm with intensities of $9 \times 10^{19}\,\mathrm{W\,cm^{-2}}$ in combination with 0.1 μm to 0.8 μm thin polyethylene foils and detected the transversal energy resolved beam profile with gated CCD-cameras and fast plastic scintillators. They could prove that no laser light was transmitted and therefore no RIT took place. Reproducing the experimental observations with 2D-PIC simulations led them to the conclusion that a lateral charge separation close to the 0° axis gives rise to a lateral electric field, which in turn pushes protons away from the axis. As the lateral electric field decreases further away from the 0° axis, a common deflection angle dependent on the proton energy emerges. This effect declines with increasing target thickness, because the maximum electric field is less localized due to increased multiple small angle scattering of the hot electrons inside the target.

Just this year M. Nakatsutsumi et al. [138] reported about the formation of strong self-generated surface magnetic fields for laser intensities exceeding $10^{20}\,\mathrm{W\,cm^{-2}}$ that distort the proton distribution, evident from PIC simulations, and prevent the acceleration of high energy protons.

The findings of the investigations of the transversal beam profile of laser-driven heavy ion beams in this work are best represented by the research of G. Becker et al. [137]. The relativistic parameter a_0 is of the same order of magnitude for both experiments, but the target thickness is bigger by at least a factor of 10 in the heavy ion acceleration experiment. Judging from the trend of the opening angle of the annular structure versus target thickness, there should be no rings visible in the presented experiment. However, 2D-PIC simulations carried out by M. Afshari[3] in the plasma physics group at GSI show similar rings for CH-targets in the range of 5 μm to 10 μm target thickness. Thus with further simulation studies a suitable description for the case of laser-driven heavy ion beams should be found. What remains puzzling is the high intensity of Carbon ions at low energies on the beam axis.

To fully understand the observed ring-like structures further experiments are necessary. In the following chapters, especially for the input of the laser-driven heavy ion beam into accelerator physics simulations, the laser-driven heavy ion beam is assumed to behave like a proton beam, characterized in references [46, 108, 113]. The divergence distribution is taken from the references in terms of $E_{kin}/E_{kin,max}$. This assumption is especially valid for low energies, e.g. in the case of C^{4+} ions for kinetic energies up to 20 MeV, because the measured spectra at −12° and 20° match the expected spectra for proton like behaviour well (compare figure 3.12).

---

[3] M. Afshari et al., unpublished results and private communication

4 Transport and energy selection of laser-driven heavy ion beams

Almost immediately after the discovery of the compact acceleration of ion bunches by ultra-intense laser irradiation of solid targets almost two decades ago [14, 15, 17] numerous possible applications for these ion beams were suggested. They ranged from igniting inertial confinement fusion [18, 19], driving isochoric heating to achieve warm dense matter [20, 21, 22] to the generation of isotopes with table-top devices [23] and particle therapy [24, 25]. Due to the high particle numbers and initially short pulse durations of the ion bunches the monitoring of transient phenomena is an interesting field of work and has been pursued as proton radiography [26, 139, 140, 141]. Lately the generation of laser-driven neutron beams has been investigated by several groups [27] and neutron resonance spectroscopy was successfully demonstrated recently [142]. With proton radiography time resolved measurements in the picosecond range are possible, but a major drawback is the required very short distance of some millimeters between proton source and object of interest to have sufficient beam intensities intensities available. On the one hand this leads to a very high background level for any diagnostics and on the other hand the x-rays, EMP and hot electrons from the laser-plasma interaction could influence the object of study. To enable the application of laser-driven ion beams as particle probes for the measurement of the stopping power of hot and dense plasmas (as introduced in section 1.1), a spatial separation of the source of the probe beam and the examined plasma has to be ensured. Thus the ion beam has to be collimated shortly after its generation and only a relatively narrow part of the energy spectrum suitable for the probing should be transported. These conditions also have to be fulfilled, if particle therapy or injection in further accelerating structures are strived for.

The following section is dedicated to the study of feasibility of transport and energy selection of laser-driven heavy ion beams. After a short excursus about the beam dynamics and emittance of ion beams, different methods for the collimation and energy selection are reviewed. Simulation studies with the linear accelerator simulations tool TraceWin pave the way to the experimental realization of the transport and energy selection section of LIGHT. The characterization of the resulting heavy ion beams together with a comparison with the simulated output of the beamline, followed by a discussion of the results, will conclude the chapter.

4.1 Terminology of accelerator physics

For a better understanding of later paragraphs, it is mandatory to briefly introduce the basic terminology and mechanics of accelerator physics. The general approach to the dynamics of single particles in accelerators are covered in the next section, whereas paragraph 4.1.2 touches on the defining characteristic of the quality of ion beams, the emittance. The description of beam dynamics and emittance are mainly taken from references [143, 144, 145, 146].

4.1.1 Linear beam dynamics

As with many problems in physics and mathematics, an intelligent way of redefining the reference system can simplify the problem significantly. In accelerator physics this simplification is achieved by introducing a co-moving coordinate system, whose coordinate origin is always at the position of the reference particle. The coordinate system is defined by the unit vector in direction of the trajectory of the reference particle $\mathbf{u}_s$ and two unit vectors $\mathbf{u}_x, \mathbf{u}_y$ perpendicular on $\mathbf{u}_s$ in a mathematically positive direction of rotation, when looking in the direction of travel. With this coordinate system and the parameter s being the distance travelled along the trajectory of the reference particle (also called synchronous particle) $\mathbf{r}_0(s)$, measured from an arbitrary point, any point in space is described by

$$\mathbf{r}(s) = \mathbf{r}_0(s) + x \cdot \mathbf{u}_x + y \cdot \mathbf{u}_y. \tag{4.1}$$

This method is only applicable, if the reference trajectory is known, which is almost always the case when designing a particle accelerator. Figure 4.1 shows the evolution of the co-moving reference system along a reference trajectory. It should be noted at this point, that the coordinate system (x, y, s) is curvilinear, which results in the line element being

$$\mathrm{d}\mathbf{r} = \mathbf{u}_x \mathrm{d}x + \mathbf{u}_y \mathrm{d}y + \mathbf{u}_s \cdot (1 + hx)\mathrm{d}s, \tag{4.2}$$

where $h = 1/\rho_0$ denotes the curvature of the reference trajectory, ρ_0 being its radius. Thus, it can be helpful to introduce a right-handed coordinate system with $\mathbf{u}_z$ parallel to $\mathbf{u}_s$.

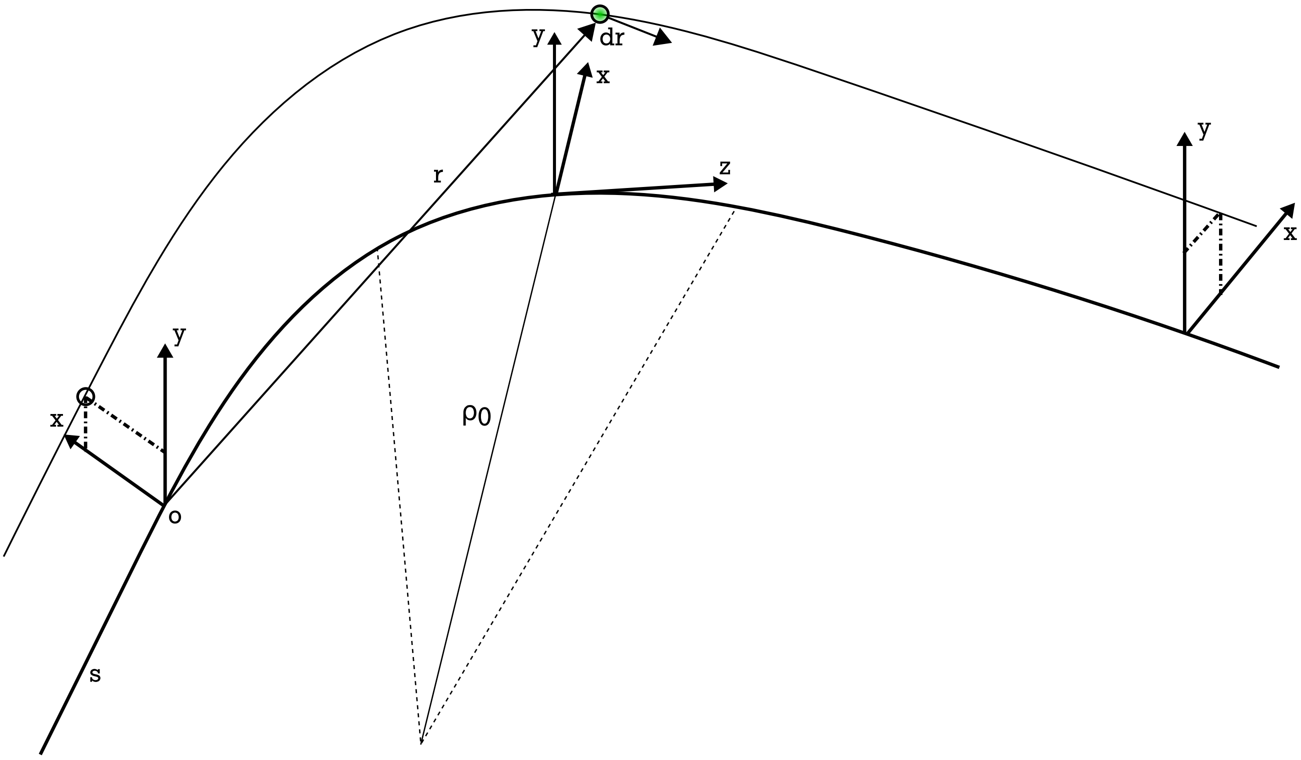

Figure 4.1: Sketch of the co-moving coordinate system in accelerator physics (comparable to [143]). The actual reference frame, (**x**,**y**,**s**), is a curvilinear coordinate system. It can be convenient to define a right-handed coordinate system, (**x**,**y**,**z**), with **z**(s) pointing in the direction of the tangent on **s**.

The complete description of a single particle in accelerator physics is achieved with a six-dimensional reference system, also called phase space. In addition to the two spatial coordinates (x, y) for the transversal position, two coordinates (x', y') represent the direction of travel with respect to the reference trajectory (divergence) and implicitly the transversal momentum of the particles

$$x' = \frac{\mathrm{d}x}{\mathrm{d}s} = \frac{p_x}{p_z} \approx \frac{p_x}{p_0}; \quad \frac{p_x}{p_z} = \tan(\theta_x) \approx \theta_x; \quad y' = \frac{\mathrm{d}y}{\mathrm{d}s}. \tag{4.3}$$

Setting $p_z \approx p_0$ and $\tan(\theta_x) \approx \theta_x$ is called the paraxial approximation, which is only viable as long as (x, y) are small compared to the curvature of the trajectory and $(x', y' \ll 1)$. The 5th and 6th dimensions of the six-dimensional reference system are the longitudinal characteristics of the particle and read as

$$l = -v_0(t - t_0); \quad \delta = \frac{p - p_0}{p}. \tag{4.4}$$

As the velocity of particles in accelerators for the most part exceeds several percent of the vacuum speed of light, the transversal manipulation of particle beams is dominated by the magnetic part of the Lorentz force (for readily available quasi-static EM-fields). The paraxial approximation enables a Taylor series expansion of an arbitrary magnetic field

$$\frac{q}{p}B_y(x) = \underbrace{\frac{q}{p}B_{y0}}_{dipole} + \underbrace{\frac{q}{p}\frac{\mathrm{d}B_y}{\mathrm{d}x}x}_{quadrupole} + \underbrace{\frac{q}{2p}\frac{\mathrm{d}^2B_y}{\mathrm{d}x^2}x^2}_{sextupole}. \tag{4.5}$$

In order to analytically solve the resulting equations of motion, it is necessary to neglect all higher orders beyond quadrupoles, thus limiting the beam dynamics to the linear approximation. In experimental realities this supposition is supported by the use of extremely high quality magnets, which are designed specifically to suppress any higher order fields. Dipole magnets are used for beam guiding purposes, whereas quadrupole magnets focus the beam transversally. The linear approximation also allows for a separate treatment of the x- and y-plane, because they stay linearly independent under all possible operations. This only holds true for paraxial beams, because any change in transverse momentum cannot effect the total momentum of the particles. Under these conditions beam transport can be expressed as simple matrix operations with a 6×6-dimensional transfer matrix $R(s)$.

$$\mathbf{r}(s) = R(s)\mathbf{r}(s = 0) \tag{4.6}$$

4.1.2 Emittance and quality of ion beams

As the beam consists of an ensemble of particles, a description in terms of density in the phase space is needed. The beam is fully characterized, when its density distribution $\rho(\mathbf{r})$ is known at any combination of the 6-dimensional coordinates. In many cases 2-dimensional projections of this volume filling object are considered, in this case a projection to the (x, x')-plane.

Generally these density distributions have the shapes of ellipses. Any ellipse can be expressed as a symmetrical 2×2-matrix-form

$$\mathbf{X}^T\sigma_x^{-1}\mathbf{X}=1;\quad \sigma_x=\begin{pmatrix}\sigma_{11} & \sigma_{12}\\ \sigma_{12} & \sigma_{22}\end{pmatrix} \tag{4.7}$$

where **X** denotes the vector (x,x') to the border of the ellipse. The area inside of the ellipse is defined as $A=\pi ab$, a,b being major and minor axis of the ellipse. The matrix-form of an ellipse in equation 4.7 represents a tilted ellipse with the area

$$A=\pi\sqrt{\det\sigma_x}=\pi\sqrt{\sigma_{11}\sigma_{22}-\sigma_{12}^2}\doteq\pi\epsilon_{xx'}. \tag{4.8}$$

The emittance, projected to the (x,x')-plane, is therefore the area of the phase-space ellipse, or in the 6-dimensional phase-space, an ellipsoid with as many dimensions. Generally speaking the emittance represents all characteristics of the ion beam. In the two dimensional projection useful variables can be identified, such as the maximum extent of the phase space ellipse

$$x_{max}=\sqrt{\sigma_{11}};\quad x'_{max}=\sqrt{\sigma_{22}}, \tag{4.9}$$

also depicted in figure 4.2. The correlation of the spatial extent of the beam and its divergence can also be described with the dimensionless correlation parameter

$$r_{12}=\frac{\sigma_{12}}{\sqrt{\sigma_{11}\sigma_{22}}};\quad x_{cor}=r_{12}\sqrt{\sigma_{11}};\quad x'_{cor}=r_{12}\sqrt{\sigma_{22}}. \tag{4.10}$$

It should be noted, that perfect correlation $|r|_{12}=1$ leads to the emittance being zero. In real machines however, the emittance can never be zero, not even at the source of the ions. This can be understood, when thinking about the source as an ion-emitting area, where the preferential direction of emission is combined with an element of randomness caused by the non-zero temperature of the emitter. The bigger the randomness (temperature) of the emitter, the less correlated and thus more turbulent the resulting ion beam. The correlation parameter can also be used as a measure for the collective behaviour of the beam. A positive correlation signifies a diverging ion beam and a negative correlation a converging ion beam. x_{cor} or x'_{cor} define the maximum extent in x and x' only at a beam waist or for a parallel beam respectively. As real ion beams cannot be assumed as homogeneous density distributions with sharp borders, but with arbitrary density distributions $\sigma(\mathbf{r})$ depending on the phase space coordinates, it is important to include the quantile which is actually covered by the emittance. For most cases it is sufficient to assume a Gaussian density distribution. In two dimensions it can be written as

$$\rho(\mathbf{X})=\frac{1}{2\pi\epsilon_{xx'}}\exp\left(-\frac{1}{2}\mathbf{X}^T\sigma_x^{-1}\mathbf{X}\right). \tag{4.11}$$

The area enclosed by this ellipse equals an emittance of a one standard deviation quantile of the beam (1-σ). The usual measure for the emittance for ion accelerators is the 2-σ emittance, including 86.5 % of all ions in the beam. It is four times the 1-σ emittance.

$$\epsilon_{xx'}^{2\sigma}=4\cdot\epsilon_{xx'}^{1\sigma}=4\sqrt{\sigma_{11}\sigma_{22}-\sigma_{12}^2} \tag{4.12}$$

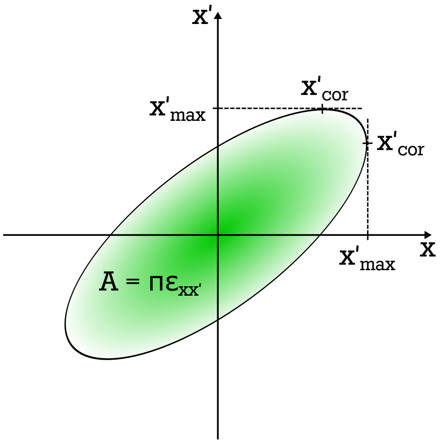

Figure 4.2: As long as the linear approximation holds true, all particles move along ellipses through the phase space. Thus any ensemble of particles can be encapsulated in an ellipse/ellipsoid. The area/volume is a measure of the correlation of each phase space coordinate to any other phase space coordinate.

According to the theorem of Liouville, the phase-space-volume stays constant under the influence of conservative forces (absence of collisions). Therefore it should remain the same over the whole accelerator. At the first glance, the theorem seems to be violated for ion beams that are accelerated, because all phase space coordinates are defined with respect to the reference particle. However, when introducing the acceleration adjusted emittance $\epsilon_{acc} = \beta\gamma\epsilon$, γ being the Lorentz factor and $\beta = v/c$, the theorem holds true.

The conservation of the area of the bounding ellipse, which is in two dimensions associated with the emittance in this sub-phase-space, is only warranted under the influence of linear forces. Non-linear forces cause a filamentation of the phase space. Thus, under the assumption of a finite resolution when measuring the emittance, and the difficulties of reversing this filamentation (achievable for example with beam cooling), the emittance is indeed growing. Progressive filamentation can also lead to instabilities, which destroy the regularity in the filaments. A typical non-linear phenomenon is the influence of the inherent space charge of the ion beam (multi-stream instability).

4.1.3 Space charge

A typical ion beam in an accelerator with a very good vacuum is not space charge compensated, meaning its net charge is positive. The following paragraph is based on references [143, 147, 148]. Assuming a coasting beam (not-bunched) with a uniform cylindrical ion density and radius r, the ions experience a repulsive force from the Coulomb interaction, which increases for the outer ions. A magnetic field, produced by the current of the beam, counteracts this repulsion.

$$\delta \mathbf{F}_r = \frac{q^2\rho}{2\epsilon_0}(1-\beta^2)r \tag{4.13}$$

The area density ρ is uniform and $\beta = v/c$. Effective reduction of the Coulomb repulsion only happens for relativistic beams and thus plays only a minor role for laser-driven ion beams.

Electrons, stemming for example from ionized rest gas, can compensate the space charge. The factor f_e, ranging from 0 to 1, represents that.

$$\delta \mathbf{F}_r = \frac{q^2\rho}{2\epsilon_0}(1-\beta^2-f_e)r = \frac{q^2\rho}{2\epsilon_0\gamma^2}(1-\gamma^2 f_e)r \tag{4.14}$$

TNSA-generated ion beams are very special with regard to space charge. The ions stem from a source size as small as $50\,\mu$m to $100\,\mu$m diameter and are generated in a time frame of picoseconds. Without any space charge compensation the ions would be pushed out of this source region in a 4π solid angle. This phenomenon has been observed for mass limited targets, where a large part of the electrons were pushed out of the target by the laser and the target then exploded because of the Coulomb repulsion. In the case of the TNSA-mechanism however, the accelerated ions attract electrons from the electron sheath and accelerate them because of their positive potential. As electrons have a vastly superior charge-to-mass ratio, these co-moving electrons exhibit the same velocity distribution as the ions and ensure a fully space charge compensated beam. Guiding the mixed beam with ion optical elements distorts this compensation. Accounting for the very complicated interaction between space charge and magnetic fields of the ion optics is touched on in section 4.3.

4.2 Review of beam transport devices

Transporting TNSA-generated heavy ions equals manipulating their transversal phase-space in a way, that collimates the highly divergent ion bunch while preserving the emittance. As the TNSA-ions exhibit a very broad energy spectrum, it is also desirable to limit the collimated beam to a smaller part of the spectrum. Ion optical lenses possess an inherent chromaticity, similar to optical lenses, which takes care of the energy selection by itself. By adding a pinhole to the beamline, or just because of the limited acceptance of the beamline, the spectrum of the propagating particles consists to a growing extent solely of ions that were collimated. Collimating the whole TNSA-ion bunch is in principle possible, if the focussing force of an ion optical lens directly behind the ion source is ramped down fast enough to take advantage of the very high level of order in the longitudinal structure of the TNSA ion bunch (very small longitudinal emittance). So far no such device is readily available and for many applications, such as injection into an accelerator, a broad energy spectrum cannot be utilized anyway.

In the following section different ion optical focussing systems are covered. Combinations of quadrupole magnets are the most commonly employed ion lensing systems, but solenoid magnets are also frequently used and have certain advantages when compared to quadrupole magnets. The section is completed by a short discussion of the advantages and drawbacks of each method in order to come to a decision about which method is best suited for the task.

4.2.1 Quadrupole magnets

Quadrupole magnets are capable of influencing the transversal phase space of ion beams, while still being covered by the linear beam dynamics. That makes them the ideal tool to restrain the beam to the confinements of the beam tube. A quadrupole consists of four poles in a regular configuration (every $\pi/2$), also displayed in figure 4.3. Positively charged ions, travelling into the plane of display, experience a deflecting force proportional to the distance of the ions to the center of the quadrupole. It is due to this circumstance that quadrupoles serve as lenses for charged particles. A single quadrupole however, focusses only in one plane, here the x-z-plane, whereas it defocusses in the perpendicular plane, the y-z-plane. The field in an ideal quadrupole can be described as the gradient of a scalar field $\Phi(x, y)$, if the fringe fields are neglected, because of the much smaller transversal extent compared to the longitudinal extent.

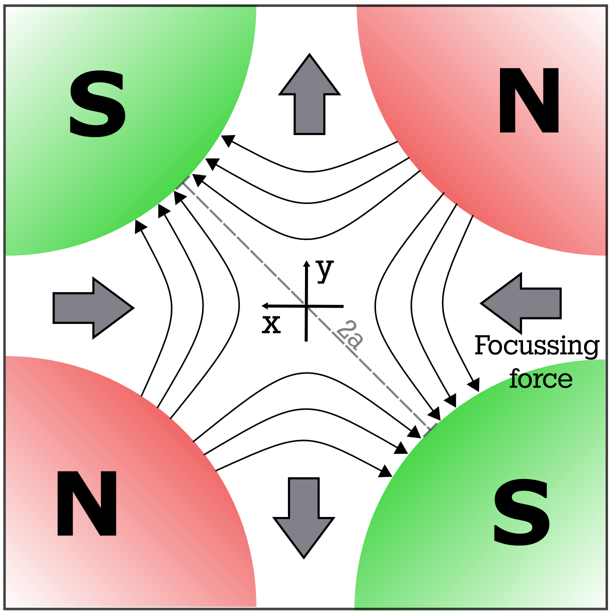

Figure 4.3: A quadrupole consists of four poles, arranged so that poles with the same polarity face each other. The field lines and the resulting force on a positively charged ion travelling into the drawing plane are also displayed.

$$\mathbf{B} = -\nabla\Phi; \quad \Phi(x, y) = -gxy; \quad g = \frac{\partial B_y}{\partial x} = \frac{\partial B_x}{\partial y} = \frac{B_0}{a}. \tag{4.15}$$

The gradient of the magnetic field g equals the ratio of the magnetic field at the poles B_0 and half the distance between two opposite poles a. Quadrupoles are typically driven by current-carrying coils, either pulsed or in continuous operation, mostly because successful manipulation of the beams requires adjustment. Nevertheless there are also permanent magnet quadrupoles, built as *Halbach-arrays* [149].

Provided that the paraxial approximation holds true, the focal length of a quadrupole is

$$|f| = \frac{1}{kL}; \quad k = \frac{g|q|}{p}, \tag{4.16}$$

where q denotes the charge of the ion, p its momentum and L the length of the quadrupole. The focal length is the same for focussing or defocussing. To obtain a focussing effect for both planes, x-z- and y-z-plane, at least one additional quadrupole magnet is necessary, rotated by $\pi/2$ around its z-axis. In that way each plane experiences one focussing and one defocussing force. The overall focussing is owed to the dependence of deflection on the distance to the main axis and is demonstrated in figure 4.4. The focal length of a quadrupole doublet can be written as

$$\frac{1}{f_d} = \left(\frac{qB_0}{ap}\right)^2 \cdot L^2 \cdot s. \tag{4.17}$$

Increasing the separation s between the quadrupoles (center to center) decreases the focal length of the doublet, but also decreases the acceptance angle and therefore the number of transported particles. As the acceptance angle differs for the two transversal directions, x and y, any axial symmetry the beam profile might possess is lost after the quadrupole doublet.

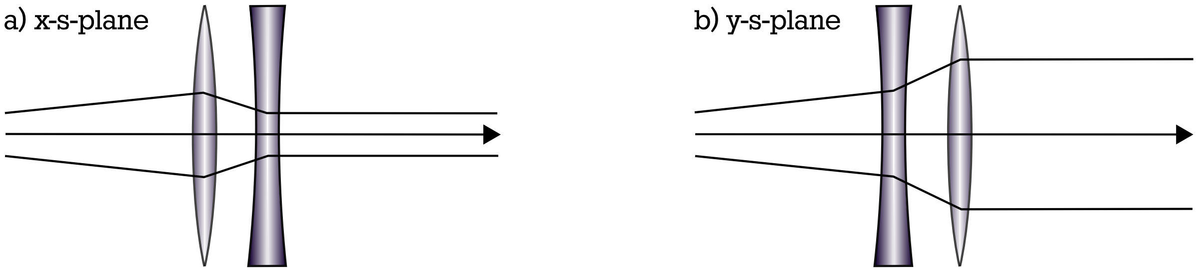

Figure 4.4: A combination of two quadrupoles, that are rotated against each other by $\pi/2$ with respect to the beam axis, applies an overall focussing force on charged particle beams. Any given charged particle experiences a defocusing in one of the quadrupoles, but the dependence of the magnetic field strength on the distance to the beam axis ensures a focussing effect.

4.2.2 Solenoids

Solenoids are another possible device for the transversal focusing of charged particles in accelerators. They are frequently used in the low energy beam transport section of an accelerator, before injection into the first accelerating structure after the source (typically a radio frequency quadrupole). Solenoids are usually wire-wound electromagnets of cylindrical shape, operated either in continuous or pulsed operation. By exploiting the axial symmetry of the solenoid, the magnetic field can be reduced to a radial and an axial part. In case of a static magnetic field, the magnetic field becomes $\mathbf{B} = -\nabla\Psi(r,z)$. A series expansion of $\Psi(r,z)$, demonstrated for example in [150] or [47], enables the description of the magnetic field as

$$B_z(r,z) = B(z) - \frac{r^2}{4}\frac{\mathrm{d}^2B(z)}{\mathrm{d}z^2} + \ldots \tag{4.18}$$

$$B_r(r,z) = -\frac{r}{2}\frac{\mathrm{d}B(z)}{\mathrm{d}z} + \frac{r^3}{16}\frac{\mathrm{d}^3B(z)}{\mathrm{d}z^3} - \ldots \tag{4.19}$$

This expression can be further simplified, if the paraxial approximation is applicable. Then it suffices to keep only terms up to linear dependence on r. If on top of that the coordinate system is chosen in a way, that the origin is situated in the center of the entrance of the solenoid with length L and z-axis being anti-parallel to the direction of the symmetry axis of the solenoid, then the field can be expressed as

$$B_z = -B_0[\Theta(z) - \Theta(z-L)]; \tag{4.20}$$

$$B_r = B_0\frac{r}{2}[\delta(z) - \delta(z-L)]. \tag{4.21}$$

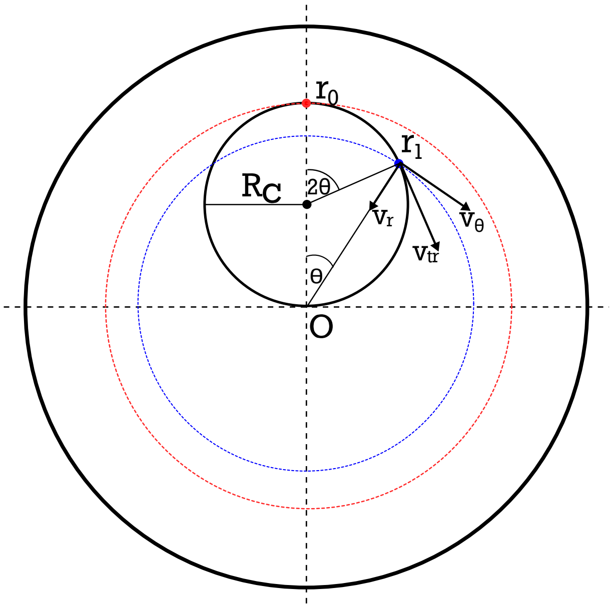

Figure 4.5: Schematic drawing of solenoid focussing: Any ions entering the solenoid receive a change in transversal velocity due to the radial magnetic field component in the fringe field and start gyrating. The transversal velocity stays constant inside the solenoid, but the decomposed azimuthal and radial components change. The azimuthal component is cancelled upon traversing the fringe field a second time, whereas the radial component stays constant.

Θ denotes the Heaviside function and δ the Kronecker delta. This approximation as well as the ensuing derivation of the focussing characteristics can be found in [151].
For the sake of simplicity, only ions with charge $q = e$ and axial velocity v_z (no radial velocity) are considered. Ions traversing the fringe field at distance r_0 to the symmetry axis experience a kick in azimuthal direction, resulting in a velocity component

$$v_\theta = r_0 \frac{eB_0}{2\gamma m} = r_0 \omega_L \tag{4.22}$$

in azimuthal direction. Inside the solenoid, the ions start rotating around $\mathbf{r}_0/2$ with the Larmor frequency ω_L, displayed in figure 4.5. In this case, with the paraxial approximation still holding, the longitudinal velocity v_z does not change and as there are no radial magnetic fields inside the solenoid, nor does the transversal velocity v_{tr}. With the radial position being described by

$$r = r_0 \cdot \cos\left(\frac{\omega_L z}{v_z}\right) \tag{4.23}$$

it is possible to decompose the transversal velocity into a radial and an azimuthal part.

$$v_\theta = \omega_L \cdot r \tag{4.24}$$

$$v_r = -\sqrt{v_{tr}^2 - v_\theta^2} = -\omega_L \cdot r_0 \cdot \sin\left(\frac{\omega_L z}{v_z}\right) = -\omega_L \cdot r \cdot \tan\left(\frac{\omega_L z}{v_z}\right) \tag{4.25}$$

Upon leaving the solenoid and thus traversing the fringe field at the exit, which points in the opposite direction as the fringe field at the entrance, the ions receive a kick in the negative azimuthal direction. The strength of the kick depends on the radial position r_1 at the exit of the solenoid.

$$\Delta v_\theta = e v_z B_r(z) = -r_1 \frac{eB_0}{2\gamma m} = -r_1 \cdot \omega_L \tag{4.26}$$

Therefore the azimuthal velocity is cancelled out once the ions reach the field free space, but the radial velocity from position $(r,z) = (r_1, L)$ remains unchanged. This behaviour is independent of the starting position of the ions, at least as long as intra-beam interactions are neglected (space charge effects). In case of a thin lens approximation, employable for $L \ll v_z/\omega_L$, the radial distance r_0 stays approximately the same over the whole solenoid. Combined with the small angle approximation for the tangens, equation 4.25 at the exit of the solenoid can be simplified to

$$v_r = -\frac{r_0 e^2}{4\gamma^2 m^2 v_z} B_0^2 L. \tag{4.27}$$

As $\mathrm{d}r/\mathrm{d}z$ depends linearly on r, within the paraxial approximation a focal length f_s for the solenoid can be defined for any charged particle with mass m and charge q.

$$\frac{1}{f_s} = \frac{q^2}{4m^2\gamma^2 v_z^2} \int B^2 \mathrm{d}z \tag{4.28}$$

4.2.3 Comparison of transversal focussing devices

Having covered the two most common transversal focusing devices, quadrupoles and solenoids, still the question remains, which device is better suited for the collimation and energy selection of TNSA-generated ions. One criterion is the possibility to generate the necessary magnetic field. The focal length of a quadrupole doublet from equation 4.21 can be set into relation with the focal length of a solenoid lens to compare focussing strengths for equal magnetic fields.

$$T_d = \frac{1/f_d}{1/f_s} = \frac{4sL_d^2}{a^2 L_s} \tag{4.29}$$

L_d denotes the length of the quadrupoles and L_s the length of the solenoid. To achieve comparable acceptance angles the overall lengths of the two ion-optical devices are both set to L. Assuming a separation s of the magnets of $2L_d$, equation 4.29 can be written as

$$T_d = \left(\frac{2}{3}\right)^3 \left(\frac{L}{a}\right)^2. \tag{4.30}$$

Thus for a small aperture a the focusing strength of a quadrupole doublet exceeds the focussing strength of a solenoid. From this finding I. Hofmann deduced, that quadrupole doublets or even triplets are better suited for the task, see reference [152], especially for ion beams generated by RPA. In the LIGHT project however, solenoids were taken, mainly because of the readily available big apertures. The huge opening angles of the TNSA-generated ion beams require large acceptance angles. Although it is true that the magnetic fields have to be substantially bigger for solenoid lenses, employing pulsed solenoids with quasi-constant fields over several μs, remedies this problem. On top of that collimation with quadrupole doublets causes increased losses due to the defocussing in one transversal plane of the already highly divergent ion beam in the first quadrupole and an overall loss of the axial symmetry of the transversal beam profile.

4.3 Beam dynamic simulations

Ever since the steep rise in computational power from the 1970s onwards, the successful design and operation of accelerators included the simulation of beam dynamics. The comparably small setup of the LIGHT beamline could be calculated by hand, if a lot of approximations, such as paraxiality, ideal solenoids as thin lenses, negligible space charge etc. were made. These approximations however, make for very poor representations of experimental realities, thus emphasizing the need for simulations.

This section is comprised of a paragraph about the different approaches to simulations followed by a description of the setup of the simulation study of the transport capabilities of the LIGHT beamline in the case of laser-driven heavy ion beams and its results. Most of the simulations were published previously in [153].

4.3.1 Selection of simulation software

The optimal choice of the characteristics of a simulation and a fitting software package is closely linked to the physical phenomenona, which define the examined process. In the case of the beam dynamics of a TNSA-generated ion beam, this includes a wide range of phenomenona, such as space charge effects, chromaticity, imperfections of ion optical elements and all of them acting on a bunched beam, occupying an initial volume of some $100\,\mu\mathrm{m}^3$ and diverging quickly. On top of that, the ion beam is initially best described as a directed plasma expansion, resulting in a complete space charge compensation. Simulation codes, capable of an accurate representation of the interaction of the ion beam with the co-moving electrons, are particle in cell codes, which calculate fields from the density distribution of macroparticles in a grid of simulation cells at every time step and then evaluate the trajectories of the macroparticles in these fields. The process is then repeated with a new density distribution at the next time step. PIC codes are in general very CPU-intensive, since the cells and time steps need to be small enough to resolve the beam evolution. For the simulation of beam dynamics on the picosecond-scale and over several meters, these codes are not applicable without modifications.

PIC simulations of TNSA-generated proton beams with stepwise adjusting of time steps and cell sizes have been performed by F. Nürnberg [112, 154] with the Warp code [155] in 2010 and by A. Almomani [156, 157] with the LASIN code, a self-developed PIC code. In both cases the six dimensional phase space of the proton beam some micrometers behind the target was taken as the input of the simulation. Then by adjusting the time steps and cell sizes in three stages for the LASIN simulations from $4\,\mu\mathrm{m}$ to 1 mm and 25 fs to 25 ps the interaction of protons with the co-moving electrons and the external magnetic solenoid field could be simulated with sufficient precision. The preceding work of F. Nürnberg with the Warp code incorporated only two stages and a coarser mesh. The findings of both simulation studies were very similar and suggested that a good part of the co-moving electrons are transmitted through the solenoid. These electrons are confined to a very small radius around the solenoid axis, because of their charge-to-mass ratio (see left diagram in figure 4.6). The result is a negative potential, which attracts protons and therefore influences the characteristics of the transported proton beam. The accumulation of protons of all energies onto the beam axis can be also seen in the right diagram in figure 4.6.

However, the number of transmitted electrons greatly depends on the magnetic mirror effect [55] and thus on the value of the fringe field at the position of the TNSA source. For charged

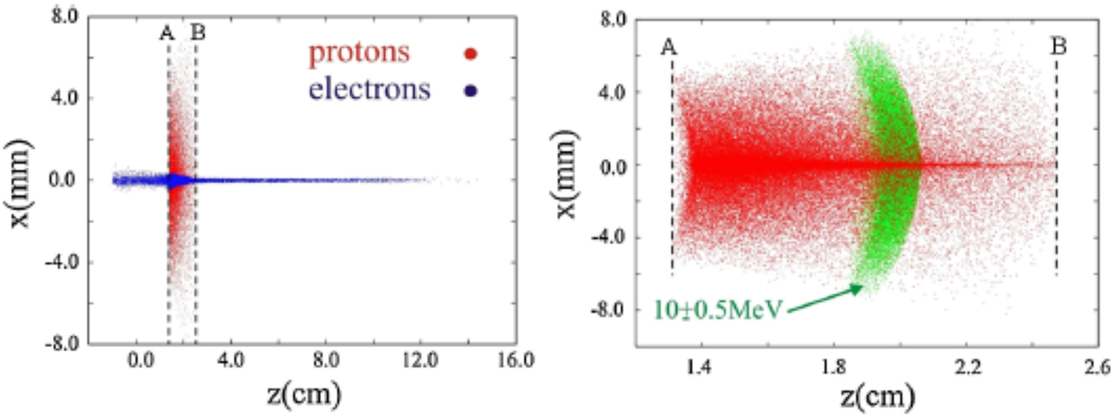

Figure 4.6: The initially comoving electrons are focussed onto the beam propagation axis by the fringe field of the solenoid. The resulting negative potential pushes electrons longitudinally in both directions, visible in the long tails exceeding the extent of the proton beam. The influence on the proton beam can be seen from an accumulation of protons on the propagation axis for all energies. Figure taken from [157]

.

particles not to be reflected by the magnetic fringe field, they have to fulfil the following conditions.

$$\frac{v_{trans}}{v_{ges}} < \frac{1}{\sqrt{\frac{B_{max}}{B_{source}}}} \quad \text{for} \quad \frac{m v_{trans}}{|q|B} \frac{\nabla B \cdot \mathbf{e}_{long}}{B} \ll 1 \tag{4.31}$$

v_{trans} denotes the transversal and v_{ges} the total velocity of the particle and $\mathbf{e}_{long}$ the direction of ion propagation. B_{max} and B_{source} indicate maximum magnetic field and magnetic field at the position of creation of the charged particle. The ions are not reflected by the fringe fields of the solenoid, because their huge mass leads to a violation of the adiabatic change of the magnetic field over the gyration revolution of the ion. For electrons the change of the magnetic field along their trajectory can be approximated as an adiabatic process, in which the magnetic moment stays constant. Then only electrons fulfilling equation 4.31 are transmitted (neglecting space charge effects). The simulation study by A. Almomani assumed the source to be deep in the fringe field, at roughly 30 % of the maximum field, whereas the study carried out by F. Nürnberg put the solenoid much further away and consequently reduced the magnetic field at the source B_{source} to 1.4 %. The accumulation of protons on the beam propagation axis in the Warp simulations was not as pronounced as in the LASIN simulations, mainly because a lot fewer electrons actually contributed to the negative space charge potential inside the solenoid. The interaction between electrons and protons is more sophisticated than just calculating the ratio of electrons inside the loss cone of the magnetic mirror effect and their influence on the proton beam. However, the influence of the magnetic mirror effect is quite big.

The simulation studies in the present work were carried out with a particle tracking software package called *TraceWin* [158], mainly because of the overall reduced computation time, large number of available modules, that can be combined very easily, and the included support, that comes from buying the license. TraceWin is primarily used for linear accelerator design and has features, which make the code suitable for simulating the transport of laser-accelerated ions. The code is a self-consistent 3D particle-in-cell code, which is capable of tracking up to

4×10^8 simulation particles. It is possible to transport two different beams in the same structure, but TraceWin neglects any interactions between the two. Therefore a suitable space charge compensation factor is needed to include space charge for TNSA ion beams. TraceWin can incorporate fieldmaps into the beamline and therefore allows for an accurate simulation of ion optical elements and their aberrations. TraceWin accepts the input of the beam characteristics either via Twiss parameters or as a set of simulation particles in the 6-D-phase-space.

To avoid Coulomb explosions in the source region, the ion beam is taken as space charge compensated up to the entrance of the solenoid. The assumption, that most electrons are deflected by the magnetic mirror effect is valid, because in simulations by F. Nürnberg only 18 % of all electrons were transmitted and in the simulations presented below the solenoid fringe field at the source was taken to be even lower by a factor of 3 because of the increased distance of target to solenoid, thus reducing the number of electrons satisfying equation 4.31 even further.

4.3.2 Simulation input and setup

Instead of defining the ion beams via Twiss parameters, the ion beams starting at the source were fed into TraceWin with a set of simulation particles that correspond to the characteristics of a TNSA-generated ion beam. The input distribution of simulation particles consisted of 10^6 to 10^7 particles, which were distributed in the six dimensional phase space to match the properties of TNSA-generated ion beams. This was accomplished by the *inverse transform sampling* method [159].

The transversal divergence profiles of the heavy ions were taken to be similar to those of protons; energy dependent maximum divergence in terms of $E_{kin}/E_{kin,max}$ was taken from [46], assuming radially symmetric beams, and the probability density function as a function of the divergence angle was approximated with a negative quadratic function, since experimental data strongly suggests such a behaviour [113]. From the divergence angle of each ion and its energy, a virtual starting point could be determined. The energy dependent virtual source size and distance to the target has been measured experimentally in [108, 112]; the virtual distance to the real source, $d_{source} = 550\,\mu\text{m}$ to $200\,\mu\text{m}$, and virtual source radius, $r_{source} = 15\,\mu\text{m}$ to $2.5\,\mu\text{m}$, are decreasing with increasing proton energy. The virtual source is situated closer to the target front side. The virtual source size then defines the transversal emittance, because the starting position of the ions inside the source area was randomized.

For better visibility, 4.7 a)-d) were generated with only 10^4 simulation particles. Figure 4.7 a) shows the source distribution at $z = 0$, projected onto the target plane for a set of simulation particles emulating a C^{4+} ion beam. Higher energies are present only in a smaller area around the beam axis. From the area in figure 4.7 b) the transversal *root mean square* (**rms**) emittance equals $\epsilon_x = 0.036\,\pi\text{mm}\,\text{mrad}$. The slightly S-shaped envelope hints at non-linear effects during acceleration. The energies of the particles were distributed according to energy spectra from the source characterization (Thomson parabola) in section 3, also visible in 4.7 c), ranging from 5.5 MeV to 50.0 MeV. A very high degree of longitudinal ordering was assumed, as particles with higher energies are typically accelerated earlier in the process. The longitudinal phase space is depicted in figure 4.7 d) in terms of kinetic energy and time. The longitudinal rms emittance is then $\epsilon_{long} = 3.8 \times 10^{-6}\,\pi\text{eV}\,\text{s}$.

The goal of the simulation studies was to understand and optimize the transport of laser-driven

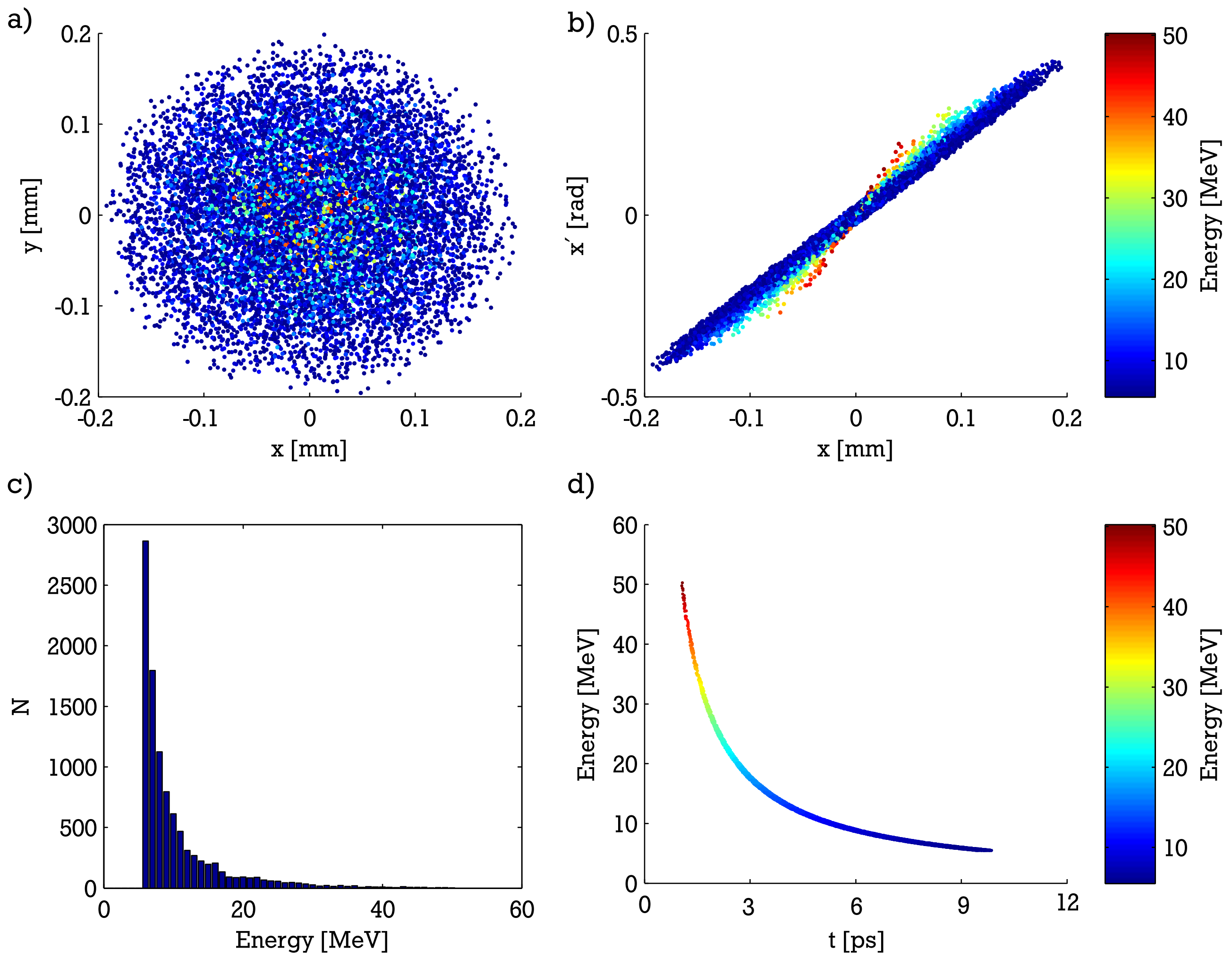

Figure 4.7: Phase space of simulation particles emulating a C^{4+} ion beam:

a) The transversal extent of ion beam at the target position changes drastically with the energy of the ions.

b) $x - x\prime$ phase space of the ions. The trajectories at a given energy are highly laminar.

c) Histogram of ions grouped in bins for their kinetic energy. The distribution was measured during the source characterization.

d) Longitudinal phase space, expressed by kinetic energy and time.

heavy ion beams in the already established LIGHT beamline [39, 42, 45, 46], with as little changes of the setup as possible. A schematic drawing of the beamline is depicted in figure 4.8. The option to move the radio frequency cavity, incorporated for the manipulation of the longitudinal phase space of the ion beam, to different positions has been added in the scope of this work. The necessity for this modification is explained in section 5. Another alteration of the beamline was the removal of the quadrupole doublets, which were used in previous experimental campaigns to improve the transport efficiency. However, simulations indicated, that they only led to minor improvements of the efficiency, and with the likely field imperfections the quadrupole doublets probably even deteriorated the ion beam and decreased the efficiency. Therefore the beamline consists of a pulsed solenoid with housing at a distance of 40 mm to the TNSA target (the coil entrance being at a distance of 80 mm) and a possible second solenoid for the final focussing of the transported ion beam. The rf cavity is not active

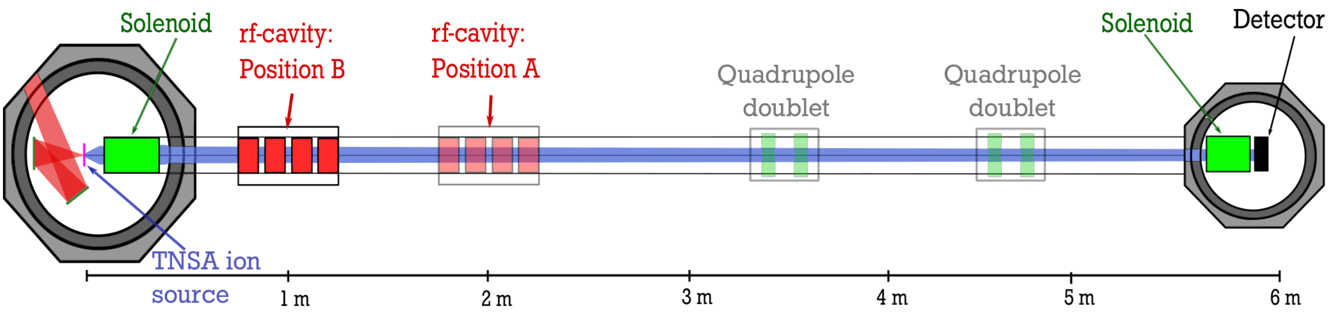

Figure 4.8: Schematic drawing of the LIGHT beamline: disregarding the removal of the quadrupole doublets and the modification of the rf cavity, only minor changes had to be undertaken.

and is only included for the reduced free aperture it confers. The pure transport simulations are conducted with the cavity switched off to avoid any effects on the transversal emittance that acceleration or deceleration of the ions in the beam might have.

In all of the simulations, the solenoid is included as a three dimensional axisymmetric field map, which has been generated using the CST simulation package by S. Busold. On axis measurements of the magnetic field, conducted by the magnetic field laboratory at GSI coincide very well with these simulations [46]. The field map is normalized to 1 kA and can be scaled arbitrarily. A section through the field map is presented in figure 4.9. Because of the axial symmetry only the upper half of the section is depicted.

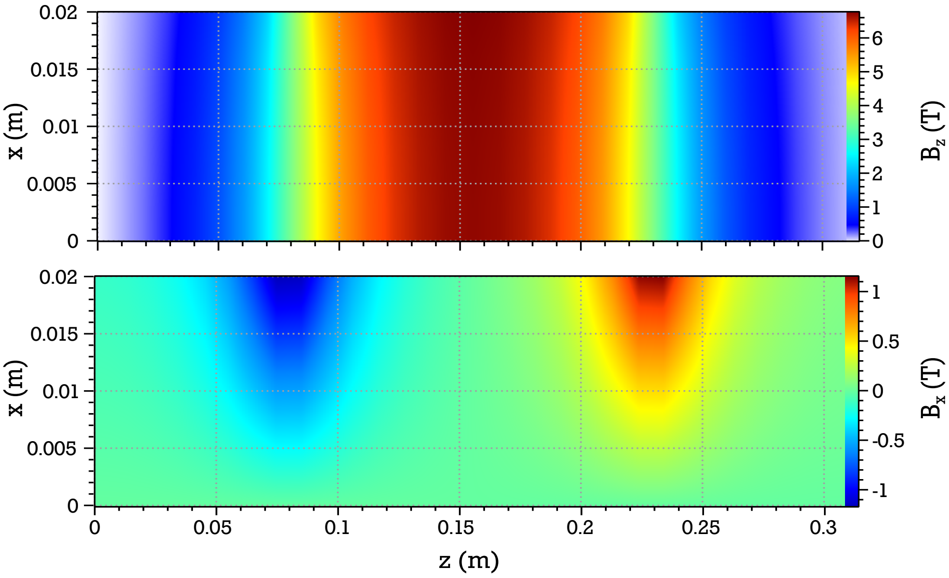

Figure 4.9: Field map of the magnetic field of the collimating solenoid. The magnetic field is axially symmetric, thus only the upper half of each cut plane is displayed. The field map has been created by simulating the current carrying coil, consisting of four layers of copper windings, with the software package CST.

4.3.3 Simulation studies on laser-driven heavy ion transport

The simulation study described in this section was conducted as a proof of concept for the collimation and transport of laser-driven heavy ion beams. The study was also preparatory work for experimental campaigns, as parameters from realistic simulations can be used as starting parameters in the experiment. A kinetic energy of around $1\,\mathrm{MeV\,u^{-1}}$ was chosen for the transmitted ion beam, because this energy is close to the kinetic energy required for possible future applications. Most of the simulations were already published in [153]. Minor changes of numbers in this section compared to the article stem from adjustments of the input distributions and changes to the assumed space charge compensation.

As a first step the influence of space charge effects was investigated. As stated in section 4.3.1 previous simulations with PIC codes support the assumption of space charge neutral drift from the source to the entrance of the solenoid coil and further propagation without any space charge compensation. Therefore the beam was fully space charge compensated for the first 80 mm and uncompensated for the rest of the beamline. From the source characterization in chapter 3 the total number of C^{4+} ions can be derived. As a first approximation the transversal profile of the ions was taken to be similar to that of protons, which is a good approximation at least in the most important central part of the beam. This yielded a total number of 10^{11} C^{4+} ions for kinetic energies ranging from 5.5 MeV to 50.5 MeV. As a consequence the initial beam charge has to be set to 64.1 nC. Additionally the fieldmap was set to emulate a solenoid from Hemholtz-centre Dresden-Rossendorf with a free aperture of 40 mm, operated at a current of 8.1 kA, resulting in a maximum magnetic field B_z of 6.72 T and square of the magnetic field integrated along axis of $5.64\,\mathrm{T^2\,m}$. The LIGHT beamline was modelled as shown in 4.8 with the defining apertures of the two solenoids, both exhibit a diameter of 40 mm, and the inactive cavity is at 1.275 m distance from the target with a free aperture of 35 mm. This setup is from here on called LIGHT beamline, if not stated otherwise.

The resulting energy spectrum of the C^{4+} ions reaching the end of the beamline is depicted in figure 4.10 together with energy spectra for 10 % of the beam charge and without any space charge effects. Accounting for the full space charge of the beam has a strong effect on the energy of the transported ions. The effect of increasing the uncompensated charge of the beam is to decrease the peak energy and the spectral width. This is mainly due to the additional defocusing of the space charge, which needs to be compensated by the solenoid lens, thus reducing the kinetic energy of the ions for which the collimation is fulfilled (equation 4.28). The full charge of 64.1 nC of the ion beam leads to a decrease of the peak by 3 MeV. From the decrease of 0.22 MeV at 10 % of that charge it can be seen, that it is a non-linear effect as expected. For better visualization all spectra are normalised, but the number of transported ions in the case of full space charge is also lower by a factor of 12.5 when compared to no space charge. The comparison of previous experimental campaigns with proton beams and TraceWin simulations, that neglected any space chage effects [46], show good agreement of experimental data and simulations. This strongly suggests, that the current treatment of space charge in the LIGHT beamline overestimates any possible effects. It can be argued, that the investigated proton beams had a higher velocity by a factor of $\sqrt{8}$ leading to a smaller effect as the proton beam diverges faster. Still, accounting for the space charge of the proton beam in simulations leads to an increase of 0.4 MeV, which is not consistent with experimental data. It is therefore likely, that additional sources of space charge compensation, besides the comoving electrons,

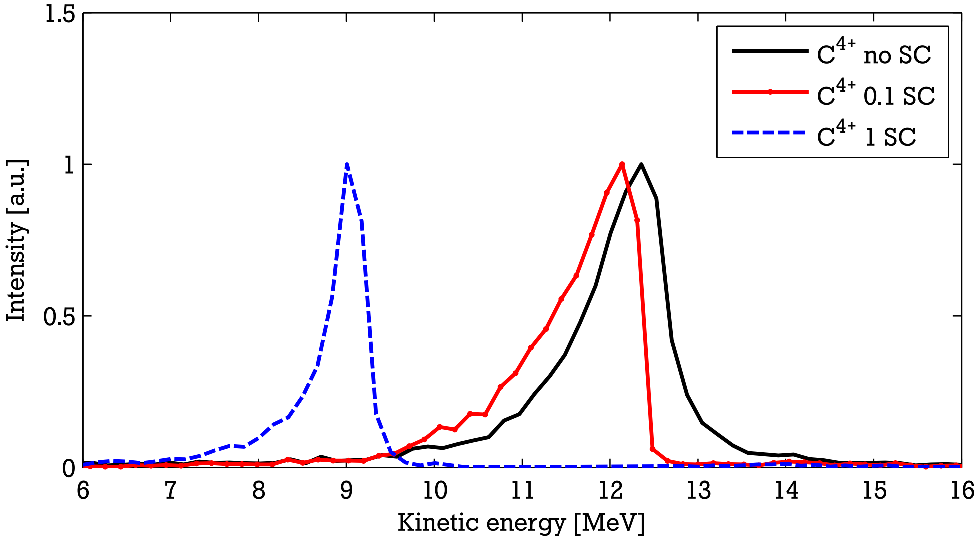

Figure 4.10: Influence of space charge effects on the transport of laser-driven heavy ion beams. Accounting for the full charge of the ion beam leads to a down shift of the peak energy by 3.3 MeV compared to the case of no space charge. The effect is already visible at 10 % of the space charge.

which are mostly deflected in the fringe field of the solenoid are not yet considered.

A possible source of electrons are the walls of the beamtube. As the biggest part of the ion beam is lost and hits the walls of the beamtube, electrons are ejected in the process. The yield of ejected electrons per ion was subject of research 30 to 40 years ago and is in the range of 10^2 to 10^3 for MeV-ions [160, 161, 162]. The kinetic energy of the electrons amounts to some 10 eV only, but they could be sucked into the ion beam and provide space charge compensation. The presence of significant populations of energetic electrons even after passing numerous solenoids acting as magnetic mirrors has been demonstrated also at other accelerators, for example the NDCX-II [163]. The beam charge at comparable ion energies is even higher in their case, while the loss ratio of ions is a lot smaller and still they see signatures at their beam monitors, that can only be attributed to electrons [164]. This supports the assumption of beam charge neutralisation in the LIGHT beamline. In the following simulations space charge effects were neglected, because from previous experience this seems to better emulate experimental realities.

In order to investigate the influence of the apertures in the beamline, four different setups were chosen. In a first step carbon with charge state 4+ is simulated over the length of the beamline of 6.05 m through a beam pipe with a 100 mm diameter. Again the solenoid fieldmap was set to emulate a solenoid from Hemholtz-centre Dresden-Rossendorf with a free aperture of 40 mm, operated at a current of 8.1 kA. In a second simulation a pinhole with a free aperture of 20 mm diameter was added in the middle between the solenoid and the monitor at 3.155 m distance to the target. Comparing the result of the simulation with aperture with a simulation of the complete LIGHT-beamline setup (apertures of cavity and second solenoid equal 35 mm and 40 mm respectively, both inactive otherwise) shows comparable energy widths with shifted peak energies (table 4.1). A LIGHT beamline without a decreased free aperture because of the second solenoid (inactive) at the end of the beamline leads to a much broader peak in the spectrum. The outcome of these transport simulations with C^{4+} is shown in figure 4.11 a).

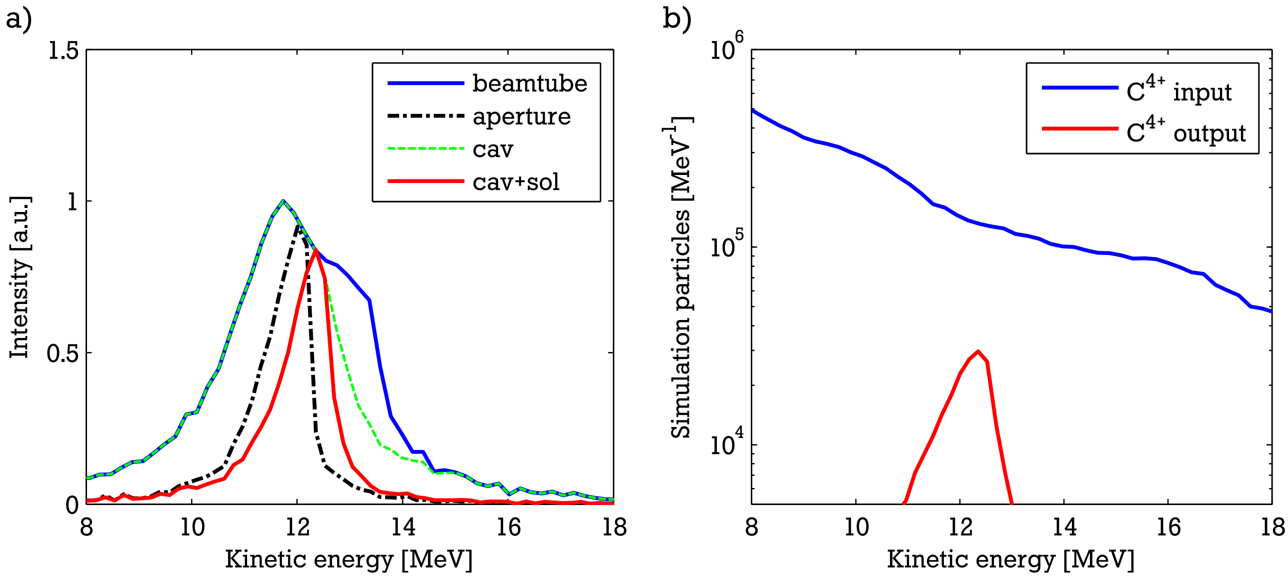

Figure 4.11: a) Simulations of laser-accelerated carbon ions with charge state 4+. For the same fieldmap of the solenoid four different beamlines were simulated. A 100 mm diameter beam tube resulted in a spectrally broad transmission. By adding an aperture with 20 mm diameter in between the solenoid and the monitor one reduces the spectral width of the transmission significantly. Taking the whole LIGHT-beamline setup without the aperture of a second solenoid results in the green spectrum. Adding the aperture of a second solenoid almost the same effect on the energetic width of the resulting beam (in red) as adding the pinhole with a free aperture of 20 mm diameter between solenoid one and detector.
b) Simulation of the output the LIGHT-beamline for a solenoid, operated at 8.1 kA in comparison with the spectrum of the input beam.

In figure 4.11 b) the input energy spectrum is depicted together with the LIGHT beamline output. For the peak energy of the output of 12.35 MeV the overall transport efficiency of the LIGHT beamline peaks at 22.7 %, whereas for the FWHM range of the peak, 11.69 MeV to 12.68 MeV the efficiency is still at 17.0 %. Going to lower solenoid currents would increase particle numbers because of the exponentially decreasing energy spectra of the input beam. Setting the peak energy to 12.35 MeV is a trade-off between the energy of the ions and overall particle numbers especially with respect to the temporal bunch compression, introduced in chapter 5.

$$\frac{1}{f} = \frac{q^2}{4\gamma^2 m^2 v_z^2} \int B^2 \mathrm{d}z \tag{4.32}$$

In figure 4.12 a) the transversal beam profile of the transmitted C^{4+} ion beam at the end of the LIGHT beamline is displayed in terms of relative density. The beam appears to be of quite homogeneous density. Figure 4.12 b) shows the input beam distribution, where the transmitted ions from 4.12 a) all stem from the area marked in dark green. All of the transmitted ions originate from starting positions close to the center of the source. This also means, that their initial divergences are small (below 120 mrad), which can be seen in the input distribution, projected onto x and x' in figure 4.12 c), where the area the transmitted ions stem from is

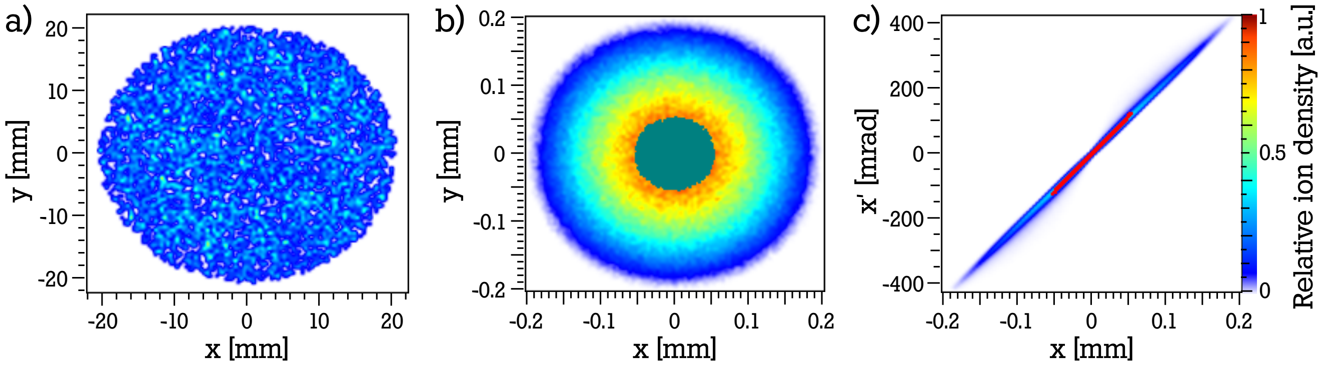

Figure 4.12: a) The transversal profile of the C^{4+} ion beam at the end of the LIGHT beamline with the above defined parameters is axially symmetrical.

b) Transversal beam profile of the input distribution. The ions transmitted, through the LIGHT beamline and displayed in dark green, all stem/originate from the center of the input distribution.

c) Projection of the input distribution onto the x-x′ phase space. Only ions with an initial divergence x′ below 120 mrad are able to reach the end of the LIGHT beamline (marked in red).

marked red. The fact that only ions with small divergences and kinetic energies below 20 MeV are transmitted further justifies the approximation in section 4.3.2 to take the divergence distribution of laser-driven carbon ions to behave like TNSA-generated protons (compare section 3.6, figure 3.12).

By using the TNSA mechanism to generate energetic ions one ends up with multiple charge states with very different energy spectra in one beam. Since the focal length of a solenoid depends on the charge to mass ratio (see equation 4.32) we expect peaks at different energies for each charge state when looking at the transport of the complete beam. In figure 4.13 the energy

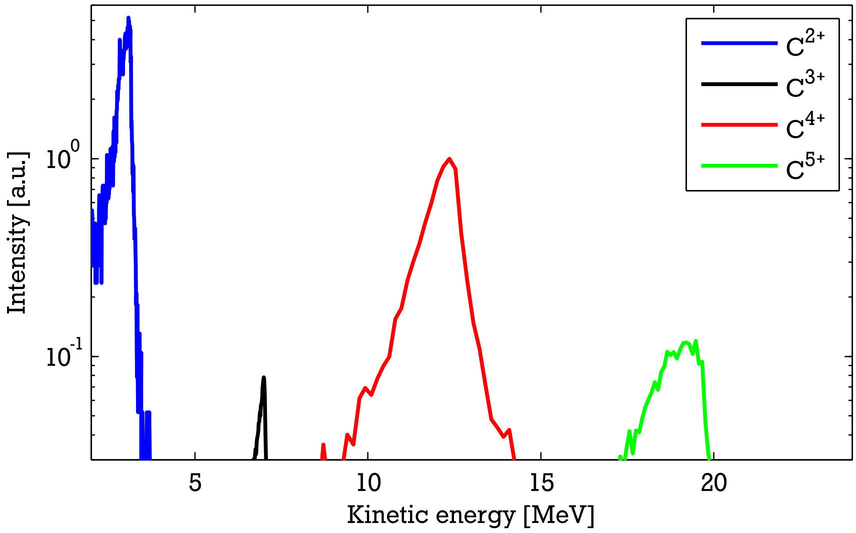

Figure 4.13: For different charge states, the focal lengths change according to equation 4.32. Therefore the lower the charge state, the lower the energy of the transported ions. The height of the peaks is normalized to the expected total particle number of C^{4+}.

spectrum of a transport simulation of a carbon ion beam barring C^{1+} and C^{6+} is shown. Protons and C^{6+} ions are not abundant in the ion beam and can therefore be neglected. At the expected peak of the energy spectrum of C^{1+} of around 0.34 MeV no simulation input distribution for C^{1+} ions exists, because the diagnostics utilized for the source characterization are not capable of investigating energies below 1 MeV. The peaks are normalized to the expected total particle number of C^{4+}. The abundance of C^{2+} ions at their respective peak energy of 3.08 MeV (see figure 3.10 for proof) leads to more ions per energy bin than even C^{4+} at their peak energy, but as this energy is much below the Bragg peak energy of carbon, these ions are not really useful for future applications. The resulting peak energies and energy widths are written down in table 4.1. The ratios of peak energies of different charge states follow a ${q_i}^2/{q_j}^2$ law well. The FWHM widths of the energy spectra scale with increasing energy of the peaks, with the exception of the C^{3+} spectrum, where the very low number of simulation particles reaching the end of the beamline might have distorted the spectrum.

	beamtube C^{4+}	aperture C^{4+}	cavity C^{4+}	LIGHT C^{2+}	LIGHT C^{3+}	LIGHT C^{4+}	LIGHT C^{5+}
E_{peak} [MeV]	11.74	12.01	11.74	3.08	6.99	12.35	19.25
E_{FWHM} [MeV]	2.90	0.90	2.24	0.34	0.23	0.99	1.63

Table 4.1: Peak energies and energy widths of carbon ions reaching the monitor at 6.05 m for a solenoid pulsed with 8.1 kA.

Another important measure for the efficient transport of ions with beam optics is the increase in emittance. By incorporating the solenoid as a field map, non-linear effects are taken into account and the emittance change can be calculated. The transversal emittance is increased mainly because of the chromaticity, which is a linear effect, according to

$$\epsilon_{trans} \propto \alpha^2 \frac{\Delta p}{p} = 0.60\,\pi\text{mmmrad}, \tag{4.33}$$

where α denotes the divergence of the ion beam and $\Delta p/p$ the relative momentum spread. At 6.03 m distance to the target, the transversal emittance grew by more than a factor of ten.

4.3.4 Simulation results and implications

As a trade-off between kinetic energy of the ions and the exponential decrease in particle numbers for increasing energy, $1\,\text{MeV}\,\text{u}^{-1}$ C^{4+} ions are intended to be transmitted through the beamline. It is expected, that all of the other charge states generated and accelerated in the source are transported with peak energies significantly separated with regard to C^{4+}. After a drift from the solenoid to the end of the beamline, the individual charge states are temporally separated by at least 90 ns, which is more than sufficient for future applications.

The transport efficiency for C^{4+} ions through the whole LIGHT beamline of 17.0 % in the FWHM range 11.69 MeV to 12.68 MeV is limited by the initial divergence of the ion beam and the apertures of both solenoids and the cavity. Assuming an initial number of ions of 10^{11} C^{4+} ions at the source leads to roughly 5×10^8 C^{4+} ions at the end of the beamline. This number should be adequate for future applications. Whether space charge effects play an important role in the transport of laser-driven heavy ion beams or not is still unclear. Comparisons with experimental data in section 4.5 should bring more insight.

4.4 Experimental setup

Several experimental campaigns were conducted to demonstrate and investigate the collimation and transport of laser-driven heavy ion beams. The most recent one took place in September 2017 and included a Thomson parabola and a fast diamond detector at the end of the six meter long beamline. The beamline has been shown in the schematic drawing 4.8.
The most crucial part of the experimental setup besides the PHELIX laser system (see section 3.2) was the pulsed high field solenoid, developed by the high field laboratory at HZDR in close cooperation with the laser-ion acceleration group on site. Already three doctoral students have dedicated themselves to the development and improvement of both solenoid and pulsed power supplies and their work has culminated in various publications. K. Harres and T. Burris-Mog started the experimental campaigns with solenoids at PHELIX [37, 38]. The work by S. Busold built on their work and culminated in the construction of the laser-driven proton beamline at the Z6 experimental area [42] with the continued support by HZDR and F. Kroll [47].

The following technical details are taken from [47]. The solenoid consists of four layers of copper windings, 28 windings in each layer, around a cylindrical coil body, made from fiber reinforced plastic, with a 54 mm outer diameter and 150 mm length. The layers are reinforced with Zylon to ensure stability under forces induced by the ramping of the magnet. The large free aperture of the solenoid of 40 mm allows the efficient capture of the highly divergent ion beam. As the Zylon-epoxy composite, strengthening the copper windings, exhibits strong outgassing, a decrease in breakdown voltage can occur (Paschen's law). Operating the coil in a vacuum compatible sealed stainless steel housing, which is connected to the outside of the target chamber via bellows, reduces the breakdown risk as well as improving the heat dissipation.

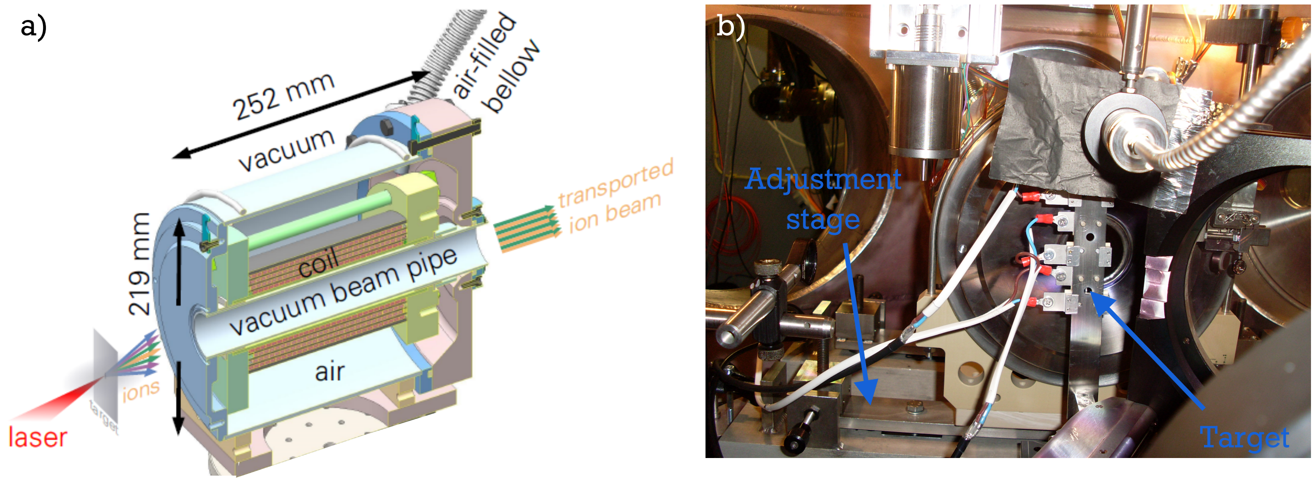

Figure 4.14: a) CAD drawing of the pulsed power solenoid developed by the HZDR, courtesy of F. Kroll [47].
b) Solenoid incorporated into experimental setup. It is mounted on a modified adjustment stage for ion optics at the UNILAC.

The CAD drawing in figure 4.14 a) shows the solenoid with the above described features. The solenoid can be operated with a peak current of up to 23.4 kA resulting in a quasi-static peak magnetic field of 19.7 T over several μs. The pulsed power supply and solenoid coil made for the LIGHT collaboration has only been tested up to 16 kA, which so far has been sufficient. The current is monitored with a Rogowski coil. The field map of the pulsed solenoid has been shown in figure 4.9. The entrance of the coil was located at 80 mm from the target rear surface, resulting in the edge of the housing sitting at 40 mm from the target. In figure 4.14 b) the solenoid is incorporated into the LIGHT beamline. The correct alignment of the solenoid is of the utmost importance, because of the impact any misalignment has on the transport efficiency. To ensure μm precision during this process an adapted and custom-built adjustment stage for ion optics from the UNILAC is utilized.

In addition to investigating the energy spectrum of the transported ions at the end of the beamline with a Thomson parabola or RIS, it is also possible to examine the temporal profile of the ion beam and use the ToF method to deduce the energy spectrum of the ions. The ToF detector in the LIGHT experimental campaigns was a **s**ingle **c**rystal **C**hemical **Va**pour **D**eposition (**scCVD**) diamond detector, designed and optimised for very short ion pulses by D. Jahn [165]. Diamond is very suitable as a material for hadron physics detectors [166]. It has a large band gap of 5.5 eV, thus making cooling for the reduction of dark current noise redundant. It exhibits a high radiation hardness and most importantly features a very high electron and hole mobility, while still being an insulator. This can be exploited by exposing the thin scCVD membrane to a strong electric field. Any electron-hole pairs that are created by the energetic ions inside the membrane, will then drift very rapidly to the metal electrodes and result in a very fast rise time of the ion signal (see also figure 4.15). The signal is proportional to the number of electron-hole pairs and can be subject to quenching effects for a very intense beam that deposits a lot of energy into the detector. As calibrating is difficult due to the attenuation of 17 dB of the detector, particle numbers cannot be determined with the diamond detector.

The utilized circular scCVD diamond membrane has a thickness of $(6 \pm 1)\,\mu$m, a diameter of 1 mm and with an applied voltage of 30 V and the specially designed circuit board to match

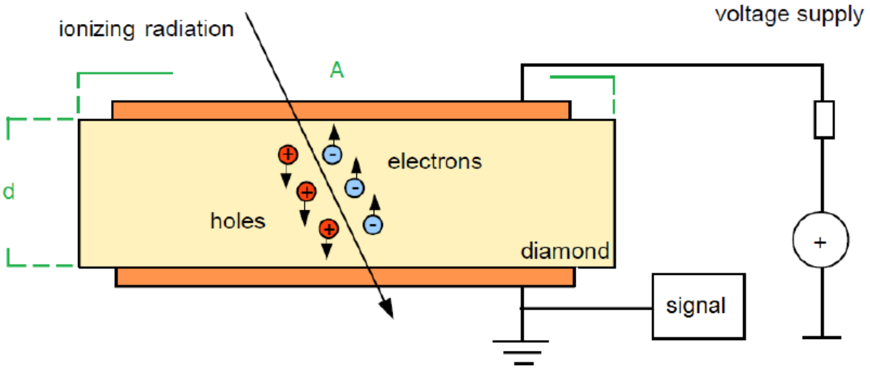

Figure 4.15: Schematic drawing of detection of ionizing radiation with a diamond detector (taken from [165]): Ion beams (or ionizing radiation) deposit energy inside the scCVD diamond membrane and generate electron-hole pairs in the process. Electrons and holes then drift to anode and cathode respectively with drift velocities depending on the electric field. The resulting signal is then a measure of beam intensity.

the impedances, it boasts a response function of (65 ± 5) ps. In the experiment the resulting currents were recorded with an oscilloscope from TekTronix, capable of a bandwidth of 8 GHz and a sampling rate of 25 GHz.

In the experimental campaign the diamond detector or the Thomson parabola were utilized at six meters behind the target (shown in figure 4.8) mutually exclusive at the same position. Another important aspect of the experimental setup was the correct timing of the pulsed solenoid, the PHELIX laser system and the data acquisition by the diamond detector. For this purpose, one of the highly accurate clocks of the UNILAC infrastructure was combined with various delay devices and specially designed timing boards (by D. Schumacher). From measured cable delays the starting time of the ions for the ToF analysis of the diamond detector read-out could be determined with sub-nanosecond precision.

4.5 Characterization of laser-driven heavy ion transport

The following section is dedicated to the characterization of laser-driven carbon ion beams, collimated by a pulsed power solenoid. The carbon ions were generated utilizing the TNSA process as detailed in chapter 3.

After setting up the detectors, pulsed solenoid with pulsed power, target and laser diagnostic, the first step for a successful demonstration of the transport and collimation of laser-driven heavy ion beams is to adjust the exact position and tilt of the solenoid to 0.1 mm precision. This process is complicated by the fact, that the axis of the magnetic field does not coincide with the geometrical axis. Thus, in practice an iterative alignment routine is applied. Starting from a position of the solenoid roughly known from previous experiments (with millimeter precision) the resulting proton beam (protons beams are easier to obtain with TNSA) is diagnosed with an RCF stack shortly behind the solenoid in the center of the beam tube. Corrections to the beam position are implemented as tilts and shifts of the solenoid. By moving the RCF stack farther away, the corrections become smaller. When reaching the position of the detectors at six meters distance to the target with sufficient accuracy, the adjustment phase is finished. The low repetition rate of the PHELIX laser of one shot every 90 min required five days of laser operation to be spent on the alignment process.

Compared to previous experimental campaigns, the latest campaign faced additional difficulties in the alignment process, caused by a change of the solenoid coil housing. The main difference between the old and new housing is that major parts of the new housing are made from polyether ether ketone instead of steel. This led to the disappearance of a localized central density feature in the transversal beam profile, visible over 5 m of drift in the case of the old housing, and complicated the pointing of the solenoid, because the center of the beam was no longer as well characterized. Investigations of this phenomenon are still under way, but a likely cause is the more efficient suppression of eddy currents in the new housing.

To begin with, the powerful capabilities of Thomson parabolas to create a charge-to-mass ratio resolved energy spectrum of ion beams in a single shot was utilized to characterize the ion beam six meters behind the target. The same Thomson parabola, previously incorporated in the characterization of laser-driven heavy ion beams in chapter 3, was operated with exactly the same parameters resulting in identical dispersion relations for the ions. The last aperture before the detector being a second structurally identical solenoid for possible final focussing at a later stage of the campaign limited the transversal extent of the beam to a diameter of 40 mm. The Thomson parabola pinhole, with a diameter of 0.2 mm was placed in the center of

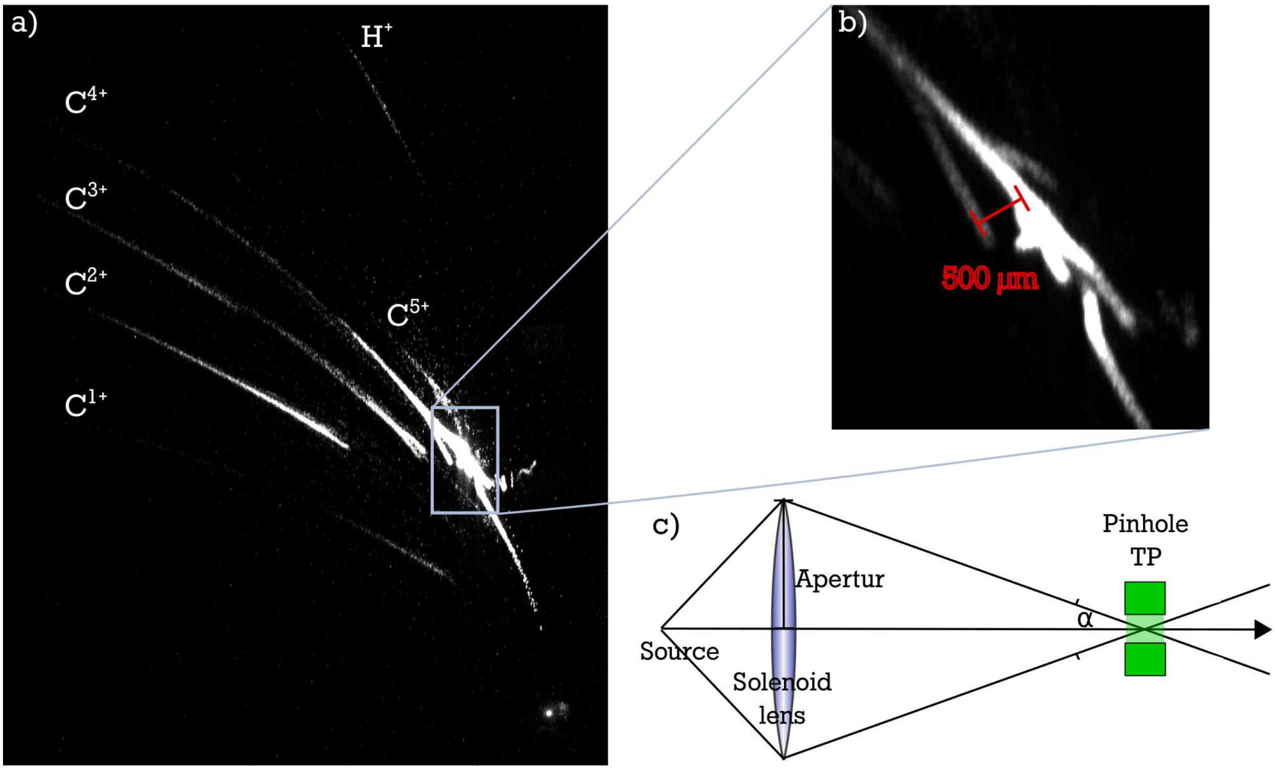

Figure 4.16: Raw data of a Thomson parabola at six meter distance from target for shot 38:
a) The image plate displays traces of carbon ions with charge states ranging from one to five and also protons. From the intensity of the traces a dominance of C^{4+} ions in the beams can be assumed.
b) At certain energy ranges the traces are fragmented and point away from the inherent dispersion parabola.
c) Ions from the outer parts of the solenoid aperture are able to enter the Thomson parabola, if their energy results in a focus close to the position of the pinhole. An offset of the ion beam axis to the axis of the beamline (Thomson parabola) would lead to a potentially large observed energy shift due to a preferential ion angle.

the beam profile. The outcome of shot 38 of the campaign in September 2017 is depicted in figure 4.16. The carbon coated tungsten target, heated to 1070 °C for 10 min, was irradiated by the PHELIX laser with a peak intensity of about $4 \times 10^{19}\,\mathrm{W\,cm^{-2}}$. The solenoid current was set to 8.92 kA for the collimation, which is a substantial change to the solenoid current of 8.1 kA, that was found to be ideal in the simulation study in 4.3.3. The reason for this change will be discussed in chapter 5 and is closely linked to a limitation of stable cavity operation. All presented simulations have been carried out with the exact parameters of the experiment.
From the traces in illustration 4.16 a), the presence of carbon ions with charge states ranging from single to fivefold positively charged and protons is evident, the same species and charge states already detected in the characterization of the laser-driven carbon ion source. Even though the image plate is depicted with a strongly enhanced contrast the dominance of C^{4+} ions in the beam can be deduced from the strength of their trace.
However, the traces differ significantly from their expected parabolic behaviour, especially in the areas of highest saturation (compare figure 4.16 b)). As the Thomson parabola is set up at six meter distance from the laser-plasma interaction, any distortions by EMP can be neglected.

A possible explanation is depicted in figure 4.16 c). By means of chromatic focussing and the broad spectrum of the ions there is always a part of the ion beam, which is focussed onto the pinhole of the Thomson parabola. The longitudinal extent of the pinhole is very small, thus allowing ions to enter the TP at an angle with respect to optical center-line. The maximum angle α, determined by distance of pinhole to solenoid and the aperture of the solenoid, is 0.2°. Therefore the distance between points of impact on the image plate of ions with an angle and ions parallel with respect to the non-deflection axis at the same energy can be as much as 1.1 mm. If the pinhole of the Thomson parabola was located exactly at the center of the transported ion beam and in case of a homogeneous beam, the angled ions should contribute to a broadening of the trace on the image plate only for energies, that are focussed close to the pinhole. The discontinuations in the C^{4+} trace hint at a fragmentation of the ion beam. A possible imperfect solenoid alignment, supported by findings of the diamond detector in figure 4.20, would lead to a shift of the pinhole with respect to the beam axis and result in breakup of the symmetry of the angle distribution. This introduces a shift in the observed energy of the ion beam. For example for C^{4+} ions at the expected beam peak energy of the transported beam of 15 MeV an average angle of 0.1° causes a shift by 2.4 MeV. This huge uncertainty is the reason for ignoring the energy spectra provided by the Thomson parabola in most of the following beam characterization.

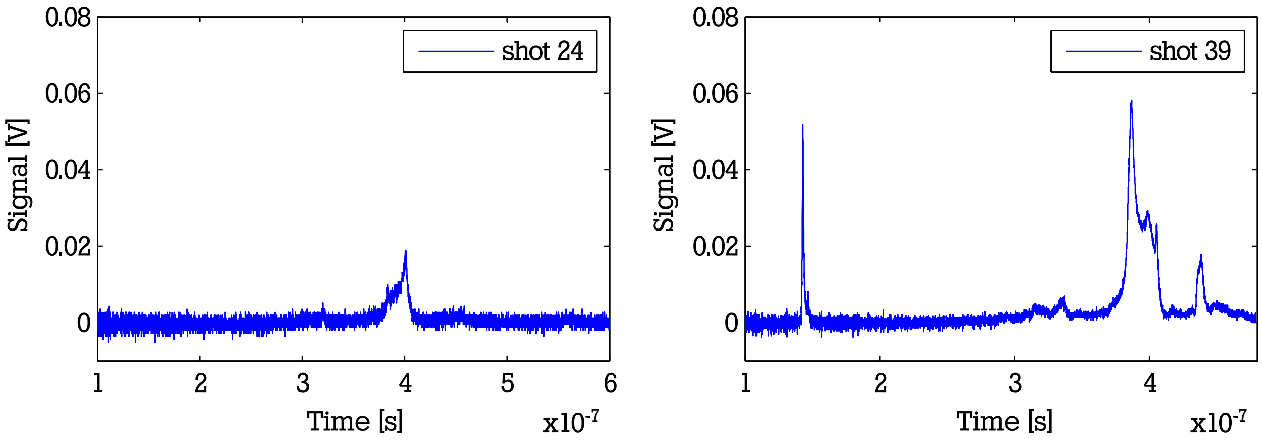

Figure 4.17: Time of flight signal at the diamond detector for two different shots: Both shots were performed with very similar parameters, but there is a large difference in the maximum signal. This can be explained by another ten shots invested for alignment purposes of the solenoid in between shots 24 and 39. The diagram of shot 39 exhibits a narrow peak for short ToF, which is due to proton remnants and indicates incomplete removal of proton contamination during the heating process.

For shots 24 and 39 a diamond detector was installed directly in front of the pinhole of the Thomson parabola. The peak laser intensity was again at around $4 \times 10^{19}\,\mathrm{W\,cm^{-2}}$ and the carbon coated wolfram targets were kept at 1050 °C for 10 min and 1010 °C for 12 min for shots 24 and 39 respectively. The solenoid currents were almost identical at 8.94 kA and 8.96 kA. In figure 4.17 the relevant sections of the ToF data for both shots are displayed. The temporal uncertainty is in the range of 0.5 ns, because the very fast response of the diamond detector and the well characterised starting time of the ions at the detector. The signal level uncertainty is dominated by the noise, which is below 0.003 V. The maximum signal is increased considerably from shot 24 to shot 39. This gain in signal stems from additional efforts undertaken to align the solenoid (overall lowering by 7.0 mm of the solenoid). Not only the signal to noise ratio is improved significantly, also the shapes of the peaks at 400 ns changes. ToF data of shot 39 also exhibits a narrow peak at 150 ns presumably caused by protons, that were not removed in the heating process. To convert the temporal signal into an energy spectrum, the signal height has to be adjusted appropriately. The associated differential transform is shown in equation 4.34

$$\frac{\mathrm{d}U}{\mathrm{d}t} = \frac{\mathrm{d}U}{\mathrm{d}t} \cdot \frac{\mathrm{d}E}{\mathrm{d}E} = \frac{\mathrm{d}U}{\mathrm{d}E} \cdot \frac{\mathrm{d}E}{\mathrm{d}t} = \frac{\mathrm{d}}{\mathrm{d}t}(m(\gamma - 1))\frac{\mathrm{d}U}{\mathrm{d}E} = m\frac{\mathrm{d}}{\mathrm{d}t}\left(\frac{1}{\sqrt{1-\frac{s^2}{c^2t^2}}} - 1\right)\frac{\mathrm{d}U}{\mathrm{d}E} = -\frac{cs^2}{\sqrt{c^2t^2-s^2}^3}\frac{\mathrm{d}U}{\mathrm{d}E}, \tag{4.34}$$

where s denotes the distance covered by the ion during the time t. The result is a general decrease of the signal for increasing kinetic energies due to its t^{-2} dependence. For the same reason also the noise level increases at lower energies and threatens to drown any spread out signals (same $\Delta v/v$ leads to bigger Δt at lower kinetic energies). The outcome of the conversion of ToF data to energy per nucleon spectra is displayed in figure 4.18. The main peaks in shots 24 and 39 remain well above the background, while at lower energies the signal-to-noise levels become problematic. The uncertainty of the kinetic energy of the heavy ions is below 1 %, as all of the distances are known with ±2 cm precision and the temporal uncertainty of the ToF data is 0.5 ns.

In the case of the diamond detector data, the assignment of signal to different ion charge states can only follow from the comparison with simulations. Fortunately the assignment is simplified by the quite substantial differences in velocities of the expected transported carbon ions with different charge to mass ratios. Plot 4.19 shows TraceWin simulations for three- to fivefold positively charge carbon ions, carried out with the exact same solenoid current as in the experiment and without space charge effects (no SC). For the simulated energy spectra all ions reaching the monitor at 6.03 m, shortly behind the second solenoid as the last limiting aperture,

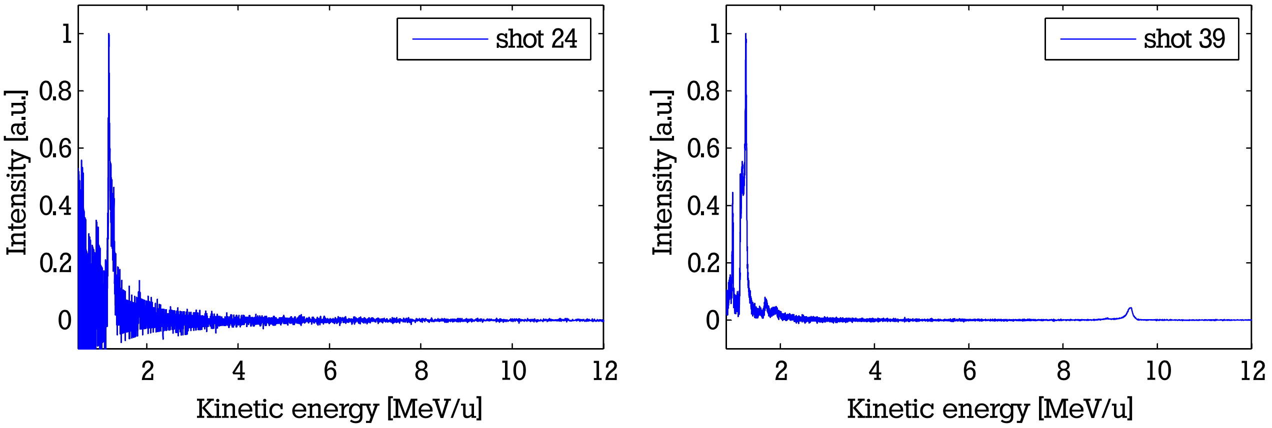

Figure 4.18: Conversion of ToF data in 4.17 to energy per nucleon spectra: It is important to convert the signal, initially given in the time domain in equally sized bins, when transforming the ToF data to velocities and energies. This transformation is also the explanation for the increasing noise level at lower energies and the changed ratio between proton and heavy ion peak for shot 39.

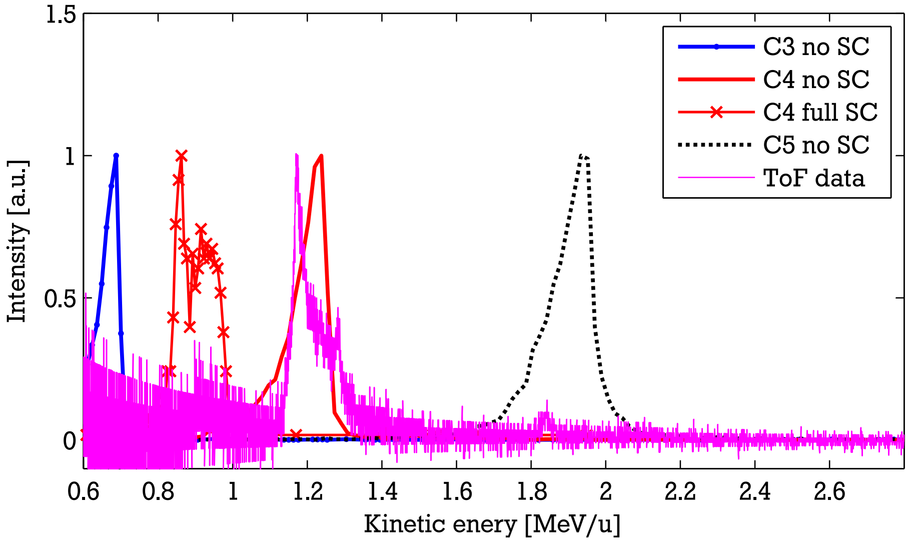

Figure 4.19: Comparison between resulting energy spectrum of shot 24 with simulations: The position of the main peak coincides very well, if not in shape then in position, with the energy spectrum from a TraceWin simulation for C^{4+} ions with the parameters from shot 24, but without space charge effects. Taking the full space charge of the C^{4+} ion bunch into account results in a down shift of the resulting energy spectrum, which is not compatible with the ToF data. There might be a very small peak roughly at the energy expected for C^{5+} ions, but C^{3+}, C^{2+} and C^{1+} ions, evident from the Thomson Parabel data, are not detected due to the high level of noise.

have been considered. The main peak of the ToF converted energy spectrum of shot 24 coincides very well with the position of the simulated C^{4+} energy spectrum without space charge.

Similar to the simulations conducted with a solenoid current of 8.1 kA in section 4.3.3, considering the full space charge of the C^{4+} ion bunch leads to a massive down shift of the resulting energy spectrum, which is not compatible with the ToF data of shot 24. Thus, the assumption of additional sources of space charge compensation seems valid. At the energy of the expected C^{5+} peak, 1.9 $\mathrm{MeV\,u^{-1}}$, only a very small bump is visible, barely above the noise level. And possible detected C^{3+}, C^{2+} and C^{1+} ions vanish in the noise at lower energies.

Although there is a good agreement of the positions of the peaks in the energy spectra of experiment (shot 24) and simulations, the shape differs significantly. On top of that, there is the change of peak shapes from shot 25 to shot 39, caused by a different solenoid alignment. This phenomenon has been studied with TraceWin simulations. The simulated transversal beam profile of all C^{4+} ions, reaching the monitor at 6.03 m, is displayed in figure 4.20 a), where the energy of the ions is denoted by a color map. The solenoid current was set to 8.96 kA and perfect alignment was assumed. The beam exhibits an axial symmetry but the slight correlation of the abundance of any given color with the radius points at a dependence of the ion energy on the radius. The beam profile in figure 4.20 b) is the outcome of a simulation with the same parameters, but with a slight misalignment of the solenoid. The field map was shifted −0.2 mm in y-direction and rotated by −0.1° around the y-axis. The result shows the loss of the beams axial symmetry. The small hole in the beam is an artefact of the limited resolution at small angles of TraceWin. The misalignment also has an influence on the energy spectrum at the position of the diamond detector.

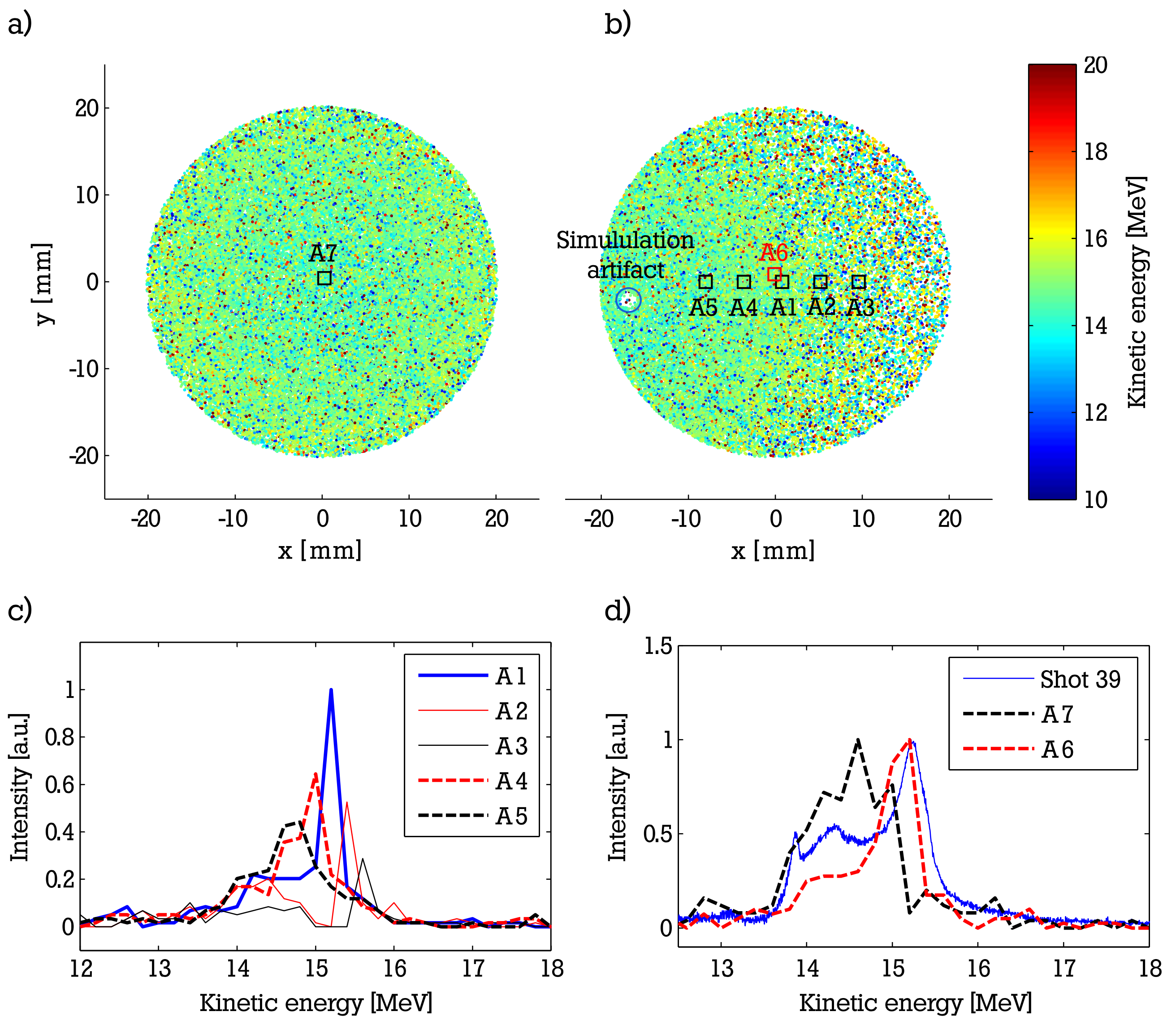

Figure 4.20: Simulation study of the shape of the energy spectrum and the influence of misalignments of the solenoid field:

a) Scatter plot of C^{4+} ions reaching the monitor at the end of the LIGHT beamline with perfectly aligned solenoid. The slight correlation of color code with radius hints at a radial dependence of the ion energy.

b) Scatter plot of C^{4+} ions reaching the monitor at the end of the LIGHT beamline with a shifted and rotated solenoid field (small margin). The small omitted area on the right side of the plot is a simulation artefact. The squares indicate the positions of the sub monitors.

c) Evaluation of the sub monitors in terms of ion energy. The energy distribution at each monitor and the integrated ion density change significantly.

d) When comparing the energy distributions in sub monitors (close to) in the center of the scatter plots for aligned and misaligned solenoid with the actual diamond detector measurement, the general shape is much better emulated by the simulation with the misaligned solenoid. Remaining differences are due to the coarse energy resolution of the simulation and non-linear behaviour of the diamond detector (measured peak signal suppressed because of saturation effects).

To consider this effect, the small detection area (1 mm^2) of the diamond detector has to be taken into account, which was neglected for the comparison in figure 4.19. In order to suppress statistical fluctuations, the considered partial areas of the monitor for the simulation was chosen to be 4 mm^2 and is further on called sub-monitor. The plot in 4.20 c) demonstrates the substantial differences of the resulting energy spectra at different positions of the sub-monitor (positions indicated in 4.20 b)). The particle density as well as the shape and position of the peak depend on the position of the sub-monitor. From this simulation the sensitivity of the beam characteristics on the quality of the alignment becomes apparent.

In order to make any statement about the complete ion beam and not just the small part, measured by the diamond detector, one has to rely on simulations. By comparing the energy spectra of the simulations with varying solenoid misalignment in a small central sub-monitor with the measured energy spectrum from the diamond detector, the solenoid misalignment in the simulations could be optimised to best emulate the measured spectrum. The resulting energy spectrum of an optimised misalignment in comparison with a perfectly aligned solenoid and the measured energy spectrum is depicted in figure 4.20 d). At position A6, close to the center of the monitor, the simulated energy spectrum fits the measured spectrum from shot 39 very well, whereas the shape of the energy distribution for the aligned solenoid has no resemblance. This is in itself a strong indication of a misalignment of the solenoid. Unresolved differences can be attributed to the non-linear behaviour of the diamond detector and coarser energy resolution of the simulation. As the whole comparison was done by trial and error and by hand, it is difficult to give a good estimate of the uncertainty. From the difference of average energies and the different FWHM of the peaks, an uncertainty on the whole comparison of ±0.1 MeV is estimated.

When comparing the transport efficiency for a perfectly aligned solenoid with the assumed misalignment the particle loss from the misalignment amounts to 28 %. The small penetration depths of the carbon ions in materials make a measurement of the beam properties of the entire beam very difficult. With a sufficient number of shots a scan of the transversal beam profile with a diamond detector would be feasible, but this would need a great number of shots and with the present limitations on the repetition rate is not economical. On top of that, the non-linear behaviour of the diamond detector and heat load induced fluctuations of the laser performance complicate any investigation of the ion beam intensity at different positions. The enhanced RIS method, introduced in section 3, generally allows only for a very coarse energy resolution, which is not sufficient to detect changes of the kinetic energies of carbon ions on the MeV-level. The approach presented in this work is based on a combination of RCF and Thomson parabola. The sensitive layer of a single RCF of the type EBT (in this case without substrate layer on the front side) stops all carbon ions in the expected energy range. Assuming a relatively small change of energy across the beam profile leads to fluctuation in beam density being accountable for any change of coloring on the RCF. Plots 4.21 a) and 4.22 b) display the resulting RCF in original coloring and with a colorcode representing a conversion to deposited energy per pixel respectively.

From the findings of the Thomson parabola measurements, that C^{4+} ions dominate the deposited energy strongly, C^{4+} ions can be assumed to cause almost all of the coloring of the RCF. The diagonal streak, indicating a more intense beam in this area, stems from the astigmatism of the solenoid. The solenoid coil consists of helical windings, which are tilted with respect to the beam propagation axis. The four layers are alternately tilted towards the axis, but the effect of tilting cannot be compensated completely. The impact on the transversal

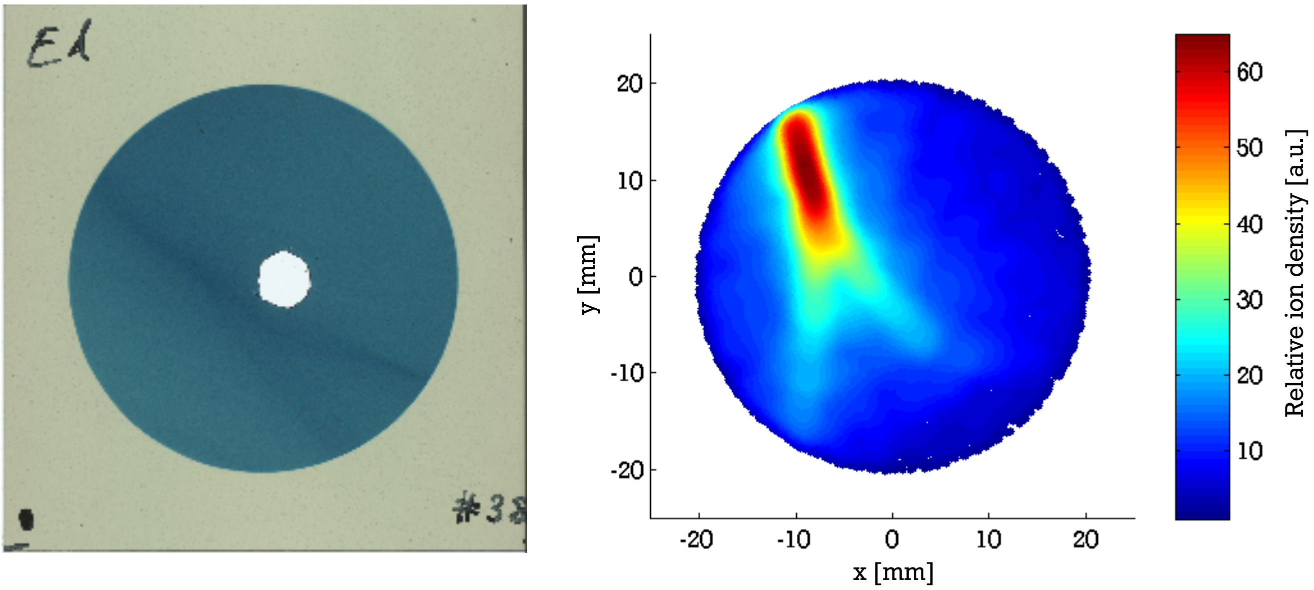

Figure 4.21: a) Radiochromic film positioned directly in front of the Thomson parabola with a hole to allow for an unobstructed line of sight. The streak, crossing the RCF diagonally, is assumed to be caused by density fluctuations in the transversal beam profile.
b) TraceWin simulations with an added quadrupole field over the length of the solenoid coil were able to reproduce the shape of the streak.

beam profile is the formation of line-shapes through the beam center, which have a different orientation depending on the considered energy range. This effect can be examined especially well with proton beams and RIS. S. Busold [46] and F. Kroll [47] have both observed this phenomenon and emulated it in simulations. Thus, the main effect of the astigmatism of the solenoid is a change of the beam profile, but not so much of the overall energy spectrum of the ions. The effect can be reproduced in simulations by adding a quadrupole field to the solenoid field map. A quadrupole with a gradient of $-0.425\,\mathrm{T\,m^{-1}}$, acting along the length of the solenoid coil, was sufficient to produce a very similar streak as observed in the experiment. An additional rotation of the magnetic fields about the x-axis with a similar angle as for the scatter plot in 4.20 b) and a shift of the beam monitor in positive x-direction in order to save working memory for the simulation, corresponding to a shift of the solenoid in negative y-direction, results in a good replication in figure 4.21 b) of the general shape of the forked streak on the RCF, displayed in figure 4.21 a). Thus TraceWin simulations have been demonstrated to be quite capable tools to emulate the transport of carbon ions with real solenoids, taking into account misalignment, solenoid astigmatism and the limited detection area of the diamond detector.

All attempts to measure the transported particle number directly with a variety of different Faraday cups or via beam induced voltages, have failed due to strong EMPs emanating from the laser-plasma interaction. To not depend completely on the simulations for any measure of actual numbers of transported particles the deposited energy per pixel on the RCF can be combined with the measured energy spectrum of the Thomson parabola. The hole in the RCF, indicated in figure 4.22 b) and necessary for a free line of sight for the TP, has been filled in with an iterative interpolation algorithm. As typical features in the transversal ion beam density are bigger than the hole in the RCF, the filling does not introduce any significant uncertainty. By comparing the

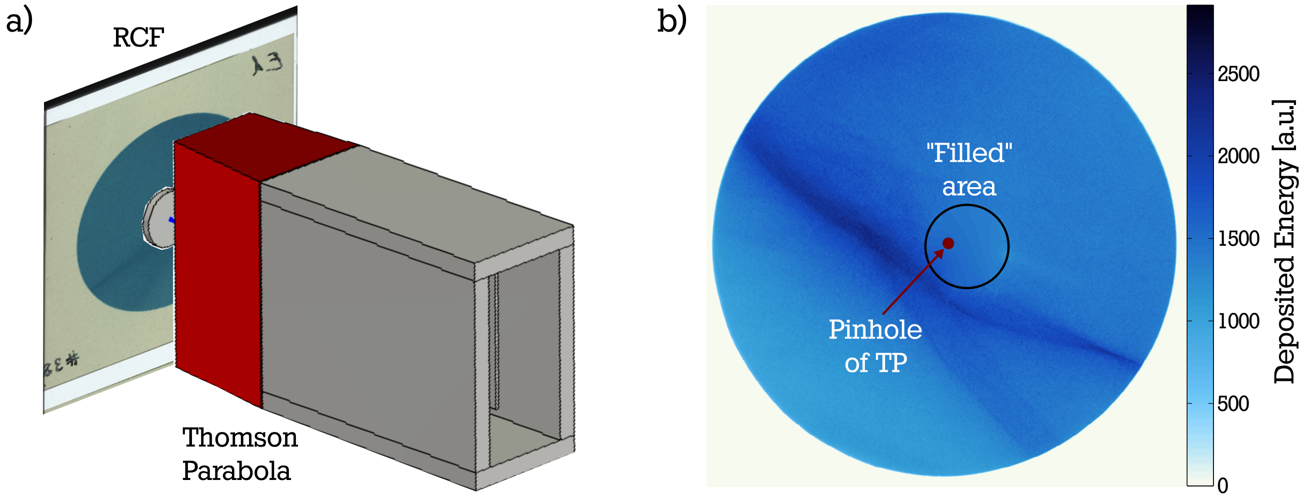

Figure 4.22: Combination of RCF and Thomson parabola to extract beam characteristics:
a) A single RCF of type EBT, custom-built with only one layer of substrate and with a hole to allow an unobstructed line of sight for the Thomson parabola, was put in front of the TP. Thus the findings of TP and RCF can be combined.
b) Deposited energy per pixel is a measure for the transversal beam density profile. The hole in the RCF was filled by interpolating between the surrounding pixels. The area, where the pinhole sat behind the RCF is indicated, but not true to scale.

deposited energy in the area of the pinhole with the integrated deposited energy of the complete RCF, one can retrieve a factor to estimate the total ion number summed up over the whole area of the RCF just from the ions detected in the Thomson parabola (see figure 4.22 a)).

As stated before, the energy allocation in the Thomson parabola is flawed by the non-vanishing angle of ions focussed in the proximity of the pinhole. Therefore the energy spectrum of shot 38 (raw data in figure 4.16) is scaled to better account for the energy spectrum measured by the diamond detector. This is important, since the number of ions relies on the energy dependent response function of the image plate. For the total number of C^{4+} ions in the whole beam there are three uncertainties.

First there is the uncertainty connected to the conversion of the image plate signal to ion quantity. As stated before in section 3.3.2, this uncertainty depends on the calibration and the energy uncertainty; in the present case the combined uncertainty amounts to 17 % because of the broadening of the ion trace, caused by the ion optic.

Second there is the uncertainty where exactly in the interpolated area of the RCF the pinhole of the TP was situated. For a realistic misalignment of the pinhole of the TP around the center of the beam imprint on the RCF (not center of the hole in the RCF, compare figure 4.22 b)) an uncertainty of 5 % and −9 % is determined.

The third uncertainty is caused by the energy deposition in the RCF. The RCF routine is not calibrated for carbon ions, but as it is reasonable to assume a linear colouring behaviour for the expected energy range of C^{4+} ions being absorbed by the RCF, and only the ratios of deposited energies are required to calculate a scaling factor for the ions detected in the TP, it can still be utilized in this setup. However, because of the dependency of the kinetic energy of the ions on their transversal position another uncertainty of the total ion number is introduced, here estimated to be 5 %. The combined uncertainty is calculated simply by adding each of the three uncertainties, because Gaussian error propagation is not applicable here. The total number of ions is then

$$N_{total}(C^{4+}) = N_{TP} \cdot F_{RCF} = N_{TP} \cdot \frac{\int_{RCF} \frac{\mathrm{d}E_{dep}}{\mathrm{d}A} \mathrm{d}A}{\int_{pinhole} \frac{\mathrm{d}E_{dep}}{\mathrm{d}A} \mathrm{d}A} = 9.9^{+2.7}_{-3.1} \cdot 10^{8}, \tag{4.35}$$

where N_{TP} is the number of C^{4+} ions detected in shot 38 inside the Thomson parabola. From simulations an average energy of (14.9 ± 0.1) MeV of the C^{4+} ion bunch at the end of the LIGHT beamline could be deduced. $6.2^{+1.7}_{-1.9} \cdot 10^{8}$ of the $9.9^{+2.7}_{-3.1} \cdot 10^{8}$ C^{4+} ions had kinetic energies within the FWHM energy of the transmitted spectrum of (14.0 ± 0.1) MeV to (15.8 ± 0.1) MeV. It has to be noted that this number of ions is subject to shot-to-shot variations caused by fluctuations of the laser energy inside the focal spot on the target front side (energy of laser pulse, wave front aberrations, etc.). Overall the number of ions can vary by as much as a factor of two.

4.6 Results

The efficient transport of a substantial amount of fourfold positively charged carbon ions could be demonstrated, both in simulations and experimentally. At an average energy of (14.9 ± 0.1) MeV an estimate of $9.9^{+2.7}_{-3.1} \cdot 10^{8}$ C^{4+} ions were transmitted to an area of $12.6\,\mathrm{cm}^2$, $6.2^{+1.7}_{-1.9} \cdot 10^{8}$ of the ions had kinetic energies within the FWHM energy of the transmitted spectrum of (14.0 ± 0.1) MeV to (15.8 ± 0.1) MeV. These ion numbers were only obtainable experimentally with a combination of radiochromic films and Thomson parabola, that circumvented the small penetration depth of low energy heavy ion beams. Considering the predicted transport efficiency of the LIGHT beamline, which leads to 4.6×10^{8} C^{4+} ions at an average of 14.92 MeV for 1×10^{11} C^{4+} ions in an energy range of 5.5 MeV to 50 MeV, the estimated ion number from the experiment is surprisingly high. However, shot-to-shot variations as well as an overall increased laser intensity on target in the latest experimental campaign compared to the campaign, in which the source characterization was conducted, resolve this disparity. As expected from simulation studies, all of the originally generated carbon charge states can be observed at the end of the beamline, if only as very faint signals with a Thomson parabola. It turned out that Thomson parabolas are generally not suited to give an accurate energy spectrum in the presence of ion optical elements in the beam because of the chromatic focusing of parts of the ion beam onto the pinhole.

Because of the small detection area of both TP and diamond detector, any statement about the characteristics of the whole beam is based on TraceWin simulations. Comparisons of simulations and experimental data showed good agreement, when reasonable assumptions about possible misalignments are included. The initial hypothesis that space charge effects start to play bigger role for the transport of heavy ion beams could not be confirmed, as simulations without accounting for any space charge reproduce the experimental data better than completely uncompensated space charge. Further investigations are necessary and should be accompanied by simulation studies with software packages capable of including interactions of different ion species and charge states and electrons. A possible software package would be the WARP code, which can also account for interactions between the ion beam and the beam tube.

The emittance of the laser-driven heavy ion beam as a measure of beam quality, could not be measured in the scope of this work. The main problem is, that the proposed method of introducing a transversal mesh of pinholes in the beam, a so called pepper pot, and the subsequent investigation of traces on a stack of RCFs farther downstream, relies on the energy and ion species discrimination of the detected trace. Therefore the usual difficulties of RIS of heavy ion beams prevent the method being used successfully.

The good agreement of simulations and experimental data allows for proficient simulations to investigate the temporal bunch compression of the LIGHT beamline for laser-driven C^{4+} ion beams. Comparisons between ToF data from the diamond detector, density profiles on RCFs and simulations can also help in the alignment process.

5 Temporal focusing of laser-driven ion beams

After having accelerated and characterized a broad spectrum of carbon or fluorine ions in the TNSA scheme and subsequently collimated and transported a much narrower part of the energy spectrum of the initially highly divergent ion beam with a pulsed power solenoid shortly behind the source, the next step within the LIGHT project is a longitudinal compression of the ions. Even 5.7 m of drift after the solenoid and a limitation of the free aperture by the second solenoid allow for a significant energy spread of the transported ion beam. In the case of the transport of carbon ions, which are fourfold positively charged, with an average kinetic energy of 1.25 MeV u^{-1}, the FWHM energy width is still 0.14 MeV u^{-1}. Thus, the bunch of C^{4+} ions reaching the end of the beamline has been diverging from the source onwards resulting in a FWHM bunch length of 25 ns.

For possible applications of the laser-driven heavy ion beam, such as energy loss of ions in dense plasmas or the injection into bigger accelerators, both the bunch length as well as the energy spread are challenging problems. The maximum acceptable energy spread of for example the heavy ion synchrotron at GSI, SIS-18, is on the sub-percent level (0.2 %). The transversal emittance has to be below 5 π mm mrad, which is already accomplished according to simulations. For energy loss measurements a small energy spread is also important. The bunch length is an even bigger challenge, since significant altering of the dense plasmas by hydrodynamic expansion is already happening within several nanoseconds.

The aforementioned reasons make it necessary to compress the beam longitudinally. In the LIGHT project this is achieved with a radiofrequency spiral resonator, in which a longitudinal electric field acts on the ions and therefore changes their kinetic energy. The first section will give a short introduction to longitudinal compression within LIGHT and the status of the beamline before applications to heavy ion beams, followed by a theoretical excursus on bunching and compression. Realistic implementations into TraceWin give a limit for achievable shortest bunch lengths before presenting data from experimental campaigns on bunching of fluorine and carbon ion beams. A conclusion then completes this section.

5.1 Principle of phase focusing and its status within LIGHT

Within the scope of the PhD thesis by S. Busold [46] a *three gap radiofrequency spiral resonator* (**rf cavity**) has been incorporated into the LIGHT beamline. This rf cavity was previously utilized for bunching and acceleration of ions in the UNILAC and a full characterization of the cavity design and application can be found in [167]. The cavity resonator is a cylinder, coated with copper on the inside and with small inlets for the ion beam on the axis of symmetry, which gives rise to a standing electromagnetic wave. The conductive cylinder closing covers reflect the radiofrequency waves, which are fed to the cavity by cylindrical wave guides. The resonant standing wave can only develop, if the capacity and impedance of the cavity are matched to the wave frequency. The cavity resonator can be described as a *damped LC circuit* with a very high Q-factor leading to a strong resonant amplification of the amplitude and thus a narrow bandwidth. The Q-factor depends on the resonance frequency ω_0, the capacity C, the inductivity L and the shunt impedance R

$$Q = \frac{\omega_0}{\Delta\omega} = \frac{R}{\omega_0 L} = \omega_0 RC, \tag{5.1}$$

which is responsible for the consumption of the rf power P_{rf} by ohmic heating. From the shunt impedance the peak voltage in the cavity can be derived.

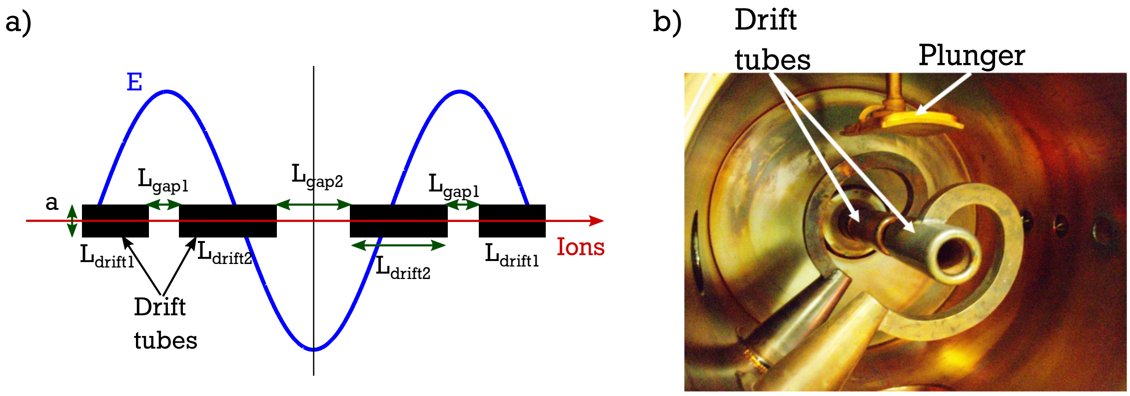

Figure 5.1: a) Schematic drawing of the three gap spiral resonator. It consists of three gaps with varying gap lengths and drift tubes in between. Technical details can be found in table 5.1.
b) Photograph of the inside of the three gap spiral resonator. The drift tubes, held in place by spiral arms, are visible as well as the plunger utilized to control the resonance frequency of the resonator (taken from [46]).

A schematic drawing of the rf cavity is depicted in figure 5.1 a). Ions traversing the cavity only experience an electric field in the gaps between the drift tubes. In the photograph 5.1 b) the spiral arms holding the drift tubes in place and after which the resonator design is named are displayed. The plunger in the top of the picture is utilized to control the resonance frequency of the cavity. The technical details of the three gap spiral rf resonator can be found in table 5.1. By inserting drift tubes along the beam axis, the standing wave is concentrated in the gaps in between.

$$U_{peak} = \sqrt{2P_{rf}R} \tag{5.2}$$

The amplitude of the standing wave oscillates with the rf frequency of 108.4 MHz. The absolute amplitude and phase of the standing wave inside the resonator has been simulated and the longitudinal part (direction of propagation) is displayed in figure 5.2. The electric field is concentrated on the area between the gaps and is homogeneous in this area (no deception by logarithmic scaling in figure 5.2 a)). There is a phase shift of π between gaps, caused by the nature of the standing wave, also depicted in 5.2 b). Ions with the design kinetic energy of $8\,\mathrm{MeV\,u^{-1}}$ experience the same phase ϕ_0 of the electric field at each gap, resulting in an overall change of their kinetic energy of

$$\Delta E_{kin} = U_{cav} \cdot q = (2U_1 + U_2) \cdot q = qU_{peak} \cdot \cos(\phi_0), \tag{5.3}$$

Geometrical dimensions			Electrical properties	
Diameter	500 mm		Resonance frequency	108.4 MHz
Length	550 mm		Shunt impedance	21.8 MΩ
Open aperture a	35 mm		Quality factor Q	6000
Aperture drift tube length L_{drift1}	85 mm		Maximum rf power	> 100 kW
Length of gap between aperture and spiral drift L_{gap1}	20 mm		Design particle velocity	8 MeV u^{-1}
Spiral drift tube length L_{drift2}	150 mm		**Plunger**	
Length of gap between two spiral drifts L_{gap2}	40 mm		Frequency shift	1 MHz

Table 5.1: Technical details of the three gap spiral resonator incorporated into the LIGHT beamline. Taken from [167], with design inspiration from [46].

where q denotes the charge of the ions, U_1 and U_2 describe the gap voltage of outer and inner gaps with $2U_1 \approx U_2$ due to the difference in gap lengths and U_{peak} equals equation 5.2. The periodic change of the gap voltage results in a dependence of the gap voltage on the longitudinal position of the ions with respect to the synchronous particle. When ϕ_s is the injection phase of the synchronous particle, then the ions experience $qU_{peak} \cdot \cos(\phi_s + \phi_{ion})$, where ϕ_{ion} is negative for ions arriving before the synchronous particle. In figure 5.3 the principle of phase focussing is

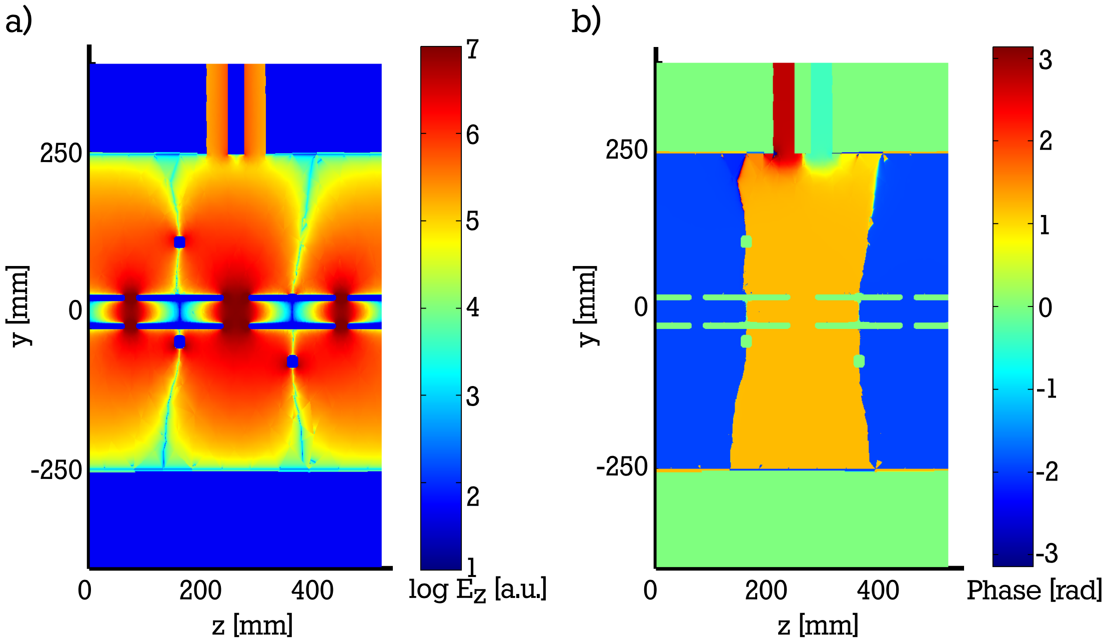

Figure 5.2: Field map of the longitudinal electric field inside the resonator and its corresponding phase (courtesy of D. Schumacher).
a) The electric field is concentrated in the gaps between the drift tubes and homogeneous in this area. The change of the kinetic energy of an ion depends linearly on the gap length for homogeneous electric fields.
b) Additionally there is a phase shift of π between each gap, which plays an important role in the effective change of kinetic energy of an ion after all three gaps.

depicted. In order to accelerate ions, the synchronous particle is usually not injected at a phase of 0° but somewhere between −90° and 0° (see figure 5.3 a)). The ions gain significantly less energy on average in this case, but in a sequence of resonators they are confined to a certain range of phases with respect to the synchronous particle. This leads to the relative momentum spread being decreased over the sequence of resonators. For ions to be confined to the bunch, they need to fulfil requirements on the relative momentum and phase difference with respect to the synchronous particle. The confinement is often called *rf bucket* and is displayed in the lower part of 5.3 a). It can be understood, when considering an ion with $\phi - \phi_s > 0$ but the same momentum $p - p_s = 0$. It reaches the gap at a later time and thus experiences a bigger accelerating voltage than the synchronous particle. As now $p - p_s > 0$ holds true, the phase difference to the synchronous particle decreases and at subsequent resonators, the additional gained momentum decreases as well. For small phase differences $\phi - \phi_s$, the change of relative momentum and phase of the ions with respect to the synchronous particle from one resonator to the next can be described by ellipses around the synchronous particle and the stable area of operation in a sequence of resonators is indicated by the *separartrix*, which limits the rf bucket and can only be computed numerically.

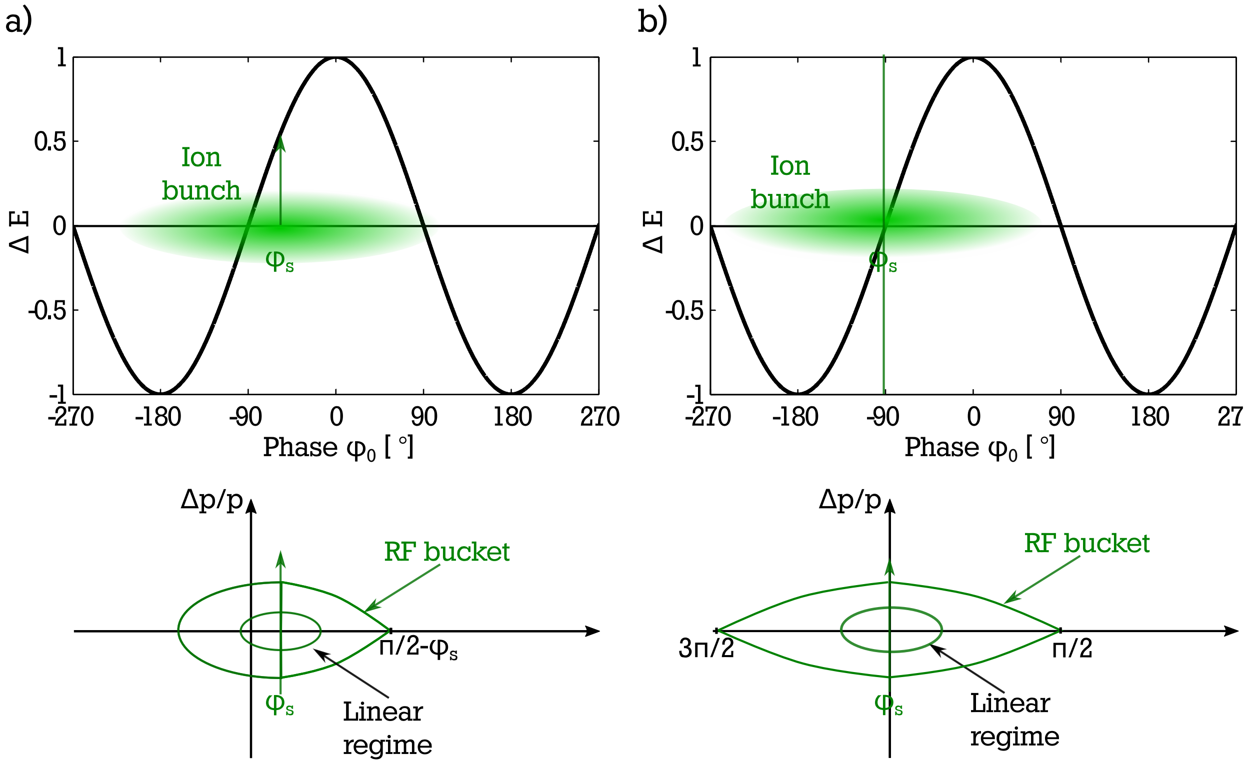

Figure 5.3: Stable acceleration of ion bunches with resonators:
a) By injecting the synchronous particle significantly below the maximum of the accelerating field, a stable operation mode for the acceleration in a series of resonators can be found, limited by the rf bucket. In a ϕ-$\Delta p/p$ plot particles with small deviations ϕ from the phase of the synchronous particle move along ellipses while traversing the sequence of resonators.
b) The bunching capability of a resonator can be maximised by injecting the synchronous particle at −90°. Thus the ions gain no energy on average, but with growing distance the longitudinal size of the bunch decreases after the resonator.

In the LIGHT project only one resonator is available and the main goal is to decrease or even reverse the momentum spread of the ion bunch. In this case an ideal injection is at $\phi_{resonator} = \phi_s = -90°$, which also becomes apparent from the size of the rf bucket in 5.3 b). The very high degree of ordering in the TNSA-generated ion beam, with high velocity ions in the front of the beam and low velocity ions at the back of the beam, allows for an efficient reduction of the momentum spread. With sufficient rf power, the momentum spread can even be reversed, resulting in an ion beam with a shrinking longitudinal extent. As the ions in the front of the ion bunch are now slower than the ions in the back of the ion bunch, the bunch becomes shorter. Neglecting the longitudinal emittance, which limits the degree of longitudinal order, the complete bunch, that experiences the linear part of the sinusoidal amplitude oscillation, can be focussed on to the phase of the synchronous particle.

By controlling the phase of the cavity relative to the time the laser impinges on the target, the phase of the ion injection into the cavity ϕ_s can be varied. Proper selection of this relative phase as well as the overall accelerating amplitude U_{peak} via the input rf power P_{rf}, resulted in a decrease of either energy spread or temporal length of laser-driven proton beams. Within the scope of the PhD thesis and short ensuing employment of S. Busold, this work culminated in proton bunches at 9.7 MeV with a FWHM energy spread of $(2.7 \pm 1.7)\,\%$, containing $(1.7 \pm 0.3) \times 10^9$ protons [45] at a distance of 3 m to the target. Increasing the gap voltage at a similar relative phase followed by 3.5 m of additional drift, enabled a reduction of the temporal length of a proton beam with 7.8 MeV to a FWHM length of (462 ± 40) ps, containing at least 1.5×10^8 protons [39].

5.2 Modifications for the efficient phase focusing of heavy ion beams

While the paragraph above covers the basic principle of phase focusing, there are a number of intricacies, that play a bigger role for the phase focusing of laser-driven heavy ion beams compared to proton beams. In section 4 the successful transport of C^{4+} ions has been demonstrated. Assuming a perfectly aligned collimating solenoid, the transported ion bunch has a center of gravity energy of 14.8 MeV with an rms energy spread of 1.6 MeV. Both values of the complete heavy ion beam are only accessible via TraceWin simulations, which have proven to emulate experimental realities very well. On the other hand, the energy and energy spread of the transported proton beam, chosen for phase focussing, are 7.8 MeV and rms 1.5 MeV respectively. The large mass difference between carbon ions and protons, results in a severe difference in velocities, which in turn gives rise to two major differences between the focussing of carbon ions and protons.

Expressing the kinetic energies of the two different ion bunches in terms of energy per atomic mass unit, $7.8\,\mathrm{MeV\,u^{-1}}$ for protons and $1.23\,\mathrm{MeV\,u^{-1}}$ for C^{4+} ions, reveals a major problem in the case of phase focusing of heavy ions. Their energy is much below the kinetic energy the cavity was designed for, i.e. $8.0\,\mathrm{MeV\,u^{-1}}$. The existence of an ideal velocity for the cavity is owed to the cavity consisting of three gaps, in which the acceleration is taking place. The utilized cavity is a so called *Wideröe* structure, meaning, that the phase of the central gap is shifted by π with respect to the outer gaps, see figure 5.2 b). An ion traversing a gap gains energy according to

$$\Delta E_{kin} = q \cdot U_{gap} = q \cdot \int_{L_{gap}} E_z \mathrm{d}z. \tag{5.4}$$

While propagating through the drift tube, the amplitude oscillates with the cavity frequency f_{cav}. Thus, when the ion reaches the central gap, the amplitude of the electric field reads as

$$E = E_0 \cdot \cos\left(\phi_1 + \pi + \frac{L_{drift}}{v_{ion}} \cdot f_{cav} \cdot 2\pi\right), \tag{5.5}$$

where E_0 is the amplitude of oscillation, ϕ_1 the phase of the oscillation at the first gap, L_{drift} the length of the drift tube and v_{ion} the velocity of the ion. To maximize the efficiency of the cavity, the length of the drift tube needs to be $L_{drift} = \frac{(2n+1)\cdot v_{ion}}{2 f_{cav}}$. Therefore such a Wideröe cavity is only designed for a certain ion velocity. Because of the ratio of gap lengths of 2:1 of central gap to outer gaps, the gap voltage $U_{center} = U_2$ equals $2U_{outer} = 2U_1$ from equation 5.3. Then the total gap voltage over all three gaps can be written as

$$\begin{aligned} U_{tot} = U_2(v_{ion}) + 2U_1(v_{ion}) = 2U_1\cos(\phi_2) + U_1 \cdot \cos\left(\phi_2 + \pi + \tfrac{L_{drift}}{v_{ion}} \cdot f_{cav} \cdot 2\pi\right) + \\ + U_1 \cdot \cos\left(\phi_2 - \pi - \tfrac{L_{drift}}{v_{ion}} \cdot f_{cav} \cdot 2\pi\right), \end{aligned} \tag{5.6}$$

as long as the relative change of velocity at each gap is small enough to be negligible. In this equation ϕ_2 denotes the cavity phase at the central gap. The resulting total gap voltage for a range of velocities, expressed in terms of kinetic energy per nucleon, can be seen in figure 5.4, depicted as U_{eff}. The effective gap voltage is maximal not only at $8\,\mathrm{MeV\,u^{-1}}$, but also at lower kinetic energies, satisfying the relation $v_{ion} = v_{design} \cdot \frac{1}{2n+1}$. This means, that efficient phase focussing is possible at kinetic energies of $8\,\mathrm{MeV\,u^{-1}}$, $0.89\,\mathrm{MeV\,u^{-1}}$, $0.32\,\mathrm{MeV\,u^{-1}}$ etc., but only to a lower degree at all other kinetic energies. Ions with kinetic energies of for example $2\,\mathrm{MeV\,u^{-1}}$, $0.5\,\mathrm{MeV\,u^{-1}}$ or $0.2\,\mathrm{MeV\,u^{-1}}$ leave the cavity with unchanged kinetic energies, no matter what the injection phase.

So far, only the ratios of the gap lengths have been taken into account, but other than that, they were assumed to be negligibly small. However, for the discussed ion velocities and the actual lengths, the time the ions need to traverse the gap are comparable to a significant change of the phase of the oscillating electric field. Accounting for this averaging effect with the so called transit time factor TT changes the effective gap voltage significantly, especially at lower ion velocities.

$$TT = \frac{\left|\int_{-L/2}^{L/2} E(0,z) \cdot \cos\left(\frac{2\pi \cdot z \cdot f_{cav}}{v_{ion}}\right) \mathrm{d}z\right|}{\int_{-L/2}^{L/2} |E(0,z)| \mathrm{d}z} \overset{E(0,z)=E_0}{=} \frac{v_{ion}}{\pi \cdot L \cdot f_{cav}} \cdot \left|\sin\left(\frac{\pi \cdot L \cdot f_{cav}}{v_{ion}}\right)\right| \tag{5.7}$$

L stands for the width of the gap and $E(0,z)$ and E_0 for the electric field in between this gap. The last part of equation 5.7 is valid, when $E(0,z)$ can be approximated to be constant across the whole gap. $U_{eff,transit}$ in figure 5.4 reflects the effect of including the transit time factor. Without the transit time factor the voltages at the individual gaps could cancel each other out. With the transit time factor, the voltages at the outer gaps are not reduced as much as the voltage in the central gap, since they are only half as wide. Thus the total applied voltage by the cavity can have the opposite effect of the voltage aimed for with a certain phase at the central gap ϕ_0. Overall, the design of the cavity severely limits the accessible ion energies for effective temporal bunch compression. The findings of the preceding sections about the generation and transport of laser-driven heavy ion beams suggest an operation of the beamline around $0.88\,\mathrm{MeV\,u^{-1}}$.

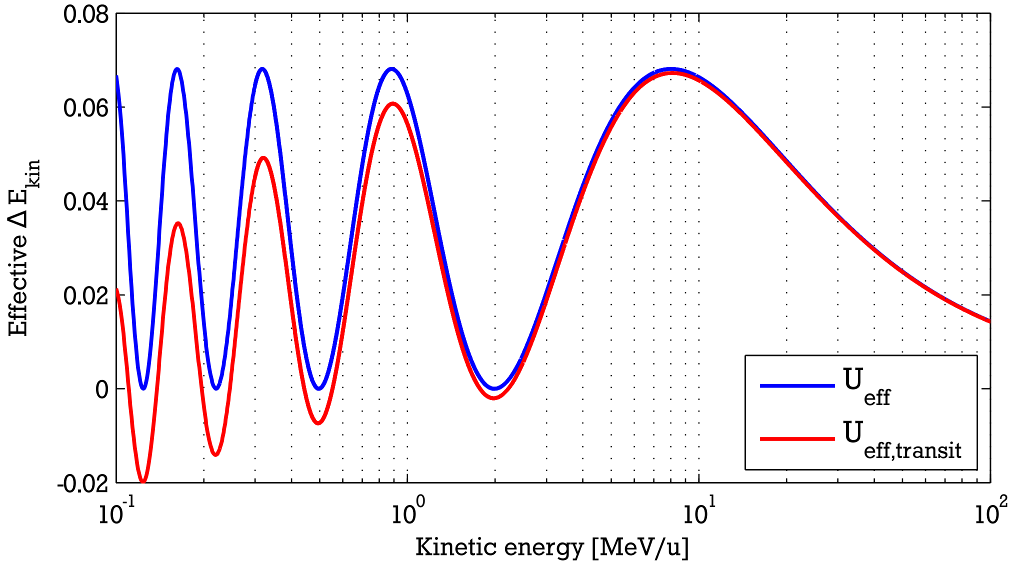

Figure 5.4: The effective gap voltage the ions are exposed to is strongly dependent on their velocity (U$_{eff}$). As the electric field oscillates with the frequency f_{cav}, only ions travelling from one center of the gap to the next in $t = \frac{L_{drift}+L_{gap}}{v_{ion}} = \frac{2n+1}{f_{cav}}$ reach each gap at the same phase. Differing ion velocities result in reduced gap voltages. Including the transit time factor changes the course of the total voltage U$_{eff,transit}$ as well, especially at the low velocity end of the diagram.

Another difference and possible problem of the lower velocity of the heavy ion bunch is that the velocity difference of head and tail of the ion bunch scales with the velocity of the center of gravity. The velocity difference of particles leading the ion bunch and particles at the back of it translates into a temporal length of the bunch with

$$\Delta t_{bunch} = \frac{s_{cav}}{v_{slow}} - \frac{s_{cav}}{v_{fast}} = \frac{2s_{cav}\Delta v}{v^2 - \Delta v^2}; \qquad v = \sqrt{1 - \frac{1}{(1+\frac{E_{kin}}{m_0 c^2})^2}} \cdot c, \tag{5.8}$$

where c denotes the vacuum speed of light, m_0 the rest mass of the ion, s_{cav} the distance from target to the middle of the cavity and $v_{slow,fast}$ the velocities of the particles in the back and front of the ion bunch and $\Delta v = (v_{fast} - v_{slow})/2$. Equation 5.8 neglects the longitudinal extent at the ion source, since it is in the picosecond regime. As long as the imaging properties of the solenoid do not change, the relative velocity spread of transported ions $\Delta v/v$ stays constant. Therefore the temporal length of the ion bunch scales with its average velocity. With the cavity sitting at $s_{cav} = 2.275\,\text{m}$, the FWHM longitudinal extent of the proton bunch at that position is $\Delta t_{bunch,protons} = 3.4\,\text{ns}$, whereas the C^{4+} ion bunch has diverged to a length of $\Delta t_{bunch,C^{4+}} = 8.2\,\text{ns}$. To achieve perfect longitudinal compression, the velocity distribution has to be reversed. The velocity difference has to be sufficient to compensate the temporal length of the bunch at the cavity position after a drift from cavity to the detector position.

$$\Delta t_{detector} = \frac{s_{tot} - s_{cav}}{v_{slow} + \Delta v} - \frac{s_{tot} - s_{cav}}{v_{fast} - \Delta v} + \Delta t_{bunch} \overset{!}{=} 0 \tag{5.9}$$

The total length of the beamline is denoted with s_{tot}. Equation 5.9 suggests that the velocity difference, induced by the injection of the ions into the cavity at −90° synchronous phase, has to be adjusted for successful phase focusing by tuning of the amplitude of the gap voltage. For given distances the kinetic energy gained by the ions can be described as

$$\Delta E_{kin} = q \cdot U_{eff} \cdot cos\left(\phi_s + \Delta t_s \cdot f_{cav} \cdot 2\pi\right) \approx q \cdot U_{eff} \cdot \Delta t_s \cdot f_{cav} \cdot 2\pi, \tag{5.10}$$

where Δt_s represents for the arrival time difference of ions at the cavity center with respect to the synchronous particle. The right part of equation 5.10 is only valid for injection of the synchronous particle into the cavity at $-90°$ synchronous phase and $\Delta t_s \cdot f_{cav} \ll 1$ (small-angle approximation). If the relative energy gain $\Delta E/E$ is small (below 10 %), the relation between the introduced energy difference and the resulting velocity difference can be linearised and the ion bunch can be compressed down to sub-nanosecond durations. A limiting factor is the longitudinal emittance, which leads to a blurring of the temporal focus. As the velocity difference of ions satisfying these conditions decreases with decreasing velocity of the synchronous particle (see equation 5.8), the gap voltage necessary for compression also decreases. Thus, the required gap voltage for maximum temporal bunch compression is considerably smaller in the case of heavy ion beams compared to the case of proton beams.

In contrast to the temporal compression of 7.8 MeV proton bunches, where the cavity was operated close to its maximum capability, the cavity has to be operated at comparably small input power for C^{4+} ions. This provides the opportunity for additional optimization. As the (rms) temporal length of the C^{4+} ion beam is in the order of the cavity period, only the central part of the beam can be focussed, because perfect focusing is only possible as long as the small-angle approximation is valid. A simple, yet effective measure to increase the number of ions close to $-90°$ synchronous phase injection is to move the cavity closer to the target. In that way the drift from target to cavity is decreased and thereby also the temporal length of the beam. At the same time also the required gap voltage increases, because the velocity difference scales inversely with the temporal difference.

Experimental constraints limit the minimum distance of target to cavity to 1.275 m, long before any limitations by the achievable gap voltages. Figure 5.5 displays the resulting change of the kinetic energy of C^{4+} ions ΔE_{eff} in case of a gap voltage U_1 of 0.05 MV. Assuming a constant slope of the gap voltage for a time window of 1.6 ns around the $-90°$ synchronous phase injection, $t_{ion} = t_s \pm 0.8$ ns, overestimates the actual gap voltage by a maximum of 5 % only. The extent of this time window can be translated into an kinetic energy range, which depends on the kinetic energy of the synchronous particle and the distance of the cavity to the target and is called bucket size. The translation of time window into kinetic energy range is only valid, because of the quasi-instantaneous generation and acceleration of the ions in the TNSA scheme.

Contrary to figure 5.3 in figure 5.5 only the linear regime is associated with the rf bucket and positions A and B denote a distance of 2.275 m and 1.275 m from target to cavity center respectively. The required alteration of the kinetic energy of the head and tail of the ions within a bucket to achieve optimal bunch compression at $z = 6.03$ m depends on the position of the cavity and the average velocity of the C^{4+} ion beam. The additional markers on the curves for the required change of kinetic energy denote an rf period of $\phi_0 = 0°$, that is repeated every 9.23 ns. TraceWin simulations demonstrate an increase in the number of ions in the central part of the beam by more than 50 % because of the increased bucket size, when comparing bunch compression with the cavity situated at 1.275 m or at the original position at 2.275 m [153].

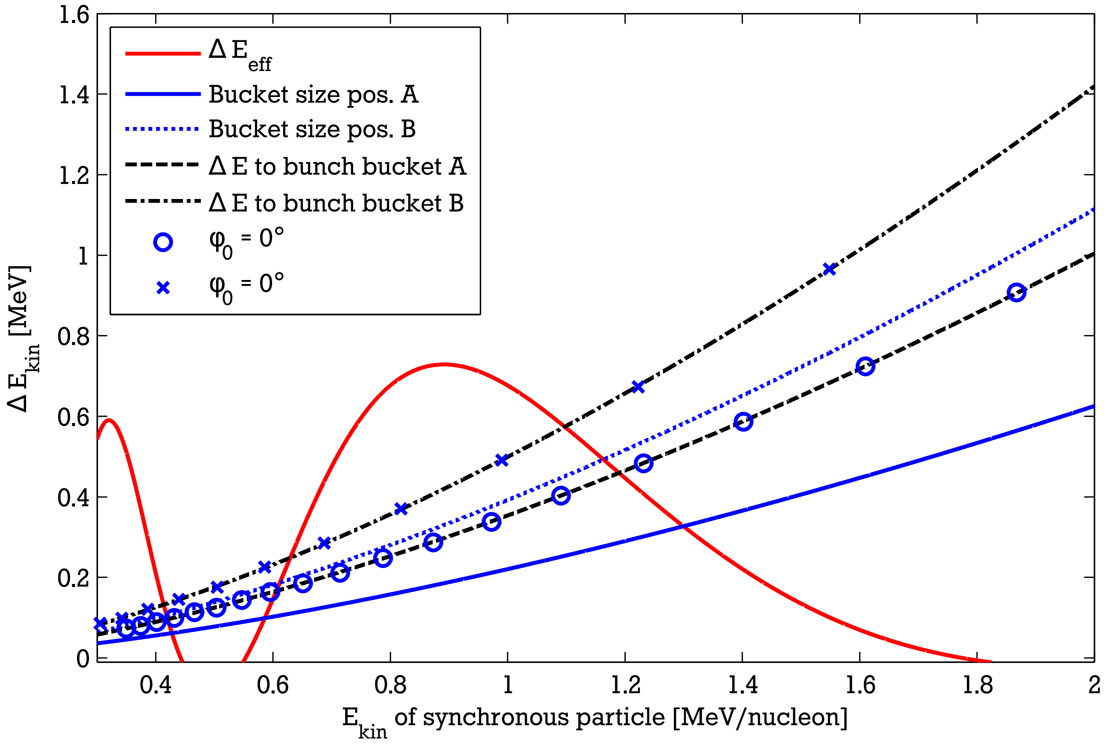

Figure 5.5: Showcasing of the dependence of the bucket size of the cavity on the cavity position: Ions arriving within a time frame of $1.6\,\mathrm{ns}$ at the cavity, either after a drift of $2.275\,\mathrm{m}$ (position A) or $1.275\,\mathrm{m}$ (position B), define the energy range of a bucket. The kinetic energy necessary to achieve maximum temporal compression at $6.03\,\mathrm{m}$ distance from the target is considerably larger than the bucket size in order to reverse the longitudinal divergence the beam accumulated while propagating from target to cavity. Also displayed is the effective change of the kinetic energy of C^{4+} ions passing through the cavity for a gap voltage $U_{outer} = 0.05\,\mathrm{MeV}$.

All findings in this paragraph support an optimum average kinetic energy of the transported C^{4+} ion beam of $0.88\,\mathrm{MeV\,u^{-1}}$. However, the required rf power input is then too low for the cavity to autonomously find and maintain the resonance condition. The plunger is connected to the standing waves in the cavity via feedbacks and in the case of small amplitudes, this self-regulation technique is not working. This is the reason, why the average energy of the C^{4+} ion beam from the previous chapter is set to neither $1\,\mathrm{MeV\,u^{-1}}$ nor $0.88\,\mathrm{MeV\,u^{-1}}$ but to $1.22\,\mathrm{MeV\,u^{-1}}$.

5.2.1 Beam dynamic simulations of temporal focusing

In order to narrow down the quite extensive parameter space, consisting of the independent parameters injection phase ϕ_s at amplitude of the gap voltage U_0 and solenoid current for the transport of the ions, it is essential to conduct simulation studies. The cavity was emulated as three gaps, separated by the distances from gap center to gap center (see table 5.1). The applied voltage at each gap oscillates with the rf period $f_{cav} = 108.4\,\mathrm{MHz}$ with a phase difference of π between each gap. The phase relation of the cavity phase to the synchronous particle is absolute at each gap, thus taking the phase advance of the ions in the drift between the gaps into account. Additionally a transit time factor has been introduced for each gap, approximating the finite gap length, which was already incorporated in the calculations concerning the effective gap voltage in the previous section (equation 5.7).

Simulation studies were utilized to determine the correct phase and oscillation amplitude for the cavity in order to achieve a pulse compression for a given average energy of the ion pulse. The simulations expanded on the setup of the transport simulations by adding the gaps in the above described way. Figure 5.6 displays the time and energy relation of C^{4+} ions at different positions. The ion beam was collimated with a solenoid driven with a current $I_{solenoid} = 8.92\,\text{kA}$ and with the determined astigmatism before arriving at the first gap (figure 5.6 a)). After crossing the whole cavity, the energy-time relation is altered considerably. Figure 5.6 b) displays the reversal of the velocities of head and tail ions close to $-90°$ phase after all three gaps. This reversal can also be described as a rotation in the energy-time plane. The angle of rotation then describes the slope of the small-angle approximation of the oscillating electric field. While drifting from the cavity exit to the monitor at 6.03 m distance from the target, the temporal bunch length is decreasing as the ions in the back of the beam start to overtake the decelerated particles at the head of the beam. If oscillation phase and amplitude of the cavity are chosen according to the energy of the transported ions, a significant part of the ion beam can be compressed down to subnanosecond FHWM temporal lengths at the position of the monitor (see figure 5.6 c)). After this focal point, the ion beam starts to diverge again.

Simulation results, published in [153], show an increase of particle numbers in the central part of the compressed bunch of 50 % in the case of the cavity center being positioned at a distance of 1.275 m compared to a distance of 2.275 m from the target (in this case for C^{4+} ions

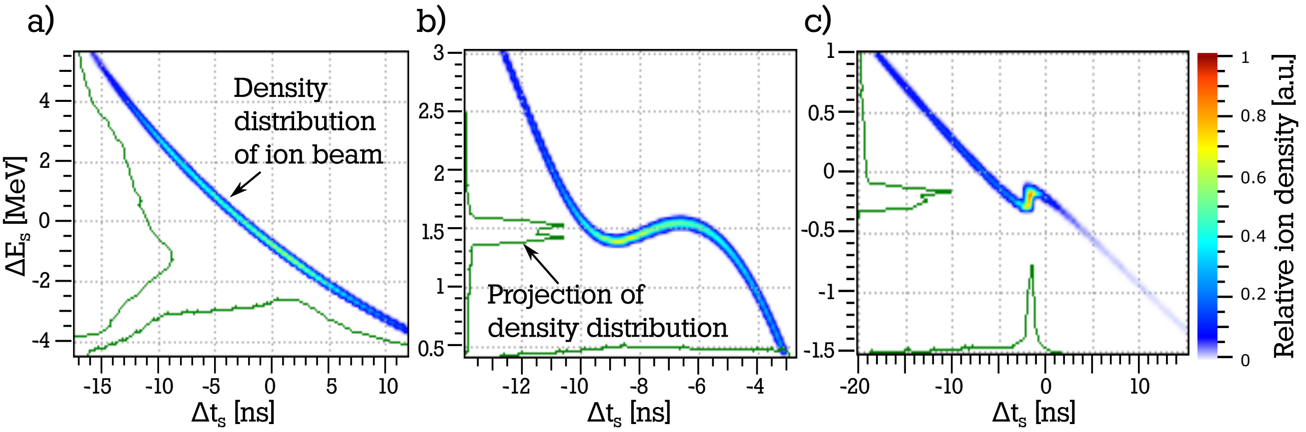

Figure 5.6: Bunch compression of laser-driven C^{4+} ions in simulations:

a) Ion beam directly before entering the first gap. The energy over time relation of the ions is proportional to t^{-2}. Both energy and time are defined relative to the synchronous particle.

b) After passing through all three gaps, the energy time relation is altered. The energy time relation close to relative times corresponding to $-90°$ injection has been reversed and these parts exhibit a constant positive slope. This positive slope indicates, that particles in the back of the beam are faster than particle at the front.

c) Thus, after sufficient drift, here at the end of the beamline, the ion bunch compression is at a maximum resulting in subnanosecond bunches.

transported with an average energy of 1 MeV u^{-1}). Another direct result was a decline of the number of satellite peaks, which are caused by the remote parts on both sides of the central part of the ion beam being focussed in adjacent buckets. These simulations also suggested, that the minimum achievable FWHM bunch length is connected to the distance of cavity to focal point of the phase focus; the smaller this distance, the lower the minimum achievable FWHM bunch length, similar to optics. In the simulations the achievable FWHM bunch lengths went from 0.2 ns to 0.3 ns. That is another 50 % increase, just as in the case of the ion number in the central part of the peak. The increased bunch length is still more than sufficiently short for future applications and the increase in ion numbers and decrease in satellite peaks is well worth the effort.

Another interesting finding is, that even though the changes of the kinetic energies of the ions introduced by the cavity are relatively small compared to the average kinetic energy of the ion beam (below 10 %), the acceleration and deceleration of the ions in the cavity has a significant impact on the transversal phase space of the ions, since transversal momentum is not changed by the cavity. This effect can be seen already, when comparing the transport efficiencies for active and inactive cavity. For phase and oscillation amplitude as in the simulation depicted in figure 5.6 the number of transmitted ions went up by about 11 % in case of the active cavity.

5.3 Experimental realization

In the preceding sections the advantages of moving the cavity closer to target have been worked out. Nevertheless the option to operate the cavity at its original position should be preserved as long as the option to temporally compress proton beams with an average kinetic energy of around 8 MeV is relevant. Additionally, any changes in the setup must not be time consuming so as not to lose any precious beam time in the process. These requirements are met by putting the cavity on a sledge, displayed in the CAD drawing in figure 5.7 a) and the photograph in 5.7 b), which allows for one degree of freedom parallel to the beam axis. In this way the position of the cavity can be chosen arbitrarily between position A, center of the cavity at 1.275 m, and position B, center of the cavity at 2.275 m. As the waveguide required to supply rf power to the cavity is very rigid, waveguides have to be matched to each position.

Exact control of the timing of each component is even more critical than in the case of pure ion transport. As the maximum compression is highly sensitive to the phase of ion injection into the cavity, any uncertainties of the time difference of the PHELIX laser impinging on the target and the phase in the cavity directly worsen the minimum achievable bunch lengths.

5.4 First experimental results for bunch compression

First results for the temporal compression of laser-driven heavy ion beams were gathered during several experimental campaigns within the scope of this thesis. During a campaign in 2016 laser-driven fluorine ion beams, characterized in chapter 3, were transported and the first attempts at temporal compression were made. The diamond detector, described in section 4.4, was utilized to examine the temporal structure of the ion beam. The cavity mounting had not been modified to permit a closer cavity position, thus the cavity setup designed for protons was used (cavity center at 2.275 m). After collimating the ion beam with the solenoid operated at a solenoid current of 8.32 kA, it passed through the cavity, which was operated at an

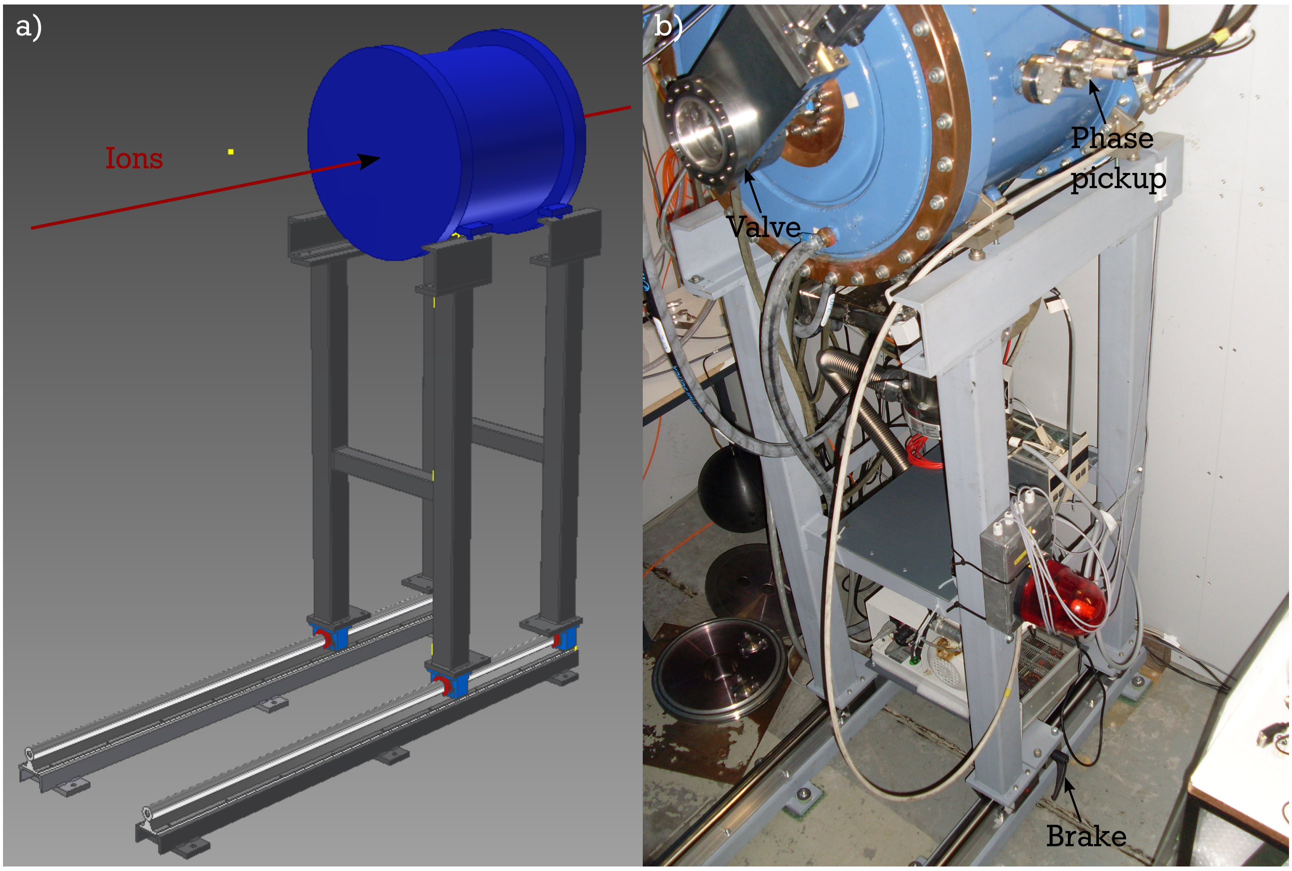

Figure 5.7: a) CAD drawing of the cavity on a sledge. The linear guidance allows for an arbitrary choice of position parallel to the beam axis.
b) As long as the beamline is not connected to the cavity, simply opening a brake makes it possible to adjust the position of the cavity in a matter of minutes.

input power of 13.2 kW (equalling a maximum gap voltage at one of the outer gaps of 91 kV). As the experiment had to be reassembled, the timing reference from previous campaigns regarding the relation between cavity phase and laser impact on the target was not valid any more. Thus, the starting phase was chosen arbitrarily, resulting in the ToF data, which was recorded at a distance of 6.03 m to the target and is depicted in figure 5.8. In addition to two main peaks around 386 ns there are a lot of satellite peaks, where the leading and trailing parts of the ion beams were compressed. The peaks can be identified to be caused by F^{7+}, F^{6+} and F^{5+} ion beams, separated in energy because of the q^2/m^2 scaling of the focal length of the solenoid. The double peak at 386 ns originates from an overcompensation of the velocity difference of head and tail. Therefore the position of maximum compression is somewhere in between cavity and detector and from there on the beam starts to diverge again longitudinally (also depicted in the top left part of figure 5.8). The steeper of the two peaks exhibits a FWHM duration of (1.3 ± 0.1) ns. At an average beam energy of 1.30 MeV u^{-1} of the F^{7+} ion beam the total efficient gap voltage of the cavity is strongly correlated with the beam energy (see figure 5.4). That makes finding the ideal pair of rf power and corresponding phase very difficult. Limitations to the test time in this campaign only allowed for this proof of principle of temporal compression. During the latest experimental campaign in September 2017, after characterizing the transported C^{4+} ions (see section 4), a number of shots were dedicated to examining the

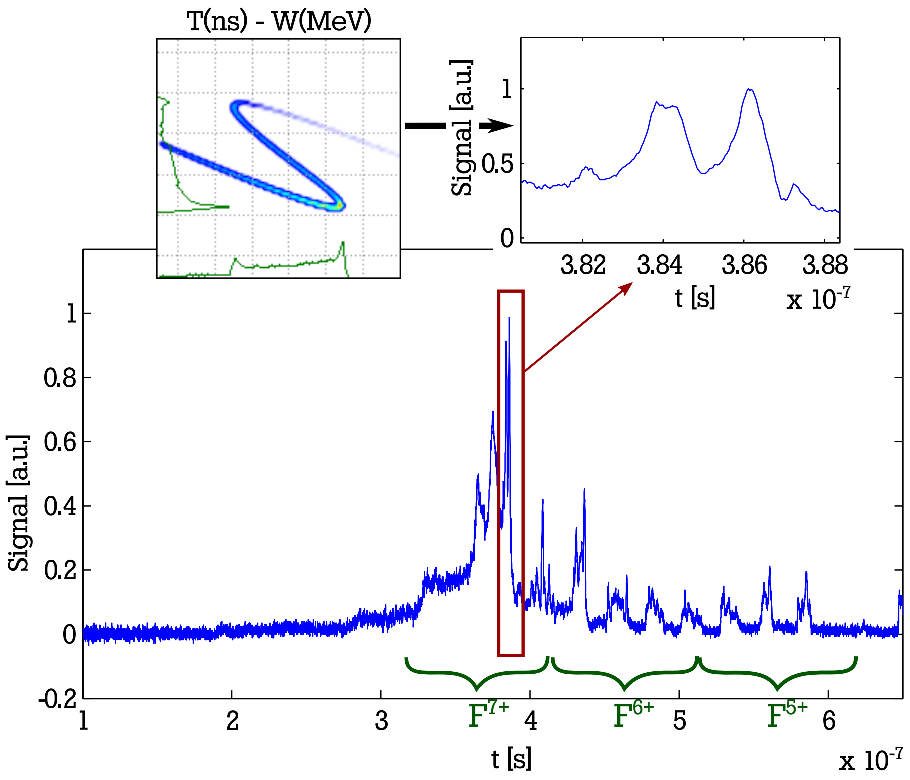

Figure 5.8: ToF data of temporally compressed fluorine ion beam. The best attempt at compressing the beam is a double peak at 386 ns, zoomed in on in the upper right part of the figure. This sort of double peak is created, when the velocity difference of head and tail of one bucket is overcompensated, resulting in a point of maximum temporal compression before reaching the detector position and subsequent divergence.

temporal compression capabilities of the LIGHT beamline with the altered cavity position (distance to target of 1.275 m). To achieve maximum compression at the position of the diamond detector, simulations were carried out to find the necessary gap voltage and corresponding phase. The absolute timing reference with respect to the laser impinging on the target for this new position of the cavity is not known with precision, because already an uncertainty of 0.01 m in the positioning leads to a ToF uncertainty of 0.65 ns, which translates into a phase of 25°. Thus, an arbitrary starting point of the phase is chosen in order to infer possible phase changes from the resulting signal at the diamond detector.

Shots 41 to 44 were all carried out with a gap voltage of an outer gap of 66 kV but with ϕ_1, $\phi_2 = \phi_1 + 97°$, $\phi_3 = \phi_1 + 214°$ and $\phi_4 = \phi_1 + 292°$ for shots 41, 42, 43 and 44 respectively. Because of the above stated reason, ϕ_1 and therefore none of the phases are known absolutely, only relative to each other. The ToF data, recorded with a diamond detector at a distance of 6.03 m to the target, is displayed in figure 5.9. In none of the shots could a temporal compression be detected. The change of the temporal signal with different phases is quite puzzling even though the injection phases are not known. From previous campaigns and simulations it is expected, that the maximum distance between the same feature at different input phases equals

$$\Delta t_{max} = \frac{s_2}{s_1} \cdot \frac{1}{f_{cav}} = 43.6\,\text{ns}, \tag{5.11}$$

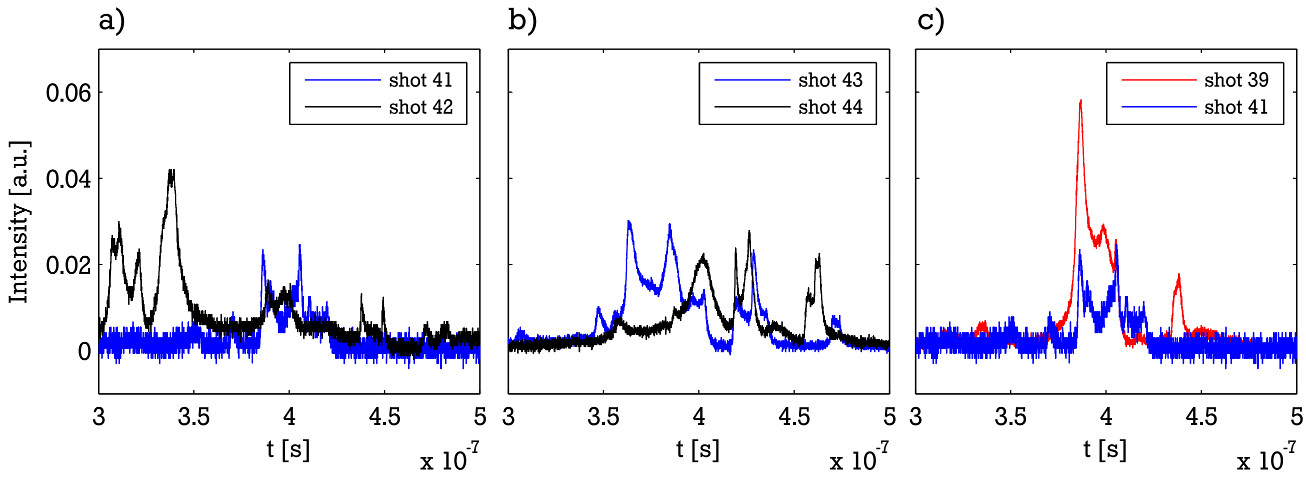

Figure 5.9: ToF data of shots with active cavity at $U_{outer} = 66\,\mathrm{kV}$ and different timings:
a) Shots 41 and 42; shot 41 at ϕ_1 and shot 42 at $\phi_1 + 97°$. Instead of temporal compression the ion beam was shifted and broadened.
b) Shots 43 and 44; shot 43 at ϕ_1+214° and shot 44 at ϕ_1+292°. Instead of temporal compression the ion beam was shifted and broadened.
c) Comparing the ToF data of shot 41 with shot 39, which was recorded for inactive cavity, suggests that reducing the rf input power at the same phase might have lead to a reduced bunch length.

where s_1 is the distance from target to cavity and s_2 the distance from cavity to detector. In the ToF data this shift exceeds this limit considerably.

Taking into account the small detection area of the diamond detector and the dependency of detected ion properties on the transversal position of the detector (demonstrated in section 4.5) could serve as a possible explanation for the seemingly chaotic change of the temporal structure of the beam with respect to the cavity phase. A perfectly aligned solenoid, even considering the quadrupole moment caused by the astigmatism, combined with an active cavity results in a dependence of the beam profile in x-y-space on the injection phase, also displayed in figure 5.10 for C^{4+} ions with the parameters from shots 41 to 44. However, a cut-out of the middle of the

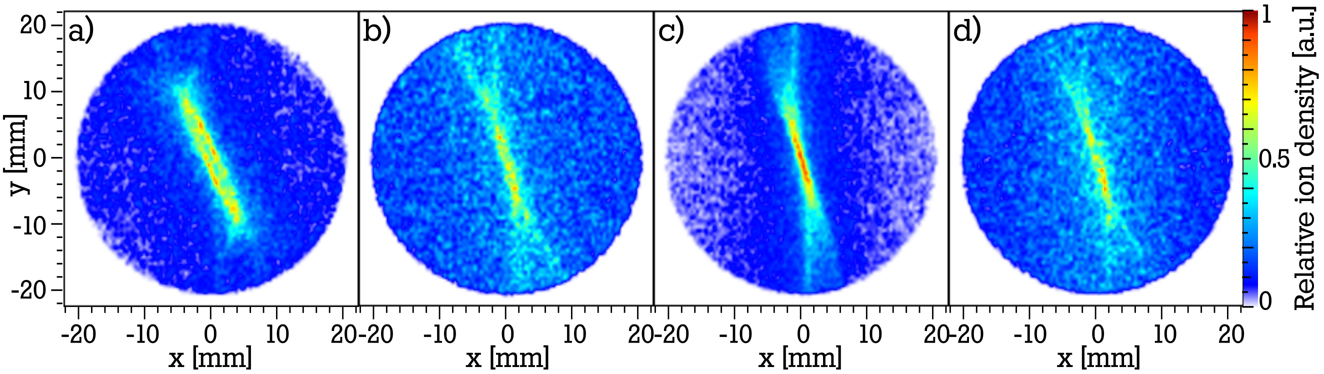

Figure 5.10: Simulated transversal beam profiles of C^{4+} ion beams at the end of the LIGHT beamline. The collimation solenoid was assumed to be perfectly aligned and the injection phases into the active cavity varied: a) injection phase of ϕ_1, b) injection phase of $\phi_1 + 97°$, c) injection phase of $\phi_1 + 214°$, d) injection phase of $\phi_1 + 292°$

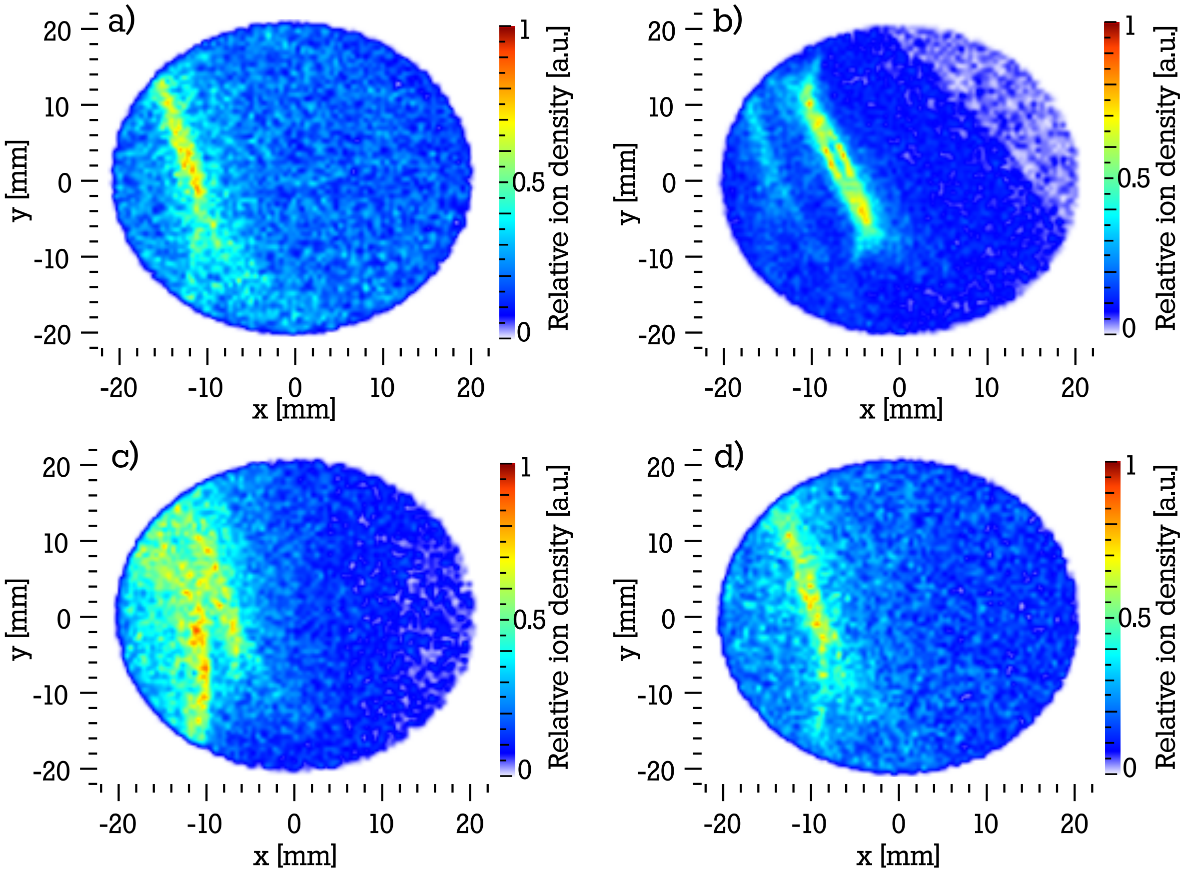

Figure 5.11: Simulated transversal beam profiles of C^{4+} ion beams at the end of the LIGHT beamline. The collimation solenoid was tilted by 0.15° and the injection phases into the active cavity varied: a) injection phase of ϕ_1, b) injection phase of ϕ_2, c) injection phase of ϕ_3, d) injection phase of ϕ_4

x-y-beam profile still represents the overall temporal structure of the complete beam reasonably well and does not exhibit the same tendencies as the ToF data of shots 41 to 44 with respect to the injection phase (see figure 5.12 a)).

By adding a shift and tilt to the solenoid field, a possible misalignment can be emulated. Figure 5.11 shows the beam profiles for misalignments similar to the ones in section 4.5. While the simulated temporal structure of the total beam is not altered significantly, the interplay of the cavity acting on the transversal phase space because of acceleration and deceleration and the altered imaging of the misaligned ion optic creates a very complicated temporal structure dependency on the phase for sub-monitors. In figure 5.12 a) the ToF outcome of a central 4 x 4 mm^2 sub-monitor at the end of the beamline for simulations emulating shots 41 to 44 is depicted. In comparison to that the temporal outcome of the same simulation with an added tilt of 0.15° in 5.12 b) show a bigger spread of the resulting peaks. On top of that there is a big difference between the temporal structures in the case of a tilt or without tilt at each input phase. Taken together this indicates a more complicated underlying relation between the injection phase and the imaging properties of the complete LIGHT beamline. Due to the unknown phase ϕ_1, exact misalignment of the solenoid and its astigmatism, it was impossible to recreate the temporal structures of shots 41 to 44 in simulations. So far only the tendencies of the time structure with varying phase have been demonstrated, but neither in the observed magnitude nor the same structure. Still the misalignment of the solenoid is the most likely cause of the time structures of shots 41 to 44.

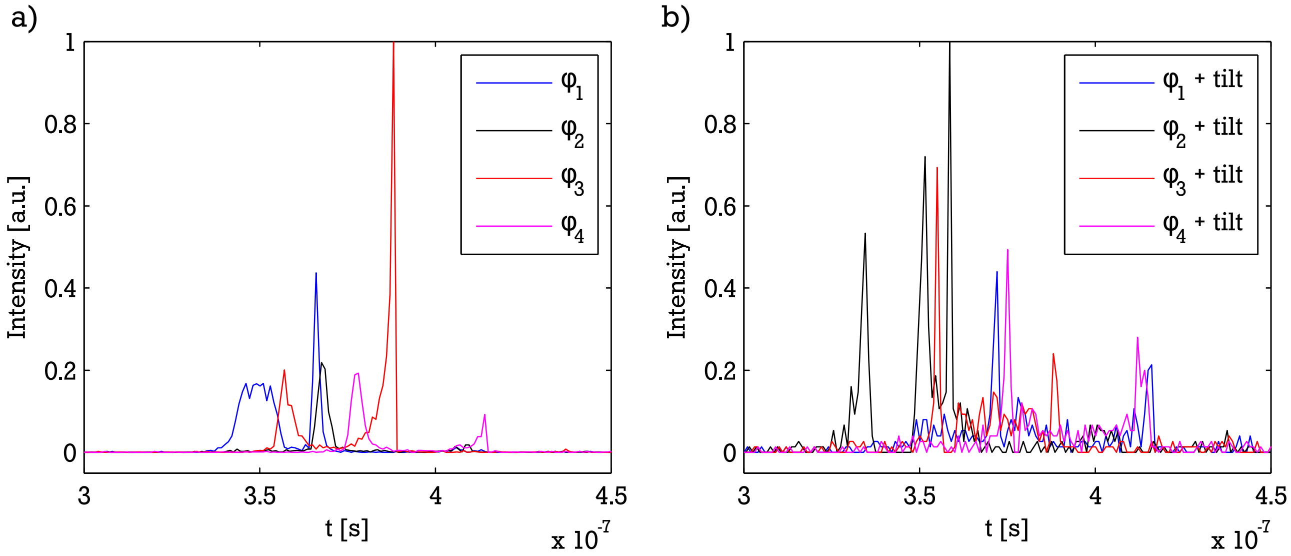

Figure 5.12: Simulated temporal distribution of C^{4+} ions at a central sub-monitor at the end of the LIGHT beamline. The results in a) were gained by simulating with a perfectly aligned solenoid and cavity and solenoid parameters as in shots 41-44. Whereas the temporal distributions in b) result from the same parameters as a), but with an added tilt of the solenoid.

5.5 Results of bunch compression

The analysis of temporal bunch compression of laser-driven heavy ion beams with a three gap spiral resonator, which is designed for ions with kinetic energies of $8\,\mathrm{MeV\,u^{-1}}$, has highlighted certain challenges. Most importantly there are requirements on the ion energy, because of the dependency of the effectively introduced change in kinetic energy of the heavy ions over all three gaps on their velocity. Operating the LIGHT beamline with C^{4+} ions with kinetic energies close to $0.88\,\mathrm{MeV\,u^{-1}}$ would match these requirements perfectly, as $8\,\mathrm{MeV\,u^{-1}}$ are neither generated by the source, nor could they be transported by the present solenoid. However, the optimum field amplitude of the standing wave in the resonator to achieve maximum bunch compression at the end of the LIGHT beamline is then too low for the self-regulating resonance control, which relies on the feedback from the standing wave, to ensure reliable operation of the cavity. In order to have a stable cavity control the collimation solenoid has to be operated at currents that enable the transport of C^{4+} with kinetic energies above $1.2\,\mathrm{MeV\,u^{-1}}$.

In order to increase the number of ions, which can fit in the linear regime of the rf bucket, it was proposed to install the cavity as close to the target as possible. Moving the cavity one meter closer results in 50 % more particles in the FWHM of the compressed bunch, at least in simulations.

In a first attempt at temporal bunch compression of laser-driven fluorine ion beams the proof-of-principle could be demonstrated for the cavity being situated at the farther position. The resulting multitude of bunches, caused by ions getting bunched into adjacent rf buckets, could not be compressed below $(1.3 \pm 0.1)\,\mathrm{ns}$.

In the most recent experimental campaign with laser driven carbon ion beams the cavity was operated one meter closer to the target. The results for the variation of the injection phase into the cavity were rather puzzling, because the ensuing temporal structure, recorded with a diamond detector, did not match the simulations for the complete beam at all. The best explanation so far is that the small detection area of the diamond detector in combination with small changes to the imaging properties of the LIGHT beamline by the injection phase dependent acceleration and deceleration of the ions in the cavity leads to the observed behaviour. Simulations support this theory, because they show a significant change of the transversal beam profile with variations of the injection phase. Resolving the alignment issues of the collimating solenoid will enable a more successful bunch compression of laser-driven heavy ion beams.

6 Conclusion and outlook

Within the scope of this doctoral thesis, several milestones on the way to a successful application of laser-driven heavy ion beams have been accomplished.

Firstly the efficient acceleration of fluorine and carbon ions by means of target normal sheath acceleration (TNSA) has been demonstrated. Fourfold positively charged carbon ions have been accelerated reliably to kinetic energies of up to $68.5^{+4.8}_{-4.3}\,\mathrm{MeV}$ and sevenfold positively charged fluorine ions have even reached kinetic energies of up to $180^{+32}_{-26}\,\mathrm{MeV}$. In the process of characterizing the divergence distribution of laser-driven carbon ions with a set of three Thomson parabolas or enhanced radiochromic imaging spectroscopy (RIS) it could be proven that the divergence of the heavy ion beams is quite different from typical laser-driven proton beams. Instead of a quadratic decrease of the maximum divergence and a Gaussian or quadratic distribution of divergences at a given ion energy, the findings from the use of three Thomson parabolas simultaneously at three different angles with respect to the TNSA direction as well as the enhanced RIS suggest a ring-like transverse beam profile for higher ion energies. For lower energies, up to 20 MeV in the case of C^{4+} ions, the divergence distribution of the carbon ion beam is very similar to the divergence distribution of a proton beam.

Literature research has not yielded any satisfactory explanation for the ring-like structures, which have been recorded with radiochromic films. Similar structures have only been observed for very thin targets and the underlying theories are thus not applicable to the the present case. Further investigations, supported by particle in cell (PIC) simulations, are necessary to find possible explanations.

Secondly the transport of laser-driven carbon and fluorine ion beams was successfully demonstrated. A detailed investigation of the energy spectrum and particle numbers of the ion beam at the end of the *laser ion generation, handling and transport* (LIGHT) beamline has only been undertaken for carbon ions, which are also the ion species most likely to be used in the anticipated stopping power measurements. The small detection areas of Thomson parabola and diamond detector made it necessary to use simulations for the characterization of the whole beam. By matching the simulations to the observed energy spectra, the ion beam characteristics could be deduced from simulations. A total number of $9.9^{+2.7}_{-3.1}\cdot 10^{8}$ C^{4+} ions at an average energy of $(14.9 \pm 0.1)\,\mathrm{MeV}$ were transported to the detection area at 6.03 m distance to the target. The ions occupied a transverse beam area of $12.6\,\mathrm{cm}^2$ and $6.2^{+1.7}_{-1.9}\cdot 10^{8}$ of the $9.9^{+2.7}_{-3.1}\cdot 10^{8}$ ions have energies in the full width half maximum (FWHM) energy range from $(14.0 \pm 0.1)\,\mathrm{MeV}$ to $(15.8 \pm 0.1)\,\mathrm{MeV}$. Resolving the alignment issues from the latest experimental campaign will lead to an overall increase in ion numbers.

Lastly, the temporal bunch compression of laser-driven heavy ion beams has also been addressed within the scope of this work. The analysis of the capability of the three gap radiofrequency spiral resonator (rf cavity) with regard to phase focusing of heavy ion beams with a velocity much below the design velocity of the resonator, led to the design and assembly of a movable mounting bracket for the resonator. Thus, for the bunch compression of protons the resonator can be utilized in its original configuration and for the bunch compression of heavy ions the resonator can be moved closer to the target to capture more ions in the linear regime of the rf bucket. Bunch compression of heavy ions has not been optimized and so far only bunch lengths of (1.3 ± 0.1) ns (FWHM) have been demonstrated in the case of fluorine ions. The complicated interplay between the injection phase into the resonator, the subsequent acceleration or deceleration of the ions, and the consequent change of the imaging of the beamline, together with the misalignment of the solenoid led to a very challenging problem to optimize the bunch compression. Future experimental campaigns should be able to resolve these issues and use the LIGHT beamline with a movable rf cavity for possible applications.

In the near future an additional transversal focusing of the heavy ion beam at the end of the beamline will also be demonstrated. The second solenoid, so far only relevant because of its limitation of the free aperture at the end of the beamline, will be used to focus the beam to small spots shortly after the solenoid. Figure 6.1 shows a TraceWin simulation of a temporally compressed bunch of C^{4+} ions, 10 cm behind the second solenoid, with a FWHM spot diameter below 1.5 mm. As soon as the temporal, as well as the transversal bunch compression at the end of the LIGHT beamline are established, the first energy loss measurements of heavy ions in dense plasmas will be able to be conducted. Preparatory work to supply a laser pulse of sufficient intensity and energy for plasma generation at the end of the LIGHT beamline are already under way.

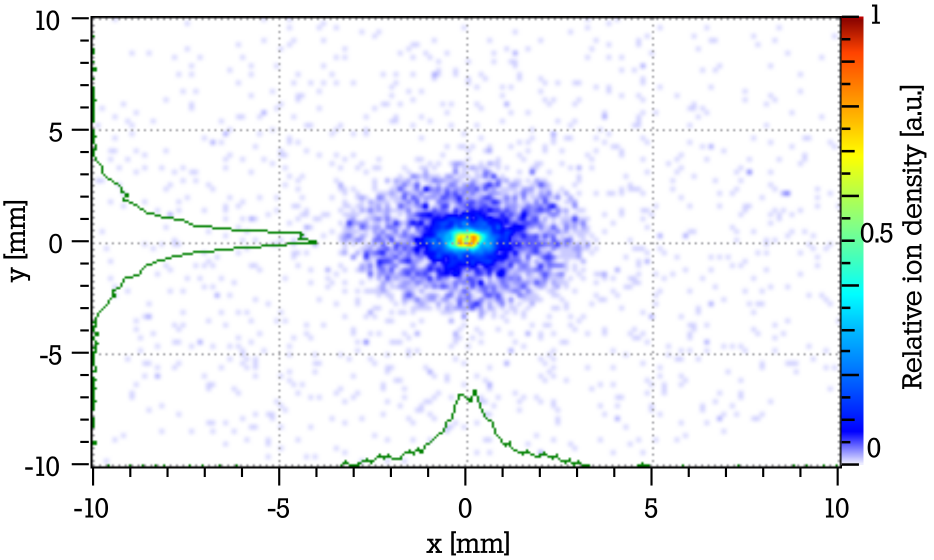

Figure 6.1: Simulated transversal beam profile of a longitudinally and transversally compressed C^{4+} ion bunch

In the medium-term a new dedicated LIGHT beamline will be established, which will eliminate the need to reassemble the target and ion optics in the beamline at the beginning of each experimental campaign. Hence one of the biggest challenges will be able to be dealt with once and for all. Within the recently approved Helmholtz accelerator research and development program ATHENA [168], the LIGHT collaboration will receive funding for a dedicated LIGHT target chamber and the infrastructure for the rf input power supply for two rf cavities, identical to the one already incorporated into the original beamline. Utilizing two rf cavities allows for an energy compression of the ion bunch shortly after the collimating solenoid and a subsequent phase focusing close to the interaction point, leading to the shortest bunch durations.

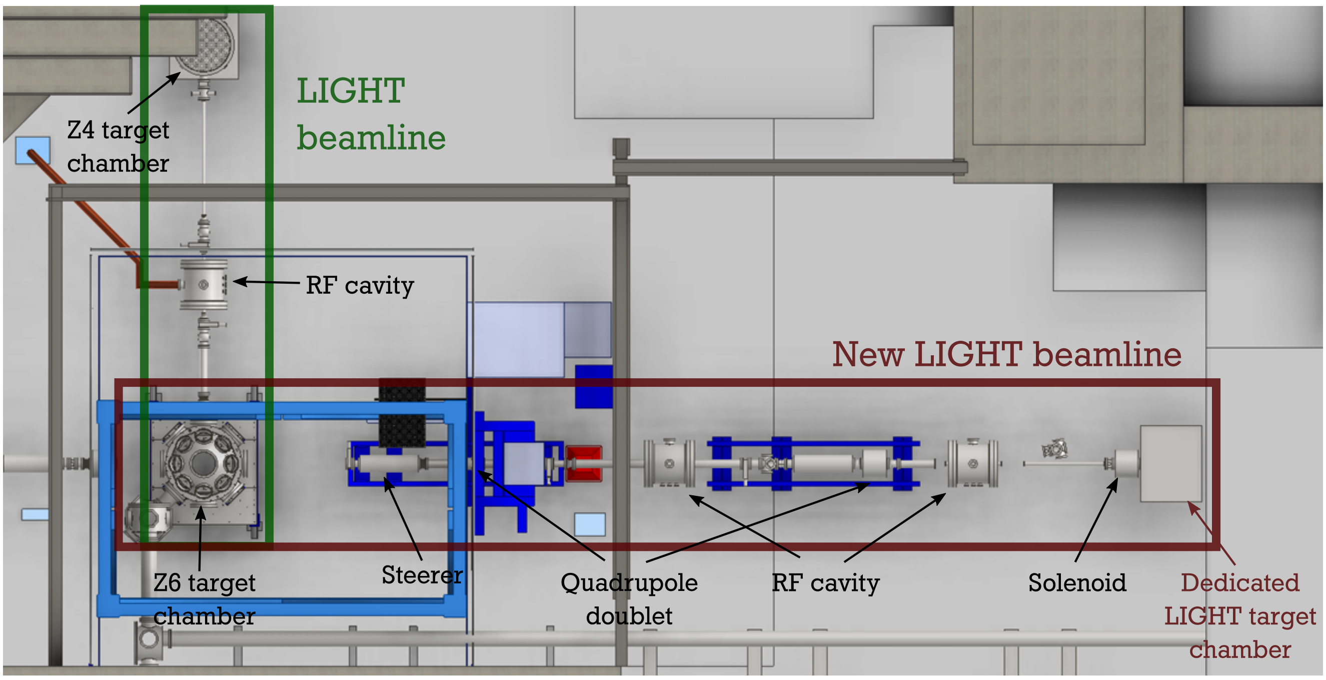

Figure 6.2: CAD drawing of the current and future LIGHT beamline (courtesy of D. Schumacher). The new beamline will end in the Z6 target chamber.

A schematic drawing of the new beamline is depicted in figure 6.2. By changing the course of the beamline to the present Z6 ion beamline and putting the laser-driven source at the current end of the beamline into a dedicated target chamber, future experiments can use the LIGHT beamline to produce an ion probe beam for experiments in the Z6 target chamber using the nhelix laser. This enables the use of additional diagnostics, which are available at the Z6 target chamber, such as a *velocity interferometer system for any reflector* or time-resolved plasma shadowgraphy. Facilities presently installed in the Z6 ion beamline will aid the process of improving the transport efficiency of laser-driven ion beams. Optimization of the alignment of the ion optics to currently unattainable precision will be feasible in future by utilizing an ion beam from the *universal linear accelerator* (UNILAC) at GSI and optimizing the throughput in the reverse direction, from the Z6 target chamber to the dedicated LIGHT target chamber.

List of abbreviations

BoA	breakout-afterburner
BSI	barrier supression ionization
CI	collisional ionization
CPA	chirped pulse amplification
CR39	California raisin 39
ELI	extreme light infrastructure
EMP	electro-magnetic pulse
FAIR	facility for antiproton and ion research
FWHM	full width half maximum
GSI	GSI Helmholtz-center for heavy ion research
HZDR	Helmholtz-centre Dresden-Rossendorf
IP	image plate
LIGHT	laser ion generation, handling and transport
MPI	multiphoton ionization
PHELIX	petawatt high-energy laser for heavy ion experiments
PIC	particle in cell
PSL	photo stimulated luminescence
PTC	positive temperature coefficient of resistance
RCF	radiodochromic film
rf	radiofrequency
rf cavity	three gap spiral radiofrequency cavity resonator
RIS	radiochromic imaging spectroscopy
RIT	radiation induced transparency
RPA	radiation pressure acceleration
TNSA	target normal sheath acceleration
ToF	time of flight
TP	Thomson parabola
UNILAC	universal linear accelerator

References

[1] T. H. MAIMAN. Stimulated optical radiation in ruby. *Nature*, 187:493 EP –, Aug 1960.

[2] F. J. McClung and R. W. Hellwarth. Giant optical pulsations from ruby. *Journal of Applied Physics*, 33(3):828–829, 1962.

[3] L. E. Hargrove, R. L. Fork, and M. A. Pollack. Locking of he-ne laser modes induced by synchronous intracavity modulation. *Applied Physics Letters*, 5(1):4–5, 1964.

[4] Donna Strickland and Gerard Mourou. Compression of amplified chirped optical pulses. *Optics Communications*, 55(6):447 – 449, 1985.

[5] C.N. Danson, P.A. Brummitt, R.J. Clarke, J.L. Collier, B. Fell, A.J. Frackiewicz, S. Hawkes, C. Hernandez-Gomez, P. Holligan, M.H.R. Hutchinson, and et al. Vulcan petawatt: Design, operation and interactions at $5 \cdot 10^{20}$ w/cm^2. *Laser and Particle Beams*, 23(1):87–93, 2005.

[6] S. H. Batha, R. Aragonez, F. L. Archuleta, T. N. Archuleta, J. F. Benage, J. A. Cobble, J. S. Cowan, V. E. Fatherley, K. A. Flippo, D. C. Gautier, R. P. Gonzales, S. R. Greenfield, B. M. Hegelich, T. R. Hurry, R. P. Johnson, J. L. Kline, S. A. Letzring, E. N. Loomis, F. E. Lopez, S. N. Luo, D. S. Montgomery, J. A. Oertel, D. L. Paisley, S. M. Reid, P. G. Sanchez, A. Seifter, T. Shimada, and J. B. Workman. Trident high-energy-density facility experimental capabilities and diagnostics. *Review of Scientific Instruments*, 79(10):10F305, 2008.

[7] V. Bagnoud, B. Aurand, A. Blazevic, S. Borneis, C. Bruske, B. Ecker, U. Eisenbarth, J. Fils, A. Frank, E. Gaul, S. Goette, C. Haefner, T. Hahn, K. Harres, H.-M. Heuck, D. Hochhaus, D. H. H. Hoffmann, D. Javorková, H.-J. Kluge, T. Kuehl, S. Kunzer, M. Kreutz, T. Merz-Mantwill, P. Neumayer, E. Onkels, D. Reemts, O. Rosmej, M. Roth, T. Stoehlker, A. Tauschwitz, B. Zielbauer, D. Zimmer, and K. Witte. Commissioning and early experiments of the phelix facility. *Applied Physics B*, 100(1):137–150, Jul 2010.

[8] Extreme light. *Nature Materials*, 15:1 EP –, Dec 2015. Editorial.

[9] A. Macchi. *A Superintense Laser-Plasma Interaction Theory Primer*. Springer, 2013.

[10] B. Dromey, M. Zepf, A. Gopal, K. Lancaster, M. S. Wei, K. Krushelnick, M. Tatarakis, N. Vakakis, S. Moustaizis, R. Kodama, M. Tampo, C. Stoeckl, R. Clarke, H. Habara, D. Neely, S. Karsch, and P. Norreys. High harmonic generation in the relativistic limit. *Nature Physics*, 2:456 EP –, Jul 2006.

[11] Antoine Rousse, Kim Ta Phuoc, Rahul Shah, Alexander Pukhov, Eric Lefebvre, Victor Malka, Sergey Kiselev, Fréderic Burgy, Jean-Philippe Rousseau, Donald Umstadter, and Daniéle Hulin. Production of a kev x-ray beam from synchrotron radiation in relativistic laser-plasma interaction. *Phys. Rev. Lett.*, 93:135005, Sep 2004.

[12] V. Malka, S. Fritzler, E. Lefebvre, M.-M. Aleonard, F. Burgy, J.-P. Chambaret, J.-F. Chemin, K. Krushelnick, G. Malka, S. P. D. Mangles, Z. Najmudin, M. Pittman, J.-P. Rousseau, J.-N. Scheurer, B. Walton, and A. E. Dangor. Electron acceleration by a wake field forced by an intense ultrashort laser pulse. *Science*, 298(5598):1596–1600, 2002.

[13] S. Steinke, J. van Tilborg, C. Benedetti, C. G. R. Geddes, C. B. Schroeder, J. Daniels, K. K. Swanson, A. J. Gonsalves, K. Nakamura, N. H. Matlis, B. H. Shaw, E. Esarey, and W. P. Leemans. Multistage coupling of independent laser-plasma accelerators. *Nature*, 530:190 EP –, Feb 2016.

[14] R. A. Snavely, M. H. Key, S. P. Hatchett, T. E. Cowan, M. Roth, T. W. Phillips, M. A. Stoyer, E. A. Henry, T. C. Sangster, M. S. Singh, S. C. Wilks, A. MacKinnon, A. Offenberger, D. M. Pennington, K. Yasuike, A. B. Langdon, B. F. Lasinski, J. Johnson, M. D. Perry, and E. M. Campbell. Intense high-energy proton beams from petawatt-laser irradiation of solids. *Phys. Rev. Lett.*, 85:2945–2948, Oct 2000.

[15] Stephen P. Hatchett, Curtis G. Brown, Thomas E. Cowan, Eugene A. Henry, Joy S. Johnson, Michael H. Key, Jeffrey A. Koch, A. Bruce Langdon, Barbara F. Lasinski, Richard W. Lee, Andrew J. Mackinnon, Deanna M. Pennington, Michael D. Perry, Thomas W. Phillips, Markus Roth, T. Craig Sangster, Mike S. Singh, Richard A. Snavely, Mark A. Stoyer, Scott C. Wilks, and Kazuhito Yasuike. Electron, photon, and ion beams from the relativistic interaction of petawatt laser pulses with solid targets. *Physics of Plasmas*, 7(5):2076–2082, 2000.

[16] B. M. Hegelich, B. Albright, P. Audebert, A. Blazevic, E. Brambrink, J. Cobble, T. Cowan, J. Fuchs, J. C. Gauthier, C. Gautier, M. Geissel, D. Habs, R. Johnson, S. Karsch, A. Kemp, S. Letzring, M. Roth, U. Schramm, J. Schreiber, K. J. Witte, and J. C. Fernandez. Spectral properties of laser-accelerated mid-z mev/u ion beams. *Physics of Plasmas*, 12(5):056314, 2005.

[17] S. C. Wilks, A. B. Langdon, T. E. Cowan, M. Roth, M. Singh, S. Hatchett, M. H. Key, D. Pennington, A. MacKinnon, and R. A. Snavely. Energetic proton generation in ultra-intense laser-solid interactions. *Physics of Plasmas*, 8(2):542–549, 2001.

[18] M. Roth, T. E. Cowan, M. H. Key, S. P. Hatchett, C. Brown, W. Fountain, J. Johnson, D. M. Pennington, R. A. Snavely, S. C. Wilks, K. Yasuike, H. Ruhl, F. Pegoraro, S. V. Bulanov, E. M. Campbell, M. D. Perry, and H. Powell. Fast ignition by intense laser-accelerated proton beams. *Phys. Rev. Lett.*, 86:436–439, Jan 2001.

[19] C. Benedetti, P. Londrillo, T.V. Liseykina, A. Macchi, A. Sgattoni, and G. Turchetti. Ion acceleration by petawatt class laser pulses and pellet compression in a fast ignition scenario. *Nuclear Instruments and Methods in Physics Research Section A: Accelerators, Spectrometers, Detectors and Associated Equipment*, 606(1):89 – 93, 2009. Heavy Ion Inertial Fusion.

[20] P. K. Patel, A. J. Mackinnon, M. H. Key, T. E. Cowan, M. E. Foord, M. Allen, D. F. Price, H. Ruhl, P. T. Springer, and R. Stephens. Isochoric heating of solid-density matter with an ultrafast proton beam. *Phys. Rev. Lett.*, 91:125004, Sep 2003.

[21] G. M. Dyer, A. C. Bernstein, B. I. Cho, J. Osterholz, W. Grigsby, A. Dalton, R. Shepherd, Y. Ping, H. Chen, K. Widmann, and T. Ditmire. Equation-of-state measurement of dense plasmas heated with fast protons. *Phys. Rev. Lett.*, 101:015002, Jul 2008.

[22] A. Pelka, G. Gregori, D. O. Gericke, J. Vorberger, S. H. Glenzer, M. M. Günther, K. Harres, R. Heathcote, A. L. Kritcher, N. L. Kugland, B. Li, M. Makita, J. Mithen, D. Neely, C. Niemann, A. Otten, D. Riley, G. Schaumann, M. Schollmeier, An. Tauschwitz, and M. Roth. Ultrafast melting of carbon induced by intense proton beams. *Phys. Rev. Lett.*, 105:265701, Dec 2010.

[23] K. Nemoto, A. Maksimchuk, S. Banerjee, K. Flippo, G. Mourou, D. Umstadter, and V. Yu. Bychenkov. Laser-triggered ion acceleration and table top isotope production. *Applied Physics Letters*, 78(5):595–597, 2001.

[24] Ingo Hofmann, Jürgen Meyer ter Vehn, Xueqing Yan, and Husam Al-Omari. Chromatic energy filter and characterization of laser-accelerated proton beams for particle therapy. *Nuclear Instruments and Methods in Physics Research Section A: Accelerators, Spectrometers, Detectors and Associated Equipment*, 681(Supplement C):44 – 54, 2012.

[25] Paul R. Bolton. The integrated laser-driven ion accelerator system and the laser-driven ion beam radiotherapy challenge. *Nuclear Instruments and Methods in Physics Research Section A: Accelerators, Spectrometers, Detectors and Associated Equipment*, 809(Supplement C):149 – 155, 2016. Advances in detectors and applications for medicine.

[26] A. J. Mackinnon, P. K. Patel, R. P. Town, M. J. Edwards, T. Phillips, S. C. Lerner, D. W. Price, D. Hicks, M. H. Key, S. Hatchett, S. C. Wilks, M. Borghesi, L. Romagnani, S. Kar, T. Toncian, G. Pretzler, O. Willi, M. Koenig, E. Martinolli, S. Lepape, A. Benuzzi-Mounaix, P. Audebert, J. C. Gauthier, J. King, R. Snavely, R. R. Freeman, and T. Boehlly. Proton radiography as an electromagnetic field and density perturbation diagnostic (invited). *Review of Scientific Instruments*, 75(10):3531–3536, 2004.

[27] M. Roth, D. Jung, K. Falk, N. Guler, O. Deppert, M. Devlin, A. Favalli, J. Fernandez, D. Gautier, M. Geissel, R. Haight, C. E. Hamilton, B. M. Hegelich, R. P. Johnson, F. Merrill, G. Schaumann, K. Schoenberg, M. Schollmeier, T. Shimada, T. Taddeucci, J. L. Tybo, F. Wagner, S. A. Wender, C. H. Wilde, and G. A. Wurden. Bright laser-driven neutron source based on the relativistic transparency of solids. *Phys. Rev. Lett.*, 110:044802, Jan 2013.

[28] A. Kleinschmidt, V. Bagnoud, O. Deppert, A. Favalli, S. Frydrych, J. Hornung, D. Jahn, G. Schaumann, A. Tebartz, F. Wagner, G. Wurden, B. Zielbauer, and M. Roth. Intense, directed neutron beams from a laser-driven neutron source at phelix. *Physics of Plasmas*, 25(5):053101, 2018.

[29] L. Yin, B. J. Albright, B. M. Hegelich, and J. C. Fernandez. Gev laser ion acceleration from ultrathin targets: The laser break-out afterburner. *Laser and Particle Beams*, 24(2):291–298, 2006.

[30] F. Wagner, S. Bedacht, V. Bagnoud, O. Deppert, S. Geschwind, R. Jaeger, A. Ortner, A. Tebartz, B. Zielbauer, D. H. H. Hoffmann, and M. Roth. Simultaneous observation of

angularly separated laser-driven proton beams accelerated via two different mechanisms. *Physics of Plasmas*, 22(6):063110, 2015.

[31] A. Henig, D. Kiefer, K. Markey, D. C. Gautier, K. A. Flippo, S. Letzring, R. P. Johnson, T. Shimada, L. Yin, B. J. Albright, K. J. Bowers, J. C. Fernández, S. G. Rykovanov, H.-C. Wu, M. Zepf, D. Jung, V. Kh. Liechtenstein, J. Schreiber, D. Habs, and B. M. Hegelich. Enhanced laser-driven ion acceleration in the relativistic transparency regime. *Phys. Rev. Lett.*, 103:045002, Jul 2009.

[32] Bruno Gonzalez-Izquierdo, Ross J. Gray, Martin King, Rachel J. Dance, Robbie Wilson, John McCreadie, Nicholas M. H. Butler, Remi Capdessus, Steve Hawkes, James S. Green, Marco Borghesi, David Neely, and Paul McKenna. Optically controlled dense current structures driven by relativistic plasma aperture-induced diffraction. *Nature Physics*, 12:505 EP –, Jan 2016. Article.

[33] A P L Robinson, M Zepf, S Kar, R G Evans, and C Bellei. Radiation pressure acceleration of thin foils with circularly polarized laser pulses. *New Journal of Physics*, 10(1):013021, 2008.

[34] T. E. Cowan, J. Fuchs, H. Ruhl, A. Kemp, P. Audebert, M. Roth, R. Stephens, I. Barton, A. Blazevic, E. Brambrink, J. Cobble, J. Fernández, J.-C. Gauthier, M. Geissel, M. Hegelich, J. Kaae, S. Karsch, G. P. Le Sage, S. Letzring, M. Manclossi, S. Meyroneinc, A. Newkirk, H. Pépin, and N. Renard-LeGalloudec. Ultralow emittance, multi-mev proton beams from a laser virtual-cathode plasma accelerator. *Phys. Rev. Lett.*, 92:204801, May 2004.

[35] Teresa Bartal, Mark E. Foord, Claudio Bellei, Michael H. Key, Kirk A. Flippo, Sandrine A. Gaillard, Dustin T. Offermann, Pravesh K. Patel, Leonard C. Jarrott, Drew P. Higginson, Markus Roth, Anke Otten, Dominik Kraus, Richard B. Stephens, Harry S. McLean, Emilio M. Giraldez, Mingsheng S. Wei, Donald C. Gautier, and Farhat N. Beg. Focusing of short-pulse high-intensity laser-accelerated proton beams. *Nature Physics*, 8:139 EP –, Dec 2011.

[36] M. Schollmeier, S. Becker, M. Geißel, K. A. Flippo, A. Blažević, S. A. Gaillard, D. C. Gautier, F. Grüner, K. Harres, M. Kimmel, F. Nürnberg, P. Rambo, U. Schramm, J. Schreiber, J. Schütrumpf, J. Schwarz, N. A. Tahir, B. Atherton, D. Habs, B. M. Hegelich, and M. Roth. Controlled transport and focusing of laser-accelerated protons with miniature magnetic devices. *Phys. Rev. Lett.*, 101:055004, Aug 2008.

[37] T. Burris-Mog, K. Harres, F. Nürnberg, S. Busold, M. Bussmann, O. Deppert, G. Hoffmeister, M. Joost, M. Sobiella, A. Tauschwitz, B. Zielbauer, V. Bagnoud, T. Herrmannsdoerfer, M. Roth, and T. E. Cowan. Laser accelerated protons captured and transported by a pulse power solenoid. *Phys. Rev. ST Accel. Beams*, 14:121301, Dec 2011.

[38] K. Harres, I. Alber, A. Tauschwitz, V. Bagnoud, H. Daido, M. Günther, F. Nürnberg, A. Otten, M. Schollmeier, J. Schütrumpf, M. Tampo, and M. Roth. Beam collimation and transport of quasineutral laser-accelerated protons by a solenoid field. *Physics of Plasmas*, 17(2):023107, 2010.

[39] S. Busold, D. Schumacher, C. Brabetz, D. Jahn, F. Kroll, O. Deppert, A. Blažević, V. Bagnoud, and M. Roth. Towards highest peak intensities for ultra-short mev-range ion bunches. *Scientific Reports*, 5, July 2015.

[40] Giuseppe A.P. Cirrone, Massimo Carpinelli, Giacomo Cuttone, Santo Gammino, S. Bijan Jia, Georg Korn, Mario Maggiore, Lorenzo Manti, Daniele Margarone, Jan Prokupek, Marcella Renis, Francesco Romano, Francesco Schillaci, Barbara Tomasello, Lorenzo Torrisi, Antonella Tramontana, and Andriy Velyhan. Elimed, future hadrontherapy applications of laser-accelerated beams. *Nuclear Instruments and Methods in Physics Research Section A: Accelerators, Spectrometers, Detectors and Associated Equipment*, 730(Supplement C):174 – 177, 2013. Proceedings of the 9th International Conference on Radiation Effects on Semiconductor Materials Detectors and Devices.

[41] U. Masood, M. Bussmann, T. E. Cowan, W. Enghardt, L. Karsch, F. Kroll, U. Schramm, and J. Pawelke. A compact solution for ion beam therapy with laser accelerated protons. *Applied Physics B*, 117(1):41–52, Oct 2014.

[42] S. Busold, A. Almomani, V. Bagnoud, W. Barth, S. Bedacht, A. Blazevic, O. Boine-Frankenheim, C. Brabetz, T. Burris-Mog, T.E. Cowan, O. Deppert, M. Droba, H. Eickhoff, U. Eisenbarth, K. Harres, G. Hoffmeister, I. Hofmann, O. Jaeckel, R. Jaeger, M. Joost, S. Kraft, F. Kroll, M. Kaluza, O. Kester, Z. Lecz, T. Merz, F. Nürnberg, H. Al-Omari, A. Orzhekhovskaya, G. Paulus, J. Polz, U. Ratzinger, M. Roth, G. Schaumann, P. Schmidt, U. Schramm, G. Schreiber, D. Schumacher, T. Stoehlker, A. Tauschwitz, W. Vinzenz, F. Wagner, S. Yaramyshev, and B. Zielbauer. Shaping laser accelerated ions for future applications - the light collaboration. *Nuclear Instruments and Methods in Physics Research Section A: Accelerators, Spectrometers, Detectors and Associated Equipment*, 740(Supplement C):94 – 98, 2014. Proceedings of the first European Advanced Accelerator Concepts Workshop 2013.

[43] Knut Jochen Harres. *Strahltransport laserbeschleunigter Ionen*. PhD thesis, Technische Universität, Darmstadt, August 2010.

[44] T. J. Burris-Mog. *Capture and Transport of Laser Accelerated Protons by Pulsed Magnetic Fields: Advancements Toward Laser-Based Proton Therapy*. PhD thesis, University of Nevada, Reno, 2012.

[45] S. Busold, D. Schumacher, O. Deppert, C. Brabetz, F. Kroll, A. Blažević, V. Bagnoud, and M. Roth. Commissioning of a compact laser-based proton beam line for high intensity bunches around 10 mev. *Phys. Rev. ST Accel. Beams*, 17:031302, Mar 2014.

[46] Simon Busold. *Construction and characterization of a laser-driven proton beamline at GSI*. PhD thesis, Technische Universität Darmstadt, Darmstadt, Mai 2014.

[47] Florian Kroll. *The study and development of pulse high-field magnets for application in laser-plasma physics*. PhD thesis, Technische Universität Dresden, Dresden, Dezember 2017.

[48] D. Jahn, D. Schumacher, C. Brabetz, J. Ding, S. Weih, F. Kroll, F.E. Brack, U. Schramm, A. Blazevic, and M. Roth. First application studies at the laser-driven light beamline: Improving proton beam homogeneity and imaging of a solid target. *Nuclear Instruments*

and Methods in Physics Research Section A: Accelerators, Spectrometers, Detectors and Associated Equipment, 2018.

[49] G. Schaumann, M.S. Schollmeier, G. Rodriguez-Prieto, A. Blazevic, E. Brambrink, M. Geissler, S. Korosity, Pirzadeh P., M. Roth, F.B. Rosmej, and et al. High energy heavy ion jets emerging from laser plasma generated by long pulse laser beams from the nhelix laser system at gsi. *Laser and Particle Beams*, 23(4):503–512, 2005.

[50] O. A. Hurricane, D. A. Callahan, D. T. Casey, E. L. Dewald, T. R. Dittrich, T. Döppner, S. Haan, D. E. Hinkel, L. F. Berzak Hopkins, O. Jones, A. L. Kritcher, S. Le Pape, T. Ma, A. G. MacPhee, J. L. Milovich, J. Moody, A. Pak, H.-S. Park, P. K. Patel, J. E. Ralph, H. F. Robey, J. S. Ross, J. D. Salmonson, B. K. Spears, P. T. Springer, R. Tommasini, F. Albert, L. R. Benedetti, R. Bionta, E. Bond, D. K. Bradley, J. Caggiano, P. M. Celliers, C. Cerjan, J. A. Church, R. Dylla-Spears, D. Edgell, M. J. Edwards, D. Fittinghoff, M. A. Barrios Garcia, A. Hamza, R. Hatarik, H. Herrmann, M. Hohenberger, D. Hoover, J. L. Kline, G. Kyrala, B. Kozioziemski, G. Grim, J. E. Field, J. Frenje, N. Izumi, M. Gatu Johnson, S. F. Khan, J. Knauer, T. Kohut, O. Landen, F. Merrill, P. Michel, A. Moore, S. R. Nagel, A. Nikroo, T. Parham, R. R. Rygg, D. Sayre, M. Schneider, D. Shaughnessy, D. Strozzi, R. P. J. Town, D. Turnbull, P. Volegov, A. Wan, K. Widmann, C. Wilde, and C. Yeamans. Inertially confined fusion plasmas dominated by alpha-particle self-heating. *Nature Physics*, 12:800 EP –, Apr 2016. Article.

[51] A. Frank, A. Blažević, V. Bagnoud, M. M. Basko, M. Börner, W. Cayzac, D. Kraus, T. Heßling, D. H. H. Hoffmann, A. Ortner, A. Otten, A. Pelka, D. Pepler, D. Schumacher, An. Tauschwitz, and M. Roth. Energy loss and charge transfer of argon in a laser-generated carbon plasma. *Phys. Rev. Lett.*, 110:115001, Mar 2013.

[52] W. Cayzac, A. Frank, A. Ortner, V. Bagnoud, M. M. Basko, S. Bedacht, C. Bläser, A. Blazevic, S. Busold, O. Deppert, J. Ding, M. Ehret, P. Fiala, S. Frydrych, D. O. Gericke, L. Hallo, J. Helfrich, D. Jahn, E. Kjartansson, A. Knetsch, D. Kraus, G. Malka, N. W. Neumann, K. Pépitone, D. Pepler, S. Sander, G. Schaumann, T. Schlegel, N. Schroeter, D. Schumacher, M. Seibert, An Tauschwitz, J. Vorberger, F. Wagner, S. Weih, Y. Zobus, and M. Roth. Experimental discrimination of ion stopping models near the bragg peak in highly ionized matter. *Nature Communications*, 8:15693 EP –, Jun 2017. Article.

[53] P. Mulser and D. Bauer. *High Power Laser-Matter interaction*. Springer, 2010.

[54] M Roth, M Allen, P Audebert, A Blazevic, E Brambrink, T E Cowan, J Fuchs, J-C Gauthier, M Geißel, M Hegelich, S Karsch, J Meyer ter Vehn, H Ruhl, T Schlegel, and R B Stephens. The generation of high-quality, intense ion beams by ultra-intense lasers. *Plasma Physics and Controlled Fusion*, 44(12B):B99, 2002.

[55] Francis F. Chen. *Introduction to Plasma Physics and Controlled Fusion*. Springer Spektrum, 2016.

[56] Eric Esarey, Phillip Sprangle, and Jonathan Krall. Laser acceleration of electrons in vacuum. *Phys. Rev. E*, 52:5443–5453, Nov 1995.

[57] P. Drude. Ueber fernewirkungen. *Annalen der Physik*, 298(12), 1897.

[58] D. Bauer, P. Mulser, and W. H. Steeb. Relativistic ponderomotive force, uphill acceleration, and transition to chaos. *Phys. Rev. Lett.*, 75:4622–4625, Dec 1995.

[59] J. Fuchs, P. Antici, E. d'Humières, E. Lefebvre, M. Borghesi, E. Brambrink, C. A. Cecchetti, M. Kaluza, V. Malka, M. Manclossi, S. Meyroneinc, P. Mora, J. Schreiber, T. Toncian, H. Pépin, and P. Audebert. Laser-driven proton scaling laws and new paths towards energy increase. *Nature Physics*, 2:48 EP –, Dec 2005. Article.

[60] Paul A. Tipler and Gene Mosca. *Physik*. Springer Spektrum, 2013.

[61] Z. Deng and J. H. Eberly. Multiphoton absorption above ionization threshold by atoms in strong laser fields. *J. Opt. Soc. Am. B*, 2(3):486–493, Mar 1985.

[62] L.D. Landau and E.M. Lifschitz. *Lehrbuch der theoretischen Physik Band III Quantenmechanik*. Akademie-Verlag, Berlin, 1976.

[63] Vladimir S. Popov. Laser acceleration of electrons in vacuum. *Phys.-Usp.*, 47, 2004.

[64] A. J. McAlister and E. A. Stern. Plasma resonance absorption in thin metal films. *Phys. Rev.*, 132:1599–1602, Nov 1963.

[65] J. P. Freidberg, R. W. Mitchell, R. L. Morse, and L. I. Rudsinski. Resonant absorption of laser light by plasma targets. *Phys. Rev. Lett.*, 28:795–799, Mar 1972.

[66] F. Brunel. Not-so-resonant, resonant absorption. *Phys. Rev. Lett.*, 59:52–55, Jul 1987.

[67] W. L. Kruer and Kent Estabrook. JxB heating by very intense laser light. *The Physics of Fluids*, 28(1):430–432, 1985.

[68] S. C. Wilks, W. L. Kruer, M. Tabak, and A. B. Langdon. Absorption of ultra-intense laser pulses. *Phys. Rev. Lett.*, 69:1383–1386, Aug 1992.

[69] S. C. Wilks. Simulations of ultraintense laser-plasma interactions. *Physics of Fluids B: Plasma Physics*, 5(7):2603–2608, 1993.

[70] Marius Schollmeier. *Optimization and control of laser-accelerated proton beams*. PhD thesis, Technische Universität, Darmstadt, 2008.

[71] Paul McKenna, David Neely, Robert Bingham, and Dino Jaroszynski. *Laser-Plasma Interactions and Applications*. Springer, 2013.

[72] Matthew Allen, Pravesh K. Patel, Andrew Mackinnon, Dwight Price, Scott Wilks, and Edward Morse. Direct experimental evidence of back-surface ion acceleration from laser-irradiated gold foils. *Phys. Rev. Lett.*, 93:265004, Dec 2004.

[73] M. Borghesi, J. Fuchs, S. V. Bulanov, A. J. MacKinnon, P. K. Patel, and M. Roth. Fast ion generation by high-intensity laser irradiation of solid targets and applications. *Fusion Science and Technology*, 49(3):412–439, 2006.

[74] Hannes Alfvén. On the motion of cosmic rays in interstellar space. *Phys. Rev.*, 55:425–429, Mar 1939.

[75] J.R. Davies. The Alfvén limit revisited and its relevance to laser-plasma interactions. *Laser and Particle Beams*, 24(2):299–310, 2006.

[76] H. A. Bethe. Molière's theory of multiple scattering. *Phys. Rev.*, 89:1256–1266, Mar 1953.

[77] M. Passoni and M. Lontano. One-dimensional model of the electrostatic ion acceleration in the ultraintense laser-solid interaction. *Laser and Particle Beams*, 22(2):163–169, 2004.

[78] M. Passoni, V. T. Tikhonchuk, M. Lontano, and V. Yu. Bychenkov. Charge separation effects in solid targets and ion acceleration with a two-temperature electron distribution. *Phys. Rev. E*, 69:026411, Feb 2004.

[79] Matthew Allen, Pravesh K. Patel, Andrew Mackinnon, Dwight Price, Scott Wilks, and Edward Morse. Direct experimental evidence of back-surface ion acceleration from laser-irradiated gold foils. *Phys. Rev. Lett.*, 93:265004, Dec 2004.

[80] Florian Wagner. *Kontrolle des zeitlichen Kontrastes am Lasersystem PHELIX*. PhD thesis, Technische Universität, Darmstadt, December 2014.

[81] Florian Wagner, Stefan Bedacht, Alex Ortner, Markus Roth, Anna Tauschwitz, Bernhard Zielbauer, and Vincent Bagnoud. Pre-plasma formation in experiments using petawatt lasers. *Opt. Express*, 22(24):29505–29514, Dec 2014.

[82] P. Mora. Plasma expansion into a vacuum. *Phys. Rev. Lett.*, 90:185002, May 2003.

[83] J. Fuchs, P. Antici, E. d'Humières, E. Lefebvre, M. Borghesi, E. Brambrink, C. A. Cecchetti, M. Kaluza, V. Malka, M. Manclossi, S. Meyroneinc, P. Mora, J. Schreiber, T. Toncian, H. Pépin, and P. Audebert. Laser-driven proton scaling laws and new paths towards energy increase. *Nature Physics*, 2:48 EP –, Dec 2005. Article.

[84] A. Pukhov. Three-dimensional simulations of ion acceleration from a foil irradiated by a short-pulse laser. *Phys. Rev. Lett.*, 86:3562–3565, Apr 2001.

[85] J. J. Honrubia, M. Kaluza, J. Schreiber, G. D. Tsakiris, and J. Meyer-ter Vehn. Laser-driven fast-electron transport in preheated foil targets. *Physics of Plasmas*, 12(5):052708, 2005.

[86] Zsolt Lecz, Vladimir Kornilov, and Oliver Boine-Frankenheim. PIC Simulations of Laser Ion Acceleration via TNSA. In *Proceedings, 11th International Computational Accelerator Physics Conference (ICAP 2012): Rostock-Warnemünde, Germany, August 19-24, 2012*, page FRSAI3, 2012.

[87] M. Hegelich, S. Karsch, G. Pretzler, D. Habs, K. Witte, W. Guenther, M. Allen, A. Blazevic, J. Fuchs, J. C. Gauthier, M. Geissel, P. Audebert, T. Cowan, and M. Roth. Mev ion jets from short-pulse-laser interaction with thin foils. *Phys. Rev. Lett.*, 89:085002, Aug 2002.

[88] Björn Manuel Hegelich. *Acceleration of heavy ions to MeV/nucleon energies by ultrahigh-intensity laser*. PhD thesis, Ludwigs-Maximilian-Universität, München, 2002.

[89] M. Roth, T. E. Cowan, M. H. Key, S. P. Hatchett, C. Brown, W. Fountain, J. Johnson, D. M. Pennington, R. A. Snavely, S. C. Wilks, K. Yasuike, H. Ruhl, F. Pegoraro, S. V. Bulanov, E. M. Campbell, M. D. Perry, and H. Powell. Fast ignition by intense laser-accelerated proton beams. *Phys. Rev. Lett.*, 86:436–439, Jan 2001.

[90] A. J. Mackinnon, M. Borghesi, S. Hatchett, M. H. Key, P. K. Patel, H. Campbell, A. Schiavi, R. Snavely, S. C. Wilks, and O. Willi. Effect of plasma scale length on multi-mev proton production by intense laser pulses. *Phys. Rev. Lett.*, 86:1769–1772, Feb 2001.

[91] M.V. Ammosov, N.B. Delone, and V.P. Krainov. Tunnel ionization of complex atoms and of atomic ions in an alternating electromagnetic field. *JETP*, 64:1191, December 1986.

[92] V. P. Krainov. Theory of barrier-suppression ionization of atoms. *Journal of Nonlinear Optical Physics and Materials*, 04(04):775–798, 1995.

[93] B. M. Penetrante and J. N. Bardsley. Residual energy in plasmas produced by intense subpicosecond lasers. *Phys. Rev. A*, 43:3100–3113, Mar 1991.

[94] Yong-Ki Kim and M. Eugene Rudd. Binary-encounter-dipole model for electron-impact ionization. *Phys. Rev. A*, 50:3954–3967, Nov 1994.

[95] V. T. Tikhonchuk. Interaction of a beam of fast electrons with solids. *Physics of Plasmas*, 9(4):1416–1421, 2002.

[96] A. Henig, S. Steinke, M. Schnürer, T. Sokollik, R. Hörlein, D. Kiefer, D. Jung, J. Schreiber, B. M. Hegelich, X. Q. Yan, J. Meyer-ter Vehn, T. Tajima, P. V. Nickles, W. Sandner, and D. Habs. Radiation-pressure acceleration of ion beams driven by circularly polarized laser pulses. *Phys. Rev. Lett.*, 103:245003, Dec 2009.

[97] G. Hoffmeister, C. Bellei, K. Harres, D. Ivanov, D. Kraus, A. Pelka, B. Rethfeld, G. Schaumann, and M. Roth. Influence of fs-laser desorption on target normal sheath accelerated ions. *Phys. Rev. ST Accel. Beams*, 16:041304, Apr 2013.

[98] J.P. Joule. On the existence of an equivalent relation between heat and the ordinary forms of mechanical power. *Philosophical Magazine*, 3(27):205–207, 1845.

[99] B. M. Hegelich, B. J. Albright, J. Cobble, K. Flippo, S. Letzring, M. Paffett, H. Ruhl, J. Schreiber, R. K. Schulze, and J. C. Fernández. Laser acceleration of quasi-monoenergetic mev ion beams. *Nature*, 439:441 EP –, Jan 2006.

[100] K.A. Flippo, B.M. Hegelich, M.J. Schmitt, C.A. Meserole, G.L. Fisher, D.C. Gautier, J.A. Cobble, R. Johnson, S. Letzring, J. Schreiber, M. Schollmeier, and J.C. Fernández. Ultrashort-laser-produced heavy ion generation via target laser-ablation cleaning. *J. Phys. IV France*, 133:1117–1122, 2006.

[101] Gabriele Hoffmeister. *Influencing laser-accelerated ions by femtosecond-laser desorption*. PhD thesis, Technische Universität Darmstadt, Darmstadt, May 2014.

[102] F. Wagner, C. P. João, J. Fils, T. Gottschall, J. Hein, J. Körner, J. Limpert, M. Roth, T. Stöhlker, and V. Bagnoud. Temporal contrast control at the phelix petawatt laser facility by means of tunable sub-picosecond optical parametric amplification. *Applied Physics B*, 116(2):429–435, Aug 2014.

[103] J. E. Murray and W. H. Lowdermilk. Nd:yag regenerative amplifier. *Journal of Applied Physics*, 51(7):3548–3556, 1980.

[104] W. H. Lowdermilk and J. E. Murray. The multipass amplifier: Theory and numerical analysis. *Journal of Applied Physics*, 51(5):2436–2444, 1980.

[105] Christian Brabetz. Wellenfront kontrolle am phelix-lasersystem mit adaptiver optik. Master's thesis, Technische Universität Darmstadt, Darmstadt, 2010.

[106] Azam Niroomand-Rad, Charles Robert Blackwell, Bert M. Coursey, Kenneth P. Gall, James M. Galvin, William L. McLaughlin, Ali S. Meigooni, Ravinder Nath, James E. Rodgers, and Christopher G. Soares. Radiochromic film dosimetry: Recommendations of aapm radiation therapy committee task group 55. *Medical Physics*, 25(11):2093–2115, 1998.

[107] J.J. Thomson. Bakerian lecture:—rays of positive electricity. *Proceedings of the Royal Society of London A: Mathematical, Physical and Engineering Sciences*, 89(607):1–20, 1913.

[108] F. Nürnberg, M. Schollmeier, E. Brambrink, A. Blazevic, D. C. Carroll, K. Flippo, D. C. Gautier, M. Geißel, K. Harres, B. M. Hegelich, O. Lundh, K. Markey, P. McKenna, D. Neely, J. Schreiber, and M. Roth. Radiochromic film imaging spectroscopy of laser-accelerated proton beams. *Review of Scientific Instruments*, 80(3):033301, 2009.

[109] William L. McLaughlin, Mohamad Al-Sheikhly, D. F. Lewis, A. Kovacs, and L. Wojnarovits. *Radiochromic Solid-State Polymerization Reaction*, chapter 11, pages 152–166. 1996.

[110] Antje Schreiber. RGB-Farb-Kalibrierung von radiochromatischen Filmen, Bachelor thesis, 2012.

[111] D. Kirby, S. Green, F. Fiorini, D. Parker, L. Romagnani, D. Doria, S. Kar, C. Lewis, M. Borghesi, H. Palmans, and et al. Radiochromic film spectroscopy of laser-accelerated proton beams using the fluka code and dosimetry traceable to primary standards. *Laser and Particle Beams*, 29(2):231–239, 2011.

[112] Frank Nürnberg. *Laser-Accelerated Proton Beams as a New Particle Source*. PhD thesis, Technische Universität, Darmstadt, November 2010.

[113] Christian Brabetz. *Development of specially shaped laser beams for the optimized acceleration of particles*. PhD thesis, Goethe Universität, Frankfurt am Main, 2014.

[114] Willy Wien. Untersuchungen über die electrische Entladung in verdünnten Gasen. *Annalen der Physik*, 301(6):440–452, 1899.

[115] Dassault Systems. CST Particle Studio - A charge particle dynamics simulation tool. Available at `https://www.cst.com/products/cstps`.

[116] A. Poyé, S. Hulin, M. Bailly-Grandvaux, J.-L. Dubois, J. Ribolzi, D. Raffestin, M. Bardon, F. Lubrano-Lavaderci, E. D'Humières, J. J. Santos, Ph. Nicolaï, and V. Tikhonchuk. Physics of giant electromagnetic pulse generation in short-pulse laser experiments. *Phys. Rev. E*, 91:043106, Apr 2015.

[117] D C Carroll, O Tresca, R Prasad, L Romagnani, P S Foster, P Gallegos, S Ter-Avetisyan, J S Green, M J V Streeter, N Dover, C A J Palmer, C M Brenner, F H Cameron, K E Quinn, J Schreiber, A P L Robinson, T Baeva, M N Quinn, X H Yuan, Z Najmudin, M Zepf, D Neely, M Borghesi, and P McKenna. Carbon ion acceleration from thin foil targets irradiated by ultrahigh-contrast, ultraintense laser pulses. *New Journal of Physics*, 12(4):045020, 2010.

[118] A P L Robinson, P Foster, D Adams, D C Carroll, B Dromey, S Hawkes, S Kar, Y T Li, K Markey, P McKenna, C Spindloe, M Streeter, C-G Wahlström, M H Xu, M Zepf,

and D Neely. Spectral modification of laser-accelerated proton beams by self-generated magnetic fields. *New Journal of Physics*, 11(8):083018, 2009.

[119] K. Harres, M. Schollmeier, E. Brambrink, P. Audebert, A. Blazevic, K. Flippo, D. C. Gautier, M. Geißel, B. M. Hegelich, F. Nürnberg, J. Schreiber, H. Wahl, and M. Roth. Development and calibration of a thomson parabola with microchannel plate for the detection of laser-accelerated mev ions. *Review of Scientific Instruments*, 79(9):093306, 2008.

[120] S. G. Gales and C. D. Bentley. Image plates as x-ray detectors in plasma physics experiments. *Review of Scientific Instruments*, 75(10):4001–4003, 2004.

[121] A. Alejo, S. Kar, A. Tebartz, H. Ahmed, S. Astbury, D. C. Carroll, J. Ding, D. Doria, A. Higginson, P. McKenna, N. Neumann, G. G. Scott, F. Wagner, M. Roth, and M. Borghesi. High resolution thomson parabola spectrometer for full spectral capture of multi-species ion beams. *Review of Scientific Instruments*, 87(8):083304, 2016.

[122] A. P. Fews and D. L. Henshaw. High resolution alpha particle spectroscopy using CR-39 plastic track detector. *Nuclear Instruments and Methods in Physics Research*, 197:517–529, June 1982.

[123] Paul Leblans, Dirk Vandenbroucke, and Peter Willems. Storage phosphors for medical imaging. *Materials*, 4(6):1034–1086, 2011.

[124] I J Paterson, R J Clarke, N C Woolsey, and G Gregori. Image plate response for conditions relevant to laser-plasma interaction experiments. *Measurement Science and Technology*, 19(9):095301, 2008.

[125] A. Mancic, J. Fuchs, P. Antici, S. A. Gaillard, and P. Audebert. Absolute calibration of photostimulable image plate detectors used as (0.5-20mev) high-energy proton detectors. *Review of Scientific Instruments*, 79(7):073301, 2008.

[126] D. Doria, S. Kar, H. Ahmed, A. Alejo, J. Fernandez, M. Cerchez, R. J. Gray, F. Hanton, D. A. MacLellan, P. McKenna, Z. Najmudin, D. Neely, L. Romagnani, J. A. Ruiz, G. Sarri, C. Scullion, M. Streeter, M. Swantusch, O. Willi, M. Zepf, and M. Borghesi. Calibration of bas-tr image plate response to high energy (3-300 mev) carbon ions. *Review of Scientific Instruments*, 86(12):123302, 2015.

[127] D. C. Carroll, P. Brummitt, D. Neely, Filip Lindau, Olle Lundh, Claes-Göran Wahlström, and P. McKenna. *A modified Thomson parabola spectrometer for high resolution multi-MeV ion measurements-Application to laser-driven ion acceleration*, volume 620. Elsevier, Netherlands, 2010.

[128] COMSOL. COMSOL Multiphysics Modeling Softwarel. Available at `https://www.comsol.com`.

[129] L. Michalski, K. Eckersdorf, J. Kucharski, and J. McGhee. *Temperature Measurement*. Wiley, 2001.

[130] Y S Touloukian and D P DeWitt. *Thermophysical Properties of Matter - The TPRC Data Series. Volume 7. Thermal Radiative Properties - Metallic Elements and Alloys*. Defense Technical Information Center, 1970.

[131] E. Brambrink, J. Schreiber, T. Schlegel, P. Audebert, J. Cobble, J. Fuchs, M. Hegelich, and M. Roth. Transverse characteristics of short-pulse laser-produced ion beams: A study of the acceleration dynamics. *Phys. Rev. Lett.*, 96:154801, Apr 2006.

[132] E. L. Clark, K. Krushelnick, J. R. Davies, M. Zepf, M. Tatarakis, F. N. Beg, A. Machacek, P. A. Norreys, M. I. K. Santala, I. Watts, and A. E. Dangor. Measurements of energetic proton transport through magnetized plasma from intense laser interactions with solids. *Phys. Rev. Lett.*, 84:670–673, Jan 2000.

[133] Yoshihiro Murakami, Yoneyoshi Kitagawa, Yasuhiko Sentoku, Michiaki Mori, Ryosuke Kodama, Kazuo A. Tanaka, Kunioki Mima, and Tatsuhiko Yamanaka. Observation of proton rear emission and possible gigagauss scale magnetic fields from ultra-intense laser illuminated plastic target. *Physics of Plasmas*, 8(9):4138–4143, 2001.

[134] S. Gaillard, J. Fuchs, N. Renard-LeGalloudec, and T. E. Cowan. Comment on ”measurements of energetic proton transport through magnetized plasma from intense laser interactions with solids”. *Phys. Rev. Lett.*, 96:249201, Jun 2006.

[135] S. Gaillard, J. Fuchs, N. Renard-Le Galloudec, and T. E. Cowan. Study of saturation of CR39 nuclear track detectors at high ion fluence and of associated artifact patterns. *Review of Scientific Instruments*, 78(1):013304, 2007.

[136] H. Padda, M. King, R. J. Gray, H. W. Powell, B. Gonzalez-Izquierdo, L. C. Stockhausen, R. Wilson, D. C. Carroll, R. J. Dance, D. A. MacLellan, X. H. Yuan, N. M. H. Butler, R. Capdessus, M. Borghesi, D. Neely, and P. McKenna. Intra-pulse transition between ion acceleration mechanisms in intense laser-foil interactions. *Physics of Plasmas*, 23(6):063116, 2016.

[137] G A Becker, S Tietze, S Keppler, J Reislöhner, J H Bin, L Bock, F-E Brack, J Hein, M Hellwing, P Hilz, M Hornung, A Kessler, S D Kraft, S Kuschel, H Liebetrau, W Ma, J Polz, H-P Schlenvoigt, F Schorcht, M B Schwab, A Seidel, K Zeil, U Schramm, M Zepf, J Schreiber, S Rykovanov, and M C Kaluza. Ring-like spatial distribution of laser accelerated protons in the ultra-high-contrast tnsa-regime. *Plasma Physics and Controlled Fusion*, 60(5):055010, 2018.

[138] M. Nakatsutsumi, Y. Sentoku, A. Korzhimanov, S. N. Chen, S. Buffechoux, A. Kon, B. Atherton, P. Audebert, M. Geissel, L. Hurd, M. Kimmel, P. Rambo, M. Schollmeier, J. Schwarz, M. Starodubtsev, L. Gremillet, R. Kodama, and J. Fuchs. Self-generated surface magnetic fields inhibit laser-driven sheath acceleration of high-energy protons. *Nature Communications*, 9(1):280, 2018.

[139] G Sarri, C A Cecchetti, L Romagnani, C M Brown, D J Hoarty, S James, J Morton, M E Dieckmann, R Jung, O Willi, S V Bulanov, F Pegoraro, and M Borghesi. The application of laser-driven proton beams to the radiography of intense laser-hohlraum interactions. *New Journal of Physics*, 12(4):045006, 2010.

[140] S. Kar, M. Borghesi, P. Audebert, A. Benuzzi-Mounaix, T. Boehly, D. Hicks, M. Koenig, K. Lancaster, S. Lepape, A. Mackinnon, P. Norreys, P. Patel, and L. Romagnani. Modeling of laser-driven proton radiography of dense matter. *High Energy Density Physics*, 4(1):26 – 40, 2008.

[141] M. Borghesi, D.H. Campbell, A. Schiavi, O. Willi, A.J. Mackinnon, D. Hicks, P. Patel, L.A. Gizzi, M. Galimberti, R.J. Clarke, and et al. Laser-produced protons and their application as a particle probe. *Laser and Particle Beams*, 20(2):269–275, 2002.

[142] Annika Kleinschmidt. *Investigation of a laser-driven neutron source with respect to different fields of application*. PhD thesis, Technische Universität, Darmstadt, 2017.

[143] Frank Hinterberger. *Physik der Teilchenbeschleuniger und Ionenoptik*. Springer, 2008.

[144] Martin Reiser. *Theory and Design of Charged Particle Beams*. Wiley-VCH Verlag, 2008.

[145] B.J. Holzer. Introduction to Transverse Beam Dynamics. (arXiv:1404.0923):27–45. 19 p, Apr 2014. Comments: contribution to the CAS - CERN Accelerator School: Course on Superconductivity for Accelerators, Erice, Italy, 24 Apr - 4 May 2013, edited by R. Bailey, CERN-2014-005.

[146] B J Holzer. Introduction to Longitudinal Beam Dynamics. (arXiv:1404.0927):15 p, Apr 2014. Comments: 15 pages, contribution to the CAS-CERN Accelerator School: Ion Sources, Senec, Slovakia, 29 May - 8 June 2012, edited by R. Bailey, CERN-2013-007.

[147] Ingo Hofmann. *Space Charge Physics for Accelerators*. Springer, 2017.

[148] Karlheinz Schindl. Space charge. (CERN-PS-99-012-DI):26 p, Mar 1999.

[149] K. Halbach. Design of permanent multipole magnets with oriented rare earth cobalt material. *Nuclear Instruments and Methods*, 169(1):1 – 10, 1980.

[150] Busch H. Berechnung der Bahn von Kathodenstrahlen im axialsymmetrischen elektromagnetischen Felde. *Annalen der Physik*, 386(25):974–993, 1926.

[151] Vinit Kumar. Understanding the focusing of charged particle beams in a solenoid magnetic field. *American Journal of Physics*, 77(8):737–741, 2009.

[152] Ingo Hofmann. Performance of solenoids versus quadrupoles in focusing and energy selection of laser accelerated protons. *Phys. Rev. ST Accel. Beams*, 16(4):041302, 2013.

[153] J. Ding, D. Schumacher, D. Jahn, A. Blazevic, and M. Roth. Simulation studies on generation, handling and transport of laser-accelerated carbon ions. *Nuclear Instruments and Methods in Physics Research Section A: Accelerators, Spectrometers, Detectors and Associated Equipment*, 2018.

[154] Frank Nürnberg, A Friedman, D P Grote, K Harres, B G Logan, M Schollmeier, and M Roth. Warp simulations for capture and control of laser-accelerated proton beams. *Journal of Physics: Conference Series*, 244(2):022052, 2010.

[155] David P. Grote, Alex Friedman, Jean-Luc Vay, and Irving Haber. The warp code: Modeling high intensity ion beams. *AIP Conference Proceedings*, 749(1):55–58, 2005.

[156] Ali Almomani. *RF acceleration of intense laser generated proton bunches*. PhD thesis, Goethe Universität Frankfurt, 2012.

[157] A. Almomani, M. Droba, U. Ratzinger, and I. Hofmann. Matching the laser generated p bunch into a crossbar-h drift tube linac. *Phys. Rev. ST Accel. Beams*, 15:051302, May 2012.

[158] D. Uriot and N. Pichoff. Status of TraceWin code. *Proceedings of IPAC 2015*, 2015.

[159] Luc Devroye. Random variate generation for multivariate unimodal densities. *ACM Trans. Model. Comput. Simul.*, 7(4):447–477, October 1997.

[160] J. Schader, B. Kolb, K.D. Sevier, and K.O. Groeneveld. Electron ejection from beam-tilted-foil experiments. *Nuclear Instruments and Methods*, 151(3):563 – 565, 1978.

[161] H.J. Frischkorn, K.O. Groeneveld, D. Hofmann, P. Koschar, R. Latz, and J. Schader. Ion induced electron ejection from solids. *Nuclear Instruments and Methods in Physics Research*, 214(1):123 – 128, 1983.

[162] P. Koschar, K. Kroneberger, A. Clouvas, M. Burkhard, W. Meckbach, O. Heil, J. Kemmler, H. Rothard, K. O. Groeneveld, R. Schramm, and H.-D. Betz. Secondary-electron yield as a probe of preequilibrium stopping power of heavy ions colliding with solids. *Phys. Rev. A*, 40:3632–3636, Oct 1989.

[163] Peter A. Seidl, Arun Persaud, William L. Waldron, John J. Barnard, Ronald C. Davidson, Alex Friedman, Erik P. Gilson, Wayne G. Greenway, David P. Grote, Igor D. Kaganovich, Steven M. Lidia, Matthew Stettler, Jeffrey H. Takakuwa, and Thomas Schenkel. Short intense ion pulses for materials and warm dense matter research. *Nuclear Instruments and Methods in Physics Research Section A: Accelerators, Spectrometers, Detectors and Associated Equipment*, 800:98 – 103, 2015.

[164] Marc Zimmer. Neutralized drift compression for short and intense ion pulses. Master's thesis, Technische Universität Darmstadt, Darmstadt, 2016.

[165] Diana Jahn. Development of fast diamond detectors for temporal profile measurements of short, intense ion bunches. Master's thesis, Technische Universität Darmstadt, Darmstadt, 2016.

[166] E. Berdermann, M. Pomorski, W. de Boer, M. Ciobanu, S. Dunst, C. Grah, M. Kis, W. Koenig, W. Lange, W. Lohmann, R. Lovrincic, P. Moritz, J. Morse, S. Mueller, A. Pucci, M. Schreck, S. Rahman, and M. Träger. Diamond detectors for hadron physics research. *Diamond and Related Materials*, 19(5):358 – 367, 2010. Proceedings of Diamond 2009, The 20th European Conference on Diamond, Diamond-Like Materials, Carbon Nanotubes and Nitrides, Part 1.

[167] J. Häuser. *Eigenschaften von Spiralresonatoren*. PhD thesis, Goethe Universität Frankfurt, 1989.

[168] ATHENA: Helmholtz ARD Distributed Test Facility. More about it at `https://www.helmholtz-ard.de/e26746/`.

Publications

The articles, reviewed and non-reviewed, the author contributed to are listed below as well as contributions, posters and talks, to numerous national and international conferences and workshops.

Reviewed Publications

J. Ding, D. Schumacher, D. Jahn, A. Blazevic, and M. Roth. Simulation studies on generation, handling and transport of laser-accelerated carbon ions. *Nuclear Instruments and Methods in Physics Research Section A: Accelerators, Spectrometers, Detectors and Associated Equipment*, 2018, https://doi.org/10.1016/j.nima.2018.02.103

D. Jahn, D. Schumacher, C. Brabetz, **J. Ding**, S. Weih, F. Kroll, F.E. Brack, U. Schramm, A. Blazevic, and M. Roth. First application studies at the laser-driven LIGHT beamline: Improving proton beam homogeneity and imaging of a solid target. *Nuclear Instruments and Methods in Physics Research Section A: Accelerators, Spectrometers, Detectors and Associated Equipment*, 2018, https://doi.org/10.1016/j.nima.2018.02.026

W. Cayzac, A. Frank, A. Ortner, V. Bagnoud, M. M. Basko, S. Bedacht, C. Bläser, A. Blazevic, S. Busold, O. Deppert, **J. Ding**, M. Ehret, P. Fiala, S. Frydrych, D. O. Gericke, L. Hallo, J. Helfrich, D. Jahn, E. Kjartansson, A. Knetsch, D. Kraus, G. Malka, N. W. Neumann, K. Pépitone, D. Pepler, S. Sander, G. Schaumann, T. Schlegel, N. Schroeter, D. Schumacher, M. Seibert, An Tauschwitz, J. Vorberger, F. Wagner, S. Weih, Y. Zobus, and M. Roth. Experimental discrimination of ion stopping models near the bragg peak in highly ionized matter. *Nature Communications*, 8:15693 EP-, Jun 2017. Article.

A. Alejo, S. Kar, A. Tebartz, H. Ahmed, S. Astbury, D. C. Carroll, **J. Ding**, D. Doria, A. Higginson, P. McKenna, N. Neumann, G. G. Scott, F. Wagner, M. Roth, and M. Borghesi. High resolution thomson parabola spectrometer for full spectral capture of multi-species ion beams. *Review of Scientific Instruments*, 87(8):083304, 2016.

Non-reviewed first author publications

J. Ding, D. Schumacher, D. Jahn, C. Brabetz, F.E. Brack, F. Kroll, R. Leonhard, I. Semmler, U. Schramm, T.E. Cowan, V. Bagnoud, A. Blazevic, M. Roth. Generation and transport of heavy ion beams at LIGHT. *Report GSI-2018-x*, p. xx, 2018.

J. Ding, D. Schumacher, D. Jahn, C. Brabetz, F.E. Brack, F. Kroll, S. Weih, U. Schramm, T.E. Cowan, V. Bagnoud, A. Blazevic, M. Roth. Further steps towards the generation of intense, subnanosecond heavy ion bunches at LIGHT. *Report GSI-2017-2*, p. 21, 2017.

J. Ding, D. Schumacher, D. Jahn, O. Deppert, C. Brabetz, S. Weih, F. Kroll, U. Schramm, T.E. Cowan, V. Bagnoud, A. Blazevic and M. Roth. First Steps towards the generation of intense, subnanosecond heavy ion bunches at LIGHT. *Report GSI-2016-2*, p. 32, 2016.

Conference contributions

04/18	LIGHT Collaboration Meeting 2018, Darmstadt, Germany **Talk**: Generation, handling and transport of laser-accelerated heavy ion beams within LIGHT
01/18	38th PHEDM international workshop, Hirschegg, Austria **Talk**: Generation, handling and transport of laser-accelerated heavy ion beams within LIGHT
09/17	3rd European Advanced Accelerator Concepts Workshop, La Biodola, Isola d'Elba **Poster**: Generation, handling and transport of laser-accelerated heavy ion beams within LIGHT
01/17	37th PHEDM international workshop, Hirschegg, Austria **Talk**: Generation of intense sub-nanosecond ion beams with the laser-driven LIGHT beamline
09/16	LIGHT Collaboration Meeting 2016, Darmstadt, Germany **Talk**: Heavy ion beams for isochoric heating within the scope of LIGHT
08/15	5th International Conference on High Energy Density Physics, San Diego, USA **Poster**: Generation of intense sub-nanosecond proton and fluorine ion bunches with a novel laser-driven beamline concept

Danksagung

Diese Doktorarbeit wäre ohne die Unterstützung, die ich während meiner Doktorandenzeit sowohl in der Arbeitsgruppe, an der GSI, aber auch außerhalb erhalten habe, nicht möglich gewesen. Im Folgenden möchte ich daher allen Personen danken, die zum Gelingen beigetragen haben.

Zuallererst sei Markus Roth genannt, der mir die Promotion in seiner Arbeitsgruppe angeboten hatte, nachdem er mein Interesse für Laser-Plasma-Physik mit einer sehr umfassenden Führung an der TU Darmstadt und der GSI geweckt hatte. Vielen Dank für das Vertrauen, das du in mich gesetzt hast, indem du mir als externem Absolventen die Promotion innerhalb des LIGHT-Projektes anvertraut hast.

Oliver Boine-Frankenheim möchte ich dafür danken, dass er die Arbeit als Koreferent dieser Dissertation auf sich genommen hat.

Meinem Mentor innerhalb des HGS-Hire Programms, Dennis Schumacher, bin ich sehr dankbar für die Zeit, die er sich für die Diskussion aller physikalischen/technischen Fragen genommen hat, die mir im Laufe der Promotion begegnet sind. Ohne sein immenses Wissen um technische Feinheiten um Z6 und LIGHT wären Strahlzeiten so nicht möglich gewesen.

Auch dem LIGHT-Team bin ich sehr verbunden. Zusammen mit Dennis Schumacher, Christian Brabetz, Diana Jahn, Inken Semmler, Simon Weih, René Leonhardt, Florian Kroll und Florian Brack haben wir während etlicher Strahlzeiten von früh bis spät versucht Probleme, zu lösen und aus Daten schlau zu werden. Hier sei nochmal gesondert auf den Einsatz der beiden Dresdner Flos, Florian Kroll und Florian Brack, hingewiesen, die mit ihren Hardware- und Softwarebeiträgen viel zum Gelingen der Experimentkampagnen beigetragen haben. Simon Busold hat mit seiner Vorarbeit dieses Projekt erst möglich gemacht und hat mir viel über LIGHT beigebracht.

Der gesamten Arbeitsgruppe bin ich für die zwanglose und beizeiten ausgelassene Arbeitsatmosphäre sehr verbunden. Insbesondere seien mein ehemaliger Bürokollege, Florian Wagner, und meine derzeitigen Bürokollegen, Johannes Hornung und Marc Zimmer, hervorgehoben, allzeit bereit den Arbeitsalltag aufzuheitern, die aber auch gute Diskussionspartner für physikalische Problemstellungen abgeben. Mein Masterstudent, Inken Semmler, hat neben unermüdlichem Einsatz in zwei LIGHT Experimentkampagnen auch immer für Abwechslung in der unverzichtbaren Kaffeepause gesorgt und mir nebenbei noch Inkscape näher gebracht.

Abel Blazevic, Jonas Ohland und Nico Neumann möchte ich für ihre konstruktiven Rückmeldungen zur Verbesserung der Doktorarbeit danken.

Special thanks to Ian Tandy for helping me with circumventing the pitfalls of English grammar and wording.

Absolut unverzichtbar für die Dissertation war das Lasersystem PHELIX, das von allzeit motivierten, kompetenten und kundenorientierten Mitarbeitern unter der Leitung von Vincent Bagnoud betrieben wird.

In der Plasmaphysikgruppe an der GSI hatten neben anderen Abel Blazevic, Christian Brabetz, Bernhard Zielbauer, Masoud Afshari und Diana Lang immer ein offenes Ohr für etwaige Probleme und meistens eine schnelle Lösung parat.

In meiner Anfangszeit im Targetlabor am IKP waren mir Gabriel Schaumann, Torsten Abel, Nico Neumann und Alexandra Tebartz immer mit Rat und Tat zur Seite gestanden. Die Bereitstellung der Schwerionenquelltargets durch Gabriel Schaumann und Torsten Abel hat auch erheblich zum LIGHT Projekt beigetragen.

Die Infrastruktur im Allgemeinen und die Werkstätten an der GSI im Besonderen fertigten termingerecht alle Aufträge und das mit hervorragender Präzision. Besonders herausgestellt seien hier die Großmontageabteilung, mit deren Hilfe die Umsetzung der Kavität erfolgreich durchgeführt wurde, und die LINAC RF-Abteilung, die den einmaligen Betrieb der Kavität auch außerhalb einer UNILAC Strahlzeit einrichten konnte. Auch das Targetlabor an der GSI, in erster Linie Bettina Lommel und Jutta Steiner haben mich sehr unterstützt, indem sie Folien für die Schwerionenquelltargets beschichtet haben.

Meinen Freunden und Mitbewohnern danke ich für die Geduld, die sie während meiner Promotion mit mir hatten, speziell in der Schreibphase.

Zuletzt sei auch meine Familie und meine Freundin genannt. Ohne den Ruhepol und die Bestätigung, die Svenja mir während stressiger Abschnitte der Promotion zugesprochen hat, wäre alles viel schwieriger gewesen. Die Förderung meiner Neugier durch meine Eltern ist wahrscheinlich der Grund für meine Begeisterung für Naturwissenschaften. Das Korrekturlesen und die zahlreichen Diskussionen mit meinem Vater über physikalische Phänomene haben mir sehr geholfen. Vielen Dank für alles auch an meine Geschwister!

Curriculum Vitae

Personal

Name	Johannes Ding
Date of birth	13 August 1987
Place of birth	Augsburg, Germany

Education

02/2015-10/2018	PhD at Technical University Darmstadt, Darmstadt Title: Generation, handling and transport of laser-driven heavy ion beams
11/2011-05/2014	M.Sc. in physics at Karlsruhe Institute of Technology, Karlsruhe Master thesis: Electrostatic field simulations and field emission measurements at the KATRIN spectrometers
10/2008-11/2011	B.Sc. in physics at Karlsruhe Institute of Technology, Karlsruhe Bachelor thesis: Messungen von Einzelphotonen am Doppelspalt, Entwurf eines Prototyp-Versuchs im Anfängerpraktikum
09/1998-07/2007	Rudol-Diesel-Gymnasium, Augsburg

Working experience

04/2015-07/2018	Assistant for lectures, tutorials and seminars at TU Darmstadt
03/2012-04/2013	Employment as work student at Polytec GmbH in Waldbronn
07/2002-03/2008	Civil service at "Diakonisches Werk" in Augsburg

Awards

05/2017	Poster Award at Young Scientists Poster Session, GSI-FAIR Colloquium

Experimental Campaigns	
03/2018	Best performance laser-ion acceleration campaign at PHELIX (I015), GSI, Germany
09/2017	LIGHT experimental campaign, transport and temporal compression of protons and carbon ions, GSI, Germany
02/2017	LIGHT experimental campaign, laser-driven carbon ion source, GSI, Germany
06/2016	Stopping power measurements of ions in dense plasmas (U303), GSI, Germany
04/2016	LIGHT experimental campaign, transport and temporal compression of protons and fluorine ions, GSI, Germany
11-12/2015	Laser-ion acceleration with cryogenic targets at VULCAN, RAL, United Kingdom
10/2015	LIGHT experimental campaign, transport and temporal compression of protons and fluorine ions (U287), GSI, Germany
09/2015	Stopping power measurements of ions in dense plasmas (U285), GSI, Germany
07/2015	LIGHT experimental campaign, laser-driven fluorine ion source (U287), GSI, Germany

Erklärung zur Dissertation

Hiermit versichere ich, die vorliegende Dissertation ohne Hilfe Dritter nur mit den angegebenen Quellen und Hilfsmitteln angefertigt zu haben. Alle Stellen, die aus Quellen entnommen wurden, sind als solche kenntlich gemacht. Diese Arbeit hat in gleicher oder ähnlicher Form noch keiner Prüfungsbehörde vorgelegen.

Darmstadt, den November 23, 2018

(J. Ding)